Fast molecular mobility of β_2-adrenergic receptor revealed by time-resolved fluorescence spectroscopy

***

Schnelle molekulare Beweglichkeit des β_2-adrenergen Rezeptors durch zeitaufgelöste Fluoreszenzspektroskopie

Doctoral thesis for a doctoral degree
at the Graduate School of Life Sciences,
Julius-Maximilians-Universität Würzburg,
Section Biomedicine

submitted by

Ashwin Balakrishnan

from Gudiyattam, India

Würzburg 2021

Submitted on:

Members of the *Promotionskomitee*:

Chairperson: Prof. Dr. Thomas Dandekar

Primary Supervisor: Prof. Dr. Katrin G. Heinze

Supervisor (Second):   Prof. Dr. Martin J. Lohse

Supervisor (Third):   Prof. Dr. Antje Gohla

Date of public defence:

Date of Receipt of certificates:

Abstract

G-protein coupled receptors (GPCRs) are the largest family of membrane confined receptors and they transduce ligand binding to downstream effects. Almost 40% of the drugs in the world target GPCRs due to their function, albeit knowing less about their activation. Understanding their dynamic behaviour in basal and activated state could prove key to drug development in the future.

GPCRs are known to exhibit complex molecular mobility patterns. A plethora of studies have been and are being conducted to understand the mobility of GPCRs. Due to limitations of imaging and spectroscopic techniques commonly used, the relevant timescales are hard to access. The most commonly used techniques are electron paramagnetic resonance or double electron-electron resonance, nuclear magnetic resonance, time-resolved fluorescence, single particle tracking and fluorescence recovery after photobleaching. Among these techniques only fluorescence has the potential to probe live cells. In this thesis, I use different time-resolved fluorescence spectroscopic techniques to quantify diffusion dynamics / molecular mobility of β_2-adrenergic receptor (β_2-AR) in live cells.

The thesis shows that β_2-AR exhibits mobility over an exceptionally broad temporal range (nanosecond to second) that can be linked to its respective physiological scenario. I explain how β_2-AR possesses surprisingly fast lateral mobility (~10 µm²/s) associated with vesicular transport in contrast to the prior reports of it originating from fluorophore photophysics and free fluorophores in the cytosol. In addition, β_2-AR has rotational mobility (~100 µs) that makes it conform to the Saffman-Delbrück model of membrane diffusion unlike earlier studies. These contrasts are due to the limitations of the methodologies used. The limitations are overcome in this thesis by using different time-resolved fluorescence techniques of fluorescence correlation spectroscopy (FCS), time-resolved anisotropy (TRA) and polarisation resolved fullFCS (fullFCS). FCS is limited to microsecond to the second range and TRA is limited to the nanosecond range. fullFCS complements the two techniques by covering the blind spot of FCS and TRA in the microsecond range. Finally, I show how ligand stimulation causes a decrease in lateral mobility which could be a hint at cluster formation due to internalisation and how β_2-AR possesses a basal oligomerisation that does not change on activation.

Thus, through this thesis, I show how different complementary fluorescence techniques are necessary to overcome limitations of each technique and to thereby elucidate functional dynamics of GPCR activation and how it orchestrates downstream signalling.

Zusammenfassung

G-Protein-gekoppelte Rezeptoren (GPCRs) sind die größte Familie der Membran-Rezeptoren und durch Bindung von Liganden leiten sie extrazlluläre Signal in das Innere der Zelle weiter. Fast 40% der Medikamente auf der Welt zielen aufgrund ihrer Funktion auf GPCRs ab, obwohl man relative wenig über ihre Aktivierung weiß. Das Verständnis ihres dynamischen Verhaltens im basalen und aktivierten Zustand könnte sich in Zukunft als Schlüssel zur Medikamentenentwicklung erweisen.

GPCRs sind dafür bekannt, dass sie komplexe molekulare Bewegungsmuster aufweisen. Eine Fülle von Studien wurden und werden durchgeführt, um die Beweglichkeit von GPCRs zu verstehen. Aufgrund der Einschränkungen der gängigen bildgebenden und spektroskopischen Techniken sind die relevanten Zeitskalen nur schwer messbar. Die am häufigsten verwendeten Techniken sind die paramagnetische Elektronenresonanz oder die Doppel-Elektron-Elektron-Resonanz, die magnetische Kernresonanz, die zeitaufgelöste Fluoreszenz, die Einzelpartikelverfolgung und die Fluoreszenzwiederherstellung nach Photobleichung. Unter diesen Techniken haben nur die Fluoreszenz-basierten Techniken das Potential, lebende Zellen zu untersuchen. In dieser Arbeit werden verschiedene zeitaufgelöste fluoreszenzspektroskopische Techniken zur Quantifizierung der Diffusionsdynamik oder molekularen Mobilität des β_2-adrenergen Rezeptors (β_2-AR) in lebenden Zellen verwendet.

Diese Arbeit zeigt, dass β_2-AR eine Beweglichkeit über einen außergewöhnlich breiten, zeitlichen Bereich (Nanosekunde bis Sekunde) aufweist, der mit dem jeweiligen physiologischen Szenario verknüpft werden kann. Es wird gezeigt, wie β_2-AR eine überraschend schnelle, laterale Bewegung (~10 µm²/s) besitzt, welche mit vesikulärem Transport in Verbindung gebracht werden kann. Im Gegensatz zu früheren Berichten, wonach die beobachtete Komponente von der Photophysik der Fluorophore und freien Fluorophoren im Zytosol abstammt. Zusätzlich weist β_2-AR eine Rotationsbeweglichkeit (~100 µs) auf, welche es - im Gegensatz zu früheren Studien - dem Saffman-Delbrück-Modell der Membrandiffusion zuordnen lässt. Dieser Unterschied ist auf die Beschränkungen der verwendeten Techniken zurückzuführen. Die Einschränkungen werden in dieser Arbeit durch die Verwendung verschiedener zeitaufgelöster Fluoreszenztechniken überwunden, z. B. der Fluoreszenzkorrelationsspektroskopie (FCS) im Bereich von mehreren hundert Nanosekunden bis Sekunden, der zeitaufgelösten Anisotropie (TRA) im Nanosekundenbereich und der polarisationsaufgelösten FullFCS (FullFCS), die die zeitlich Lücke zwischen FCS und TRA schließt. Zuletzt wird eine Abnahme der lateralen Beweglichkeit durch Ligandenstimulation gezeigt, was ein Hinweis auf Clusterbildung aufgrund von Internalisierung sein könnte, und dass β_2-AR eine basale Oligomerisierung aufweist, die sich bei Aktivierung nicht ändert.

Zusammenfassend kann man sagen, dass verschiedene komplementäre Fluoreszenztechniken notwendig sind, um die Einschränkungen der einzelnen Techniken zu überwinden und dadurch die funktionelle Dynamik der GPCR-Aktivierung und deren Bedeutung für die nachgeschaltete Signalübertragung aufzuklären.

Contents

Abbreviations

ACF	auto correlation function
AF488	Alexa Fluor 488
AR	adrenergic receptor
BE	beam expander
cAMP	cyclic adenosine monophosphate
CAR	carazolol
CHO-K1	Chinese hamster ovary
cpms	counts per molecule per second
CW	continuous wave
D	dichroic filter
DEER	double electron-electron resonance
E	electric field vector
EF	emission filter
emTDM	emission transition dipole moment
EPR	electron paramagnetic resonance
exTDM	excitation transition dipole moment
FCS	fluorescence correlation spectroscopy
FLIM	fluorescence lifetime imaging microscopy
FRAP	fluorescence recovery after photobleaching
FRET	Förster resonance energy transfer
fullFCS	polarisation resolved full Fluorescence Correlation Spectroscopy

FWHM	full width half maximum
GCE	genetic code expansion
GDP	guanosine diphosphate
GPCRs	G-protein-coupled receptors
GRK	G-protein-coupled receptor kinase
GTP	guanosine triphosphate
HEK-293T	human embryonic kidney
hetero-FRET	heterotransfer FRET
homo-FRET	homotransfer FRET
HPMT	hybrid photo multiplier tube
ICS	image correlation spectroscopy
IRF	instrument response function
ISO	isoproterenol
L	lens
NA	numerical aperture
NDF	neutral density filter
NMR	nuclear magnetic resonance
OBJ	objective
PBS	polarising beam splitter
PH	pinhole
RICS	raster image correlation spectroscopy
SAL	salbutamol
SOFI	super-resolution optical fluctuation imaging
SPT	single particle tracking
SRRF	super-resolution radial fluctuations
STED	stimulated emission depletion
TCSPC	time-correlated single photon counting

TIRF   total internal reflection fluorescence

TRA   time-resolved anisotropy

TTTR   Time Tagged Time-Resolved

UT   untransfected cells

VH   vertical excitation horizontal detection

VV   vertical excitation vertical detection

1 Introduction

1.1 Membrane composition and membrane proteins

The boundary between a cell's inner content and its environment is its plasma membrane. Eukaryotic plasma membranes are made of lipid bilayer composed of phospholipids [1]. This composition makes them permeable to nonpolar compounds and impermeable to most polar or charged solutes. Their thickness varies from 5 – 10 nm [2] and are held together using noncovalent interactions [1]. Because of this, plasma membranes are highly dynamic and fluid structures, where most molecules are free to move about in the plane of the membrane and possess diffusion constants in the range of 0.001 - 1 µm²/s [3, 4]. This implies that if a cell is assumed to be spherical with a radius of 15 µm, a cholesterol molecule with a diffusion constant of 1 µm²/s [5, 6] can circumnavigate the cell in 11 s, assuming it undergoes Brownian diffusion in one dimension. The lipid molecules in the plasma membrane make up only a part of its mass, the remainder being proteins and carbohydrates. The exact composition of the plasma membrane varies with organism and cell type. The proteins act as gatekeepers and sensors to communicate with the outer environment. Membrane proteins are classified into three types based on their membrane association: integral membrane proteins or transmembrane proteins that are firmly associated with the bilayer, peripheral membrane proteins that are associated with the membrane through electrostatic interactions and hydrogen bonding and amphitropic proteins that are associated with both membrane and cytosol. This study focusses on a particular family of transmembrane proteins [1].

1.2 G-protein-coupled receptors

G-protein-coupled receptors (GPCRs) are a family of transmembrane proteins ubiquitous in eukaryotes and function as transducers. In fact, they constitute the largest family of transmembrane receptors and over 800 genes in the human body (3% of the human genome) encode for GPCRs. Structurally, they are differentiated by their distinct seven transmembrane helices [7]. As signal transducers, they mediate most actions of neurotransmitters, hormones, immune modulators, pheromones, odorants, light (photons), ions, and other stimulants to allow cells to sense their environment [8]. Therefore, they regulate diverse physiological and biological actions and as a result GPCRs have been studied extensively. This has been reflected with the Nobel prizes associated with GPCR research in 1967 [9], 1971 [10], 1994 [11], 2004 [12, 13] and 2012 [8]. GPCRs are important therapeutic targets and at least 40% of all pharmaceutical drugs currently on the market target one or more of these receptors [14]. Based on their sequence

Table 1.1: Two different GPCR classification systems based on homology and phylogenetic analysis. Adapted from Munk et al. [19].

Class	GRAFS classification
A	Rhodopsin
B	Secretin and Adhesion
C	Glutamate
D	-
E	-
F	Frizzled and Smoothened
T	Taste type-2

homology, functional similarity and phylogenetic analysis, GPCRs are classified into six different classes. Two overlapping classifications exist, one denotes the classes from A-F [15] based on sequence homology and functional similarity, while the other denotes the classes through their prototypical members using phylogenetic studies [16], termed GRAFS. One recent addition to both are the taste type 2 receptors that were previously grouped into a different class, but have been shown recently that they are different [17]. The classification is summarised in table 1.1 and the receptors present in humans are summarised in figure 1.1a. Taking both classifications into account, the different classes are class A (rhodopsin like family), class B (secretin, B1 and adhesion, B2), class C (glutamate family), class D, class E, class F (frizzled and smoothened receptors) and Taste type-2 receptors. Structurally they differ in their ligand binding pocket and their N-terminal domains. Class A or "rhodopsin-like family" are the largest and most diverse class accounting for 80% of GPCRs. They have a relatively simple structure composition with a short N terminus. Class B is regulated mostly by peptide hormones and contains receptors for secretin and glucagon. Secretin receptors or the class B1 in particular have a long N-terminal extracellular domain and a transmembrane domain, both of which are needed to bind peptide hormones. Adhesion receptors or the class B2 have a longer N-terminal domain that undergoes self-cleavage upon maturation. Class C or the glutamate-receptor family includes metabotropic glutamate receptors and type-1 taste receptors. They are structurally distinct from other GPCRs because of their N-terminus, which contains a venus flytrap domain and a cysteine-rich domain. Class D and E contain fungal mating pheromone receptors and cAMP receptors respectively and are not found in humans. Class F contains frizzled and smoothened receptors comprising of a transmembrane domain for ligand binding and a cysteine-rich domain in the N-terminus [18]. All GPCRs regardless of their class possess a common topology: seven transmembrane helices bound together by three intracellular and extracellular loops (figure 1.1b) and they act as transducers converting ligand binding into downstream signalling [7].

1.3   GPCR downstream signalling

Predominantly in class A GPCRs, downstream signalling after ligand activation is mediated either through the heterotrimeric G protein [23–26], hence the name GPCR or through arrestin [25, 27–30] (Figure 1.2). G protein activation leads to dissociation of the G protein into G_α and $G_{\beta\gamma}$ via phosphorylation of guanosine diphosphate (GDP) to guanosine triphosphate (GTP) and both G_α
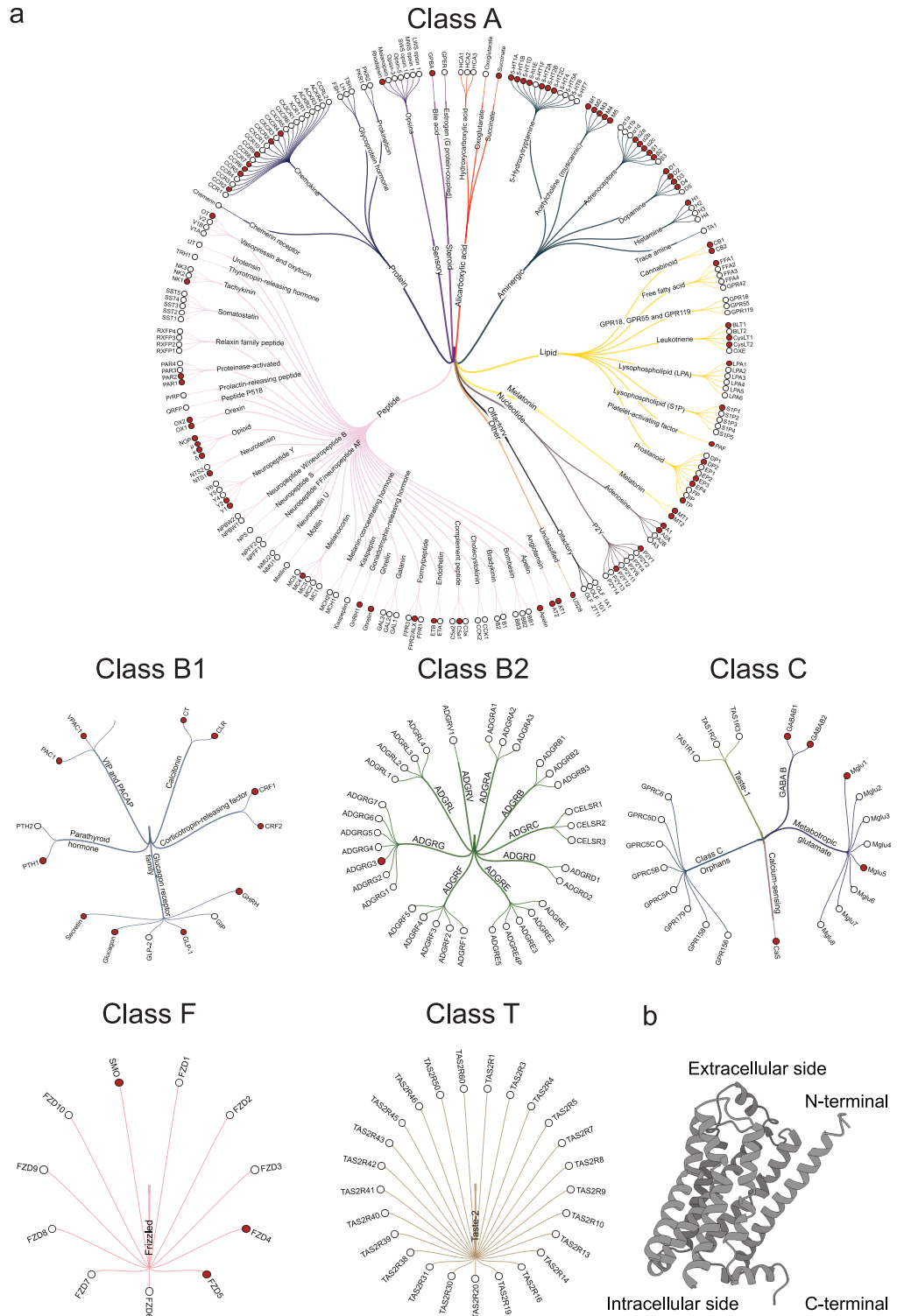
Figure 1.1: Structure and classification of GPCRs present in humans. a. Classes of GPCRs present in humans. Red circles in each class represents GPCRs whose high-resolution structure has been reported and white circles represent GPCRs whose structure is not yet available. Data and representation adapted from GPCRdb [20]. **b**. Crystal structure of a β_2-AR, a class A GPCR, in its basal state. The image was derived from the crystal structure of β_2-AR-T4 lysozyme fusion protein bound to an inverse agonist, carazolol; PDB: 2RH1 [21]. The image was modified using ChimeraX [22].

and $G_{\beta\gamma}$ modulate different effectors (figure 1.2a). Most prominently G_α bound to GTP stimulates the production of cyclic adenosine monophosphate (cAMP) by adenylyl cyclase which activates different downstream effects. Hydrolysis of the G_α bound GTP to GDP terminates GPCR activation, following which the G_α and $G_{\beta\gamma}$ subunits re-associate into the heterotrimeric G-protein [25]. Arrestin mediated signalling involves desensitisation of GPCRs by phosphorylation through G-protein-coupled receptor kinase (GRK) acting in concert with arrestin [27] which functions as a steric hindrance to any further G-protein mediated activation. Arrestin either acts as an adaptor for clathrin-mediated endocytosis or activates a different set of downstream signalling (figure 1.2b). The internalisation keeps the number of receptors traversing the plasma membrane on check. The internalised receptors on the other hand are either degraded in lysosomes or recycled back to the plasma membrane [29].
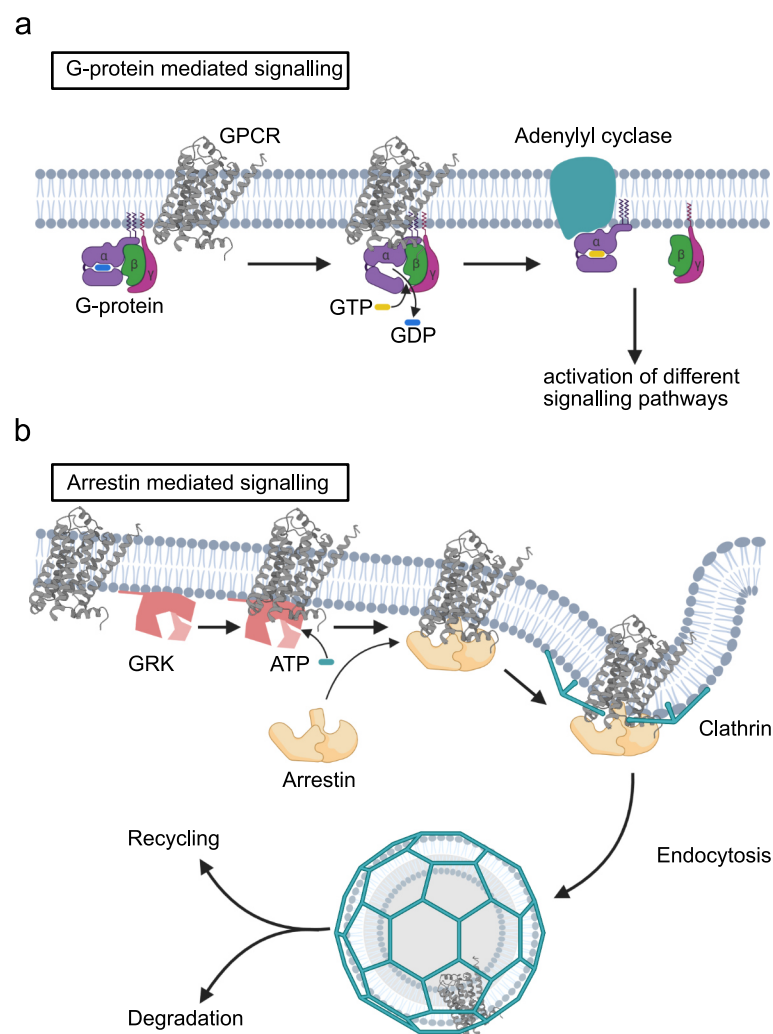
Figure 1.2: Activation of a class A GPCR. The two prominent class A activation pathways. **a**. G-protein mediated signalling involving the heterotrimeric G-protein. **b**. Arrestin mediated signalling involving mainly GRK and arrestin. Drawn using Biorender.com.

The first step of activation, the complete picture of the moments right after the ligand binds to the receptor are not yet fully understood. It has been shown that agonist activation leads to structural rearrangements in GPCRs [31]. This began with the first high-resolution X-ray crystallographic

structure of a GPCR, rhodopsin [32]. Structural studies of activated rhodopsin combined with biochemical and biophysical studies showed that rhodopsin activation acted like an "on-off" switch. Similar structural changes were reported in β_2-AR which especially undergoes a 14 Å outward displacement of its transmembrane helix 6 along with rearrangements in transmembrane helix 5 and 7, which create a binding pocket for G protein [21, 33–37]. Many structural studies have shown a similar change in conformation upon activation [38–43]. Although such conformational changes might also hint at an "on-off" activation switch, the plasma membrane environment in which GPCRs exist is highly fluidic and hence plays an important role in the dynamics and interaction in its basal and activated state. This has been made clear in the case of β_2-AR from nuclear magnetic resonance (NMR) [31, 44] and double electron-electron resonance (DEER) [31] spectroscopic studies, which indicate the presence of intermediate states that are highly dynamic even when bound to agonists. In addition to this, a recent fluorescent biophysical study has shown how different subpopulations of GPCR are present in the plasma membrane at the same time [45]. Hence, to get a complete picture of the activation landscape, studies probing local and global spatial dynamics are needed in addition to structural studies.

This work is performed on β_2-adrenergic receptor (AR), a class A GPCR. ARs are known for their function as the metabotropic gateway for the fight, fright, flight response of the hormones adrenaline and noradrenaline. β_2-AR, due to its physiological significance has been studied as the principal prototypical model for hormone activated GPCRs and has been key in understanding GPCR structure and dynamics [31, 46].

1.4 GPCR mobility and diffusion dynamics

Mobility or diffusion dynamics serves as a lens to focus on spatial dynamics in a system [4, 47]. This is due to the fact that the plasma membrane of mammalian cells are highly fluidic and ordered interfaces which makes their constituents, especially membrane proteins to be highly dynamic and organized in transient phases [3]. Studies have shown this dynamic aspect is an important factor in hypothesising new models for GPCR signalling. Initially studies hypothesised random collision by Brownian motion as the driving force of GPCR signalling [48, 49]. Experimental invalidation led to the formulation of the ternary complex model [50–52] which hypothesises that receptors are in equilibrium between an active conformation and inactive conformation and that receptors in both conformations can access G proteins with different probabilities. Although the model marked a milestone in how GPCR signalling works it did not completely resolve the question about the nature of receptor-G protein interaction. Mainly, all these models did not account for the crowded environment of the plasma membrane, where interactions with various integral membrane proteins, membrane lipids and cytoskeleton is possible [53, 54]. Nevertheless, it can be asserted from the points above that understanding dynamics in both a local and global scale is necessary to completely paint the picture of GPCR signalling.

Molecular mobility or diffusion gives access to the environment of a receptor and how the receptor interacts with this environment. Molecular mobility in cells has been studied in various GPCRs over the years. Rhodopsin was one of the first GPCRs whose mobility was calculated, exhibiting a rotational correlation time of ~20 μs [55] and lateral diffusion constant of ~0.4 μm²/s [56]. This

gave insights and led to the Saffman-Delbrück model [57], which theorised diffusion of a membrane protein in the plasma membrane without any molecular crowding. The advent of fluorescence techniques made molecular mobility more accessible in cells [58, 59]. Lateral and rotational mobility has been used as an indicator for knowing underlying oligomerisation in GPCRs [60–63]. Using the technique of fluorescence recovery after photobleaching (FRAP) Dorsch et al. reported the existence of transient and stable oligomerisation in β_1-AR and β_2-AR respectively [60, 64]. Analysing mobility through single particle tracking (SPT) led to the trapping and compartmentalisation theory of membrane proteins, termed the "fence and picket" model where membrane proteins including GPCRs undergo random diffusion in a finite sized compartment created by the actin cytoskeleton with infrequent transitions to neighbouring compartments termed as "hop diffusion" [65–68]. Later observations showed much slower lateral mobility upon activation among GPCRs which leads to signalling hot spots [45, 69, 70] in addition to the compartmentalisation. Measurement of lipid molecular mobility led to confirmation of the presence of nanodomains [71, 72], which albeit being transient might play a role in GPCR diffusion through lipid-protein interactions. Many studies on mobility have led to better understanding of the factors influencing membrane fluidity and how GPCR interact with each other and its downstream partners, yet more studies over all time scales are needed to get a complete picture. The diffusion constants obtained from these studies are summarised in table 1.2.

Table 1.2: Mean lateral diffusion constants and rotational correlation times of GPCRs in live cells available in literature.

Receptor	Technique	mean diffusion constant ($\mu m^2/s$)	Technique	mean rotational correlation time
Rhodopsin	Micro spectrophotometry	0.4 [56]	Flash photometry	20 μs [55]
A_1 Adenosine	FCS	0.42 [73]		
A_{2A} Adenosine	FCS	0.48 [74]		
A_3 Adenosine	FCS	0.11 [75]		
Histamine H_1	FCS	0.53 [76]		
Neuropeptide Y_1	FCS	0.2 [77]		
Neuropeptide Y_2	FCS	0.2 [77]		
Type-2 Bradykinin	FCS	0.3 [78]		
α_{1B}-Adrenergic	FCS	0.75 [79]		
α_{2A}-Adrenergic	SPT	0.05 - 0.2 [45]	TRA	50 ns [80]
β_1-Adrenergic	SPT	0.001 [81]		
β_2-Adrenergic	FCS, SPT	0.001[81], 0.05-0.2 [45], 0.08 [82], 0.75 [79]		
Muscarinic M_1	FCS	0.75 [79]		
Muscarinic M_3	FCS	0.75 [79]		
Dopamine D_1	FCS	0.75 [79]		
Serotonin$_{1A}$	FRAP	0.18 [83]	TRA	155 ns [61]
Serotonin$_{2A}$	FCS	0.75 [79]		
Serotonin$_{2C}$	FCS	0.8-1.2 [84]		
Metabotropic Glutamate	SPT	0.05 [85]		
μ-Opioid	FRAP	0.08 [86]		

1.5 Techniques for studying molecular mobility

Molecular mobility or diffusion constants on various time scales can be accessed using different spectroscopic and imaging techniques. Prominent spectroscopic techniques include NMR spectroscopy [31, 87], DEER spectroscopy or electron paramagnetic resonance (EPR) spectroscopy [31], fluorescence correlation spectroscopy (FCS) [58] in varied formats [88–91] and time-resolved anisotropy (TRA) [61, 80]. Widely used imaging techniques to access mobility parameter include SPT [92], imaging FCS [93], image correlation spectroscopy (ICS) [94] and raster image correlation spectroscopy (RICS) [95]. Figure 1.3 shows a summary of spatial and temporal resolution of the techniques mentioned here. In the case of *in cyto* experiments, fluorescence spectroscopic techniques overcome the rest in terms of spatial and temporal resolution [96]. Another advantage of using fluorescence spectroscopic techniques is their flexibility to use multiple techniques in complement with each other. This in essence lets one to access more information in addition to molecular mobility. Most studies reported here use one technique or the other and hence are limited in their temporal range. This work was designed to address this by using multiple techniques (FCS, TRA and polarisation resolved full Fluorescence Correlation Spectroscopy (fullFCS)) to overcome the limitations of each technique and understand both local and global diffusion dynamics of β_2-AR in live cells.
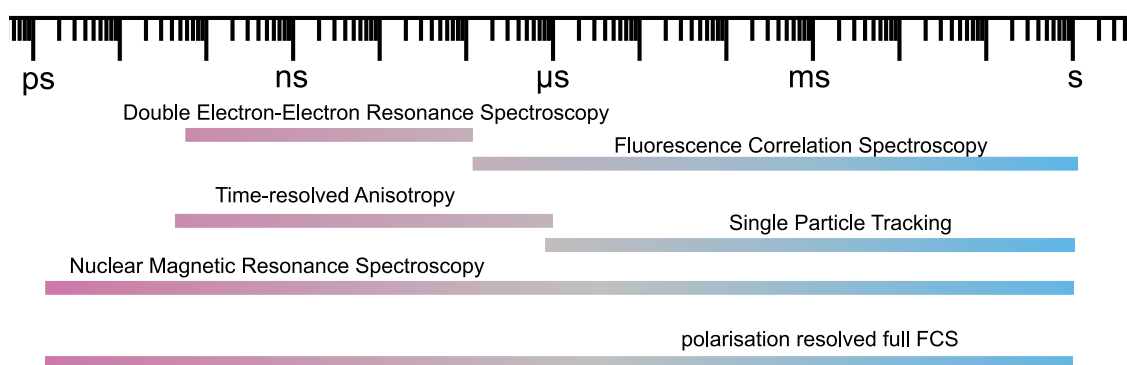

Figure 1.3: Spatial and temporal resolution of spectroscopic and imaging techniques. Spatial and temporal resolution of various spectroscopic and imaging techniques capable of accessing mobility information.

1.6   Aim of the study

Accessing GPCR mobility till now has been limited due to the techniques used to quantify it. This thesis aims to overcome that by combining multiple complementary fluorescence spectroscopic techniques to decipher and quantify fast dynamics of β_2-AR in live cells. This is achieved by performing time-resolved fluorescence spectroscopic measurements on different fluorescently tagged β_2-AR constructs to decipher molecular mobility on a broad temporal range and to link the dynamics to its functional implication in the cell. Finally, the thesis delves into the influence and significance of ligand stimulation on these dynamics. In summary, the main aim of the thesis is to quantify fast dynamics of β_2-AR, its biological significance and variability over activation (figure 1.4).
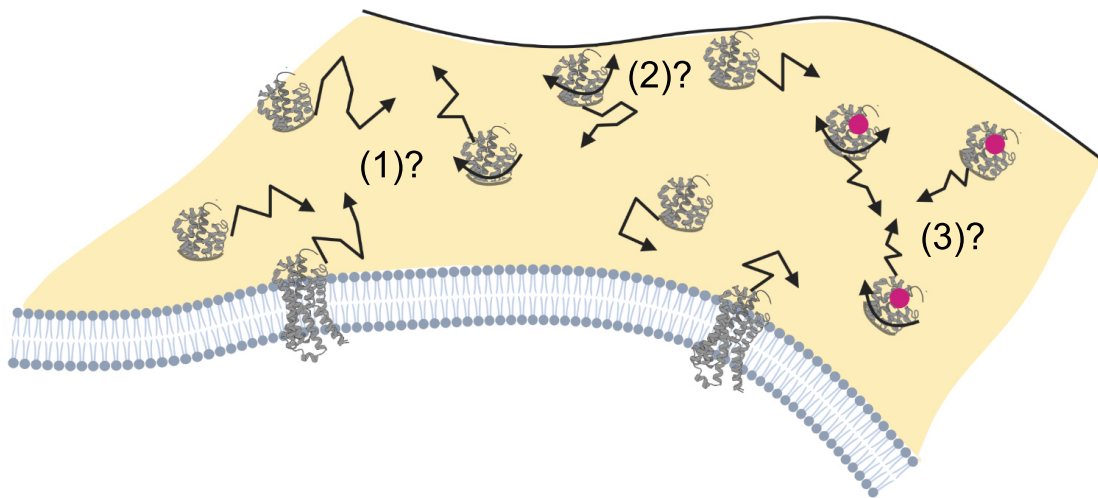
Figure 1.4: Schematic of the aim of the thesis. β_2-AR (grey) embedded and spread in the plasma membrane of a cell possessing different range of lateral and rotational mobility (ragged arrows signify lateral Brownian diffusion and curved arrows signify rotational diffusion). The aim of this thesis is to decipher and quantify all mobility (**(1)** different translational mobility and **(2)** rotational mobility) associated with β_2-AR in the plasma membrane. In addition, measuring the mobility in the basal state, the question of how ligand (circle in magenta) stimulation influences mobility (**(3)**) is also probed. Made with Biorender.com.

2   Theoretical background

In this chapter, the main concepts of time-resolved fluorescence spectroscopic techniques and the Saffman-Delbrück model are introduced, which serve as the basis for understanding data acquisition, analysis and interpretation in this work. The techniques explained here involve TRA, time-correlated single photon counting (TCSPC), Förster resonance energy transfer (FRET), FCS and fullFCS.

2.1   Fluorescence of a dye molecule

Fluorescence is the phenomenon where a molecule absorbs an incident light of a given wavelength and emits light in a different longer wavelength in the time range of ns. When the molecule has light incident on it, an electron in the molecule absorbs energy from the incident photon and gets excited to a higher energy state (excited singlet state) and returns back to its ground state within a span of ns by emitting the gained energy as a photon of lower energy, thereby causing a Stokes shift or red shift. Figure 2.1 explains fluorescence using a Jablonski diagram. The average time that a fluorophore takes to absorb energy, get to an excited state from its ground state and return to its ground state from an excited state is its inherent fluorescence lifetime and is highly dependent on the solvation of the system and temperature. The rate of fluorescence is given by k_f (figure 2.1). There are additional electronic transitions that are possible for the excited state electron, which are given by k_{vr} for the rate of vibrational relaxation, k_{nr} for the rate of non-radiative relaxation, k_{isc} and k'_{isc} for the rate of intersystem crossing. The most common is the metastable triplet state where the electron resides longer before radiating a photon and relaxing to its ground state. Triplet state lifetimes range in the μs. In other terms, a fluorophore is a single molecule emitter and can be described as a quantum two state system. In addition, a fluorophore has a dipole moment and it only absorbs photons when its dipole moment more or less aligns with the electric field vector (E) (plane of polarisation) of the excitation photon [97].

2.2   Time-Resolved Fluorescence Spectroscopy

These electronic transitions could be made use of in controlled ways to understand the kinetics and dynamics underlying in a system over a time domain. This is broadly termed as time-resolved fluorescence spectroscopy. It includes a wide array of techniques such as TRA, FRET, FCS, fluorescence lifetime imaging microscopy (FLIM), etc. This work makes use of FCS, TRA and fullFCS.
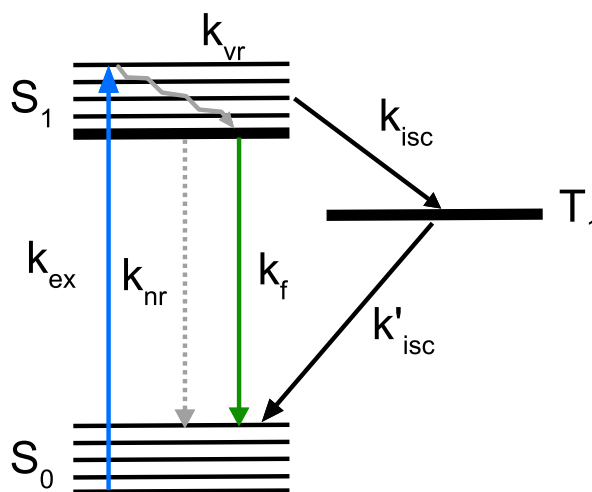
Figure 2.1: Jablonski diagram representing fluorescence. An electron from ground state, S_0 absorbs a photon and gets excited to a higher energy singlet state, S_1. The electron can release its gained energy in different scenarios. One is through vibrational relaxation where the electron drops to a lower vibrational state within S_1 non-radiatively, given by the rate k_{vr}. The electron can return to its ground state non- radiatively, given by the rate k_{nr}. The electron can return to its ground state by emitting a photon of lower energy back, given by the rate k_f. The electron can non-radiatively shift to a lower energy triplet state T_1, termed as an 'intersystem crossing' given by the rate k_{isc}. The electron stays longer in this metastable triplet state before it returns to its ground state by radiating a photon and its rate is given by k'_{isc}. Typical fluorescence lifetimes range in ps-ns and triplet lifetimes range in the µs [97].

2.2.1 Time Correlated Single Photon Counting

TCSPC is based on the principle that for low-level, high-repetition-rate signals, the light intensity is so low that the probability of detecting one photon in one signal period is far less than one [98, 99]. This technique suits live cell measurements as time decay profile of fluorescence signals from multiple single excitation-emission cycles could be recorded without high-excitation power or photo-bleaching [99]. TCSPC involves repetitive and precise time registration of single photons from an emission signal (fluorescence in this case) to build up a histogram of photon times. The TCSPC technique used in this work is Time-Tag recording or Time Tagged Time-Resolved (TTTR) mode, which involves adding a two time stamps on each photon detected, a "micro time", t and "macro time", T. The "micro time" is the time when a photon is detected after a laser pulse and the "macro time" is the time when a photon is detected since the measurement has begun (figure 2.2). As mentioned before, the micro times recorded build up the photon arrival histograms (fluorescence decays). The macro time recorded gives the intensity fluctuations over the entire measurement [98].

2.2.2 Time-resolved fluorescence anisotropy

Fluorescence anisotropy was first described by Perrin [100], which is based on the observation that a small fluorescent molecule excited by a plane polarised light emits depolarised light. This depolarisation is caused due to the molecule tumbling rapidly in solution during its fluorescence lifetime. This in turn, is associated with the fluorophore being a dipole.
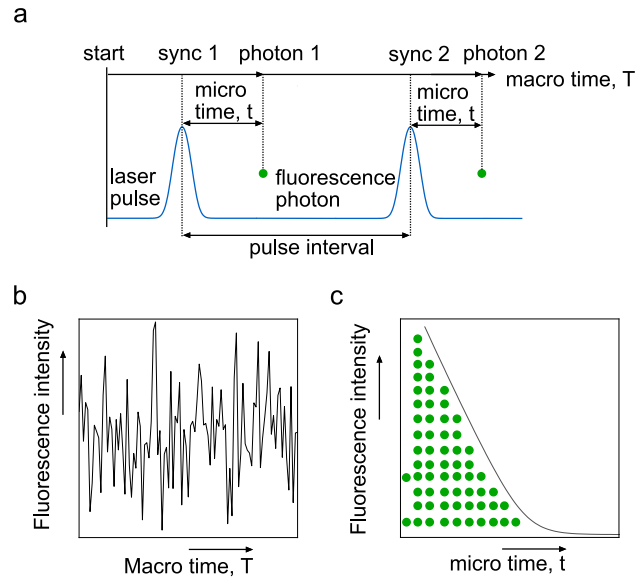
Figure 2.2: Time-Tagged Time-Resolved data collection. A schematic representing how TTTR data is generated. **a**. As soon as a measurement is started, the macro time, T starts recording and as soon a laser pulse sync is recorded, the micro time t starts recording. After a fluorescent photon is detected the micro time stops and starts after the next laser pulse sync but the macro time is recorded till the end of the measurement. Every photon recorded has a micro and a macro time. The macro time constitutes the intensity fluctuations recorded from the measurement (**b**) and the micro times constitutes the photon arrival histogram from the measurement (**c**). Laser pulses are given in blue and fluorescent photons in green. Here, the pulses are separated out from one another by an interval of 50 ns owing to the laser repetition rate of 20 MHz.

In fluorescence anisotropy experiments an ensemble of fluorophores are excited by a polarised laser pulse. The fluorophores, whose excitation transition dipole moment (exTDM) is oriented close to parallel with the polarisation of the excitation light will get excited. This is because the probability of excitation is proportional to cos² of the angle between the transition dipole moment and the polarisation of excitation light (θ) (figure 2.3). This process is termed photoselection. During this excited state the molecules undergo change in orientation and hence a change in the dipole moment and the emitted photon will have a different polarisation. Thus, the emitted light is depolarised with respect to the excitation light. This light is polarisation resolved and focussed on detectors, parallel and perpendicular to the plane of polarisation of the excitation light. The depolarisation caused due to change in orientation or rotational diffusion is described using the collected intensities as fluorescence anisotropy r given in equation (2.1) [101],

$$r = \frac{I_{VV} - I_{VH}}{I_{VV} + 2I_{VH}} \tag{2.1}$$

where I_{VV} (vertical excitation vertical detection (VV)) is the intensity from the detection channel parallel to the field vector of the excitation light and I_{VH} (vertical excitation horizontal detection (VH)) is the intensity perpendicular to it.

The fundamental anisotropy (r_0) of a fluorophore given in equation (2.2) describes the anisotropy if depolarising processes such as rotational diffusion or energy transfer are absent,
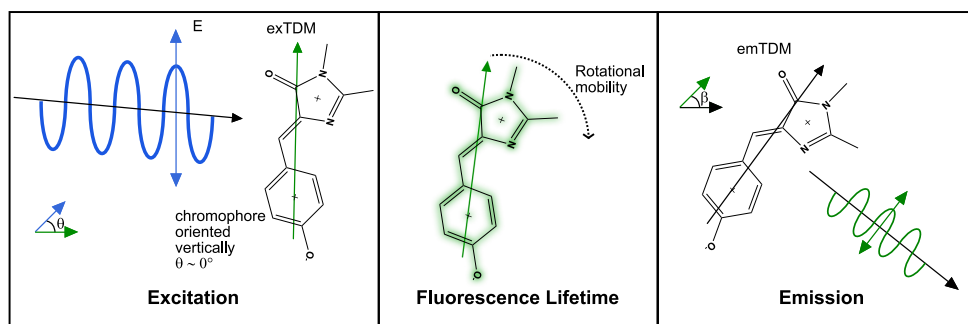
Figure 2.3: Polarisation dependence of excitation and emission. A schematic of the source of fluorescence anisotropy. A fluorophore (EGFP chromophore here, [102]) is excited by a laser pulse with vertical polarisation and the absorption of this light is dependent on θ, the angle between the E of the excitation light and the exTDM. The fluorophore undergoes rotational mobility during its fluorescence lifetime (less in the case of EGFP since the chromophore is bound to the rest of the protein). The fluorophore emits a photon in a changed orientation, parallel to its emission transition dipole moment (emTDM) due to rotational mobility. Anisotropy is dependent on β, the angle between exTDM and emTDM.

$$r_0 = \frac{2}{5}\left(\frac{3cos^2\beta - 1}{2}\right) \tag{2.2}$$

where β is the angle between exTDM and emTDM.

This, in essence gives the maximum and minimum possible fluorescence anisotropy values, 0.4 when β = 0° and -0.2 when β = 90°. Normally small organic fluorophores in a solution that are free to move exhibit fast rotation and hence decreased anisotropy, close to 0 while large molecules, like fluorophores coupled to proteins possess higher fluorescence anisotropy values. Fluorescence anisotropy measured in steady state conditions are termed as steady-state fluorescence anisotropy, r_{ss}.

Time-resolved fluorescence anisotropy, lets us probe into the rotational motions and orientation changes that a molecule possesses and can be described by equation (2.3) [103],

$$r(t) = r_0 exp\left(-\frac{t}{\tau_{rot}}\right) \tag{2.3}$$

where τ_{rot} is the rotational correlation time.

In the case of a fluorophore coupled to a biomolecule, the fluorescence anisotropy would arise from both motion from the biomolecule and the free rotation of the fluorophore attached to the biomolecule and in some cases also the linking groups in between. In such cases, the fluorescence anisotropy would have to be fitted with a bi- or multiexponential decay [104, 105] as shown in equation (2.4).

$$r(t) = b_{protein} exp\left(-\frac{t}{\tau_{rot,protein}}\right) + b_{fluorophore} exp\left(-\frac{t}{\tau_{rot,fluorophore}}\right) \tag{2.4}$$

Usually the measured intensities are directly fitted to calculate the rotational correlation times. The emission intensities are given by equation (2.5) and (2.6).

$$I_{VV} = \frac{1}{3}I(t)\left[1 + 2r(t)\right] \tag{2.5}$$

$$I_{VH} = \frac{1}{3}I(t)\left[1 - r(t)\right] \tag{2.6}$$

2.2.3 Förster Resonance Energy Transfer between identical fluorophores

FRET is a phenomenon of non-radiative energy transfer between a donor molecule in the excited singlet state, S_1 and an acceptor molecule in the ground state, S_0. The phenomenon of FRET, first theorised by Theodor Förster in 1948 [106], relies on long-range dipole-dipole interactions between the donor and acceptor and is highly dependent on the distance and orientation between them (figure 2.4a). It is usually expressed through the FRET efficiency, E which is given as,

$$E = \frac{k_{FRET}}{k_r + k_{nr} + k_{FRET}} = \frac{\tau_D k_{FRET}}{1 + \tau_D k_{FRET}} \tag{2.7}$$

where k_{FRET} is the rate constant of energy transfer, k_r and k_{nr} are the rates of radiative and non-radiative decay respectively and τ_D is the fluorescence lifetime of the donor [107]. k_{FRET} in turn is related to the fluorophore distance as,

$$k_{FRET} = \frac{1}{\tau_D} \cdot \left(\frac{R_0}{R}\right)^6 \tag{2.8}$$

where R is the distance between the donor and acceptor and R_0 is the distance at which FRET efficiency is 50% and is termed as the Förster radius [108]. The Förster radius can be related to the properties of the fluorophore through,

$$R_0 = 0.2108 \cdot \left(\kappa^2 \cdot Q_D \cdot J(\lambda) \cdot n^{-4}\right)^{\frac{1}{6}} \tag{2.9}$$

where κ^2 is the orientation factor, Q_D is the fluorescence quantum yield of the donor in the absence of acceptor and n is the refractive index of the medium [108]. Equation (2.9) is only applicable when the unit of R_0 is in Å.

The resonance between donor and acceptor occurs due to the spectral overlap of the donor emission and the acceptor excitation spectrum (figure 2.4b). The spectral overlap is given by the overlap integral J as,

$$J(\lambda) = \int_0^\infty F_D(\lambda)\epsilon_A(\lambda)\lambda^4 d\lambda \tag{2.10}$$

where $F_D(\lambda)$ is the area-normalised donor emission and $\epsilon_A(\lambda)$ is the wavelength dependent extinction coefficient of the acceptor [108].
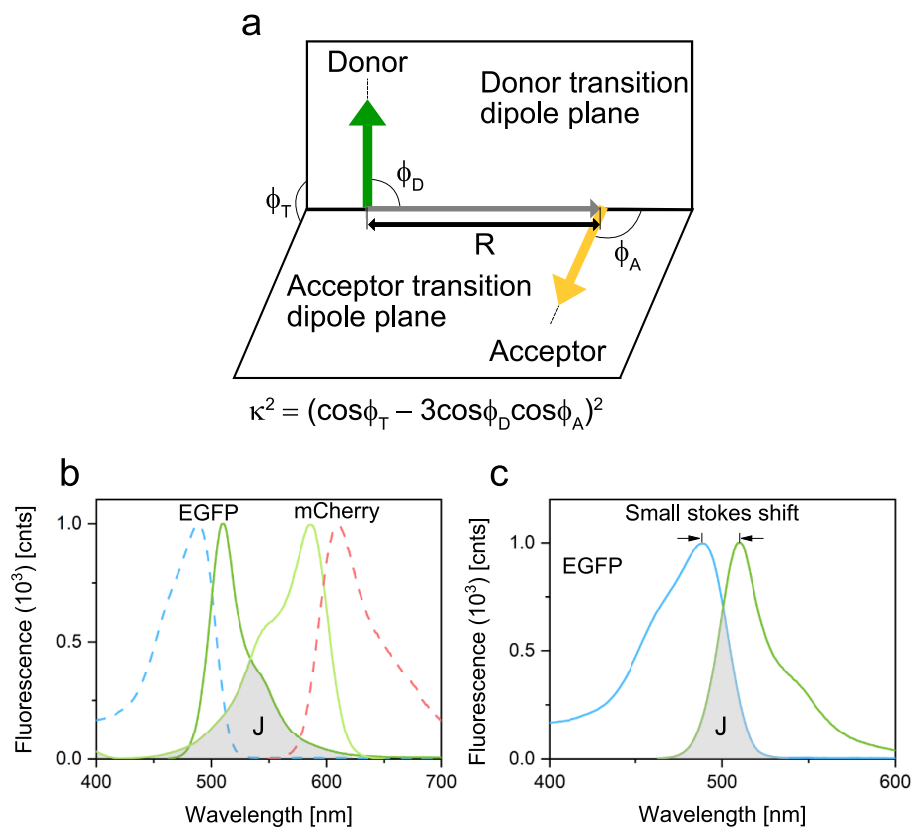

Figure 2.4: Criteria for FRET. a. FRET is dependent on the proximity or distance (R) between the fluorophores and their orientation which is summed up as the orientation factor (κ^2). **b**. Excitation and emission spectra of a FRET pair based on the fluorescent proteins, EGFP (blue: excitation; green: emission) and mCherry (yellowish green: excitation; red: emission). FRET is dependent on the spectral overlap between the emission spectra of the donor and excitation spectra of the acceptor, shaded region in grey. The spectral overlap is numerically expressed through the overlap integral (J, equation (2.10)). **c**. Excitation and emission spectra of EGFP. Fluorescent proteins like EGFP exhibit homo-FRET due to the small Stokes shift between excitation and emission spectra combined with a large overlap between the spectra. Shaded in grey is the spectral overlap for EGFP. Spectral data for **b-c** were taken from the database FPbase.org [109].

In most literature, FRET refers to heterotransfer FRET (hetero-FRET), occurring between two spectrally distinct fluorophores. However, FRET can occur in identical fluorophores, stated as homotransfer FRET (homo-FRET) provided the fluorophores have a high overlap between their excitation and emission spectra or they have a small Stokes shift, e. g. EGFP [108]. Due to spectral independence, hetero-FRET can be observed as a decrease in the donor fluorescence (accessed through lifetime measurement [110, 111], acceptor photobleaching [112, 113] and spectral imaging [114]) whereas homo-FRET detection is indistinguishable in terms of fluorescence due to spectral similarity [108]. The only way to detect homo-FRET is by means of fluorescence anisotropy since FRET efficiency is proportional to the depolarisation of fluorescence emission (equation (2.15)) [115]. This relation can be derived by knowing how the degree of polarisation, steady state anisotropy and quantum yield are related to each other.

Degree of polarisation, p can be related to the quantum yield as

$$\frac{p}{p_{max}} = \frac{6\frac{Q_D}{Q}}{5 + \frac{Q_D}{Q}}$$

(2.11)

where p_{max} is the maximum degree of polarisation in the absence of energy transfer and Q is the total fluorescence quantum yield [115]. p is related to the fluorescence intensity through,

$$p = \frac{I_{VV} - I_{VH}}{I_{VV} + I_{VH}}$$

(2.12)

Since steady state anisotropy r_{ss} is also a similar expression (equation (2.1)) with the only difference being that it is normalised to the total intensity, both p and r_{ss} can be related [101] to each other as,

$$r_{ss} = \frac{2p}{3 - p}$$

(2.13)

At the same time Quantum yield Q is related to the rate of energy transfer given by,

$$Q_D = Q \cdot \frac{1 + \tau k_{FRET}}{1 + 2\tau k_{FRET}}$$

(2.14)

By combining equations (2.7), (2.11), (2.13) and (2.14),

$$E = \frac{6(r_{max} - r_{ss})}{5(r_{ss} + \frac{1}{2})}$$

(2.15)

Equation (2.15) shows that an increase in FRET would consequently lead to a decrease in the steady state anisotropy [115, 116]. Since the efficiency is highly proportional to the distance between the donor and acceptor (here the donor and the acceptor are identical fluorophores), homo-FRET can be used as an indicator to study oligomerisation [117, 118]. Therefore, an increase in oligomerisation would lead to a decrease in steady state anisotropy.

2.2.4 Fluorescence Correlation Spectroscopy

FCS is a statistical technique involving autocorrelation of fluorescence intensity fluctuations to reveal diffusion dynamics and reaction kinetics underlying in a system [119, 120]. FCS gives access to any physical parameter that can give rise to fluctuations in intensity such as diffusion constants, molecular brightness, concentrations, triplet kinetics, etc. FCS was first introduced by Magde, Elson and Webb [58] to measure diffusion and chemical dynamics of DNA-drug intercalation. The technique works best in nanomolar concentrations where each molecule in the system (measurement volume) contributes considerably to the measured signal. Combined with confocal optics, FCS is capable of reaching single molecule sensitivity by limiting the effective detection volume [121]. FCS has been established as a method capable of measuring diffusion dynamics in model membranes [122], native membranes [123] and more importantly, in living cells [124].

FCS is based on the principle of autocorrelation. Autocorrelation involves correlating a signal at a time t with the same signal after a lag time $t + \tau$, and taking its temporal average and the normalised autocorrelation is described by equation (2.16). The resulting auto correlation function (ACF) is the temporal decay function of average fluctuations in the detection volume. Initially the correlations were performed by dedicated correlator hardware, in which case any information about fluorescence lifetime or fluorescence intensity characteristics that were not reflected in the FCS curve are completely lost. With the introduction of TCSPC electronics and TTTR data acquisition, correlation is done on the recorded "Macro Times" by software [125–127]. This adds a layer of flexibility, in removing artefacts by correlating using a time gate [128] or removing fluctuations from aggregates and photobleaching [129]. The ACF is expressed as,

$$G(\tau) = \frac{\langle \delta F(t) \cdot \delta F(t + \tau) \rangle}{\langle F(t) \rangle^2} \tag{2.16}$$

where τ is the lag time, $\delta F(t) = F(t) - \langle F(t) \rangle$ is the fluctuation around average intensity. $\langle \rangle$ denotes temporal averaging. The denominator normalises the equation [119, 120].

A representative ACF is given in figure 2.5 (bottom right). It is calculated by autocorrelating the intensity fluctuations (figure 2.5, top right and left) created when a molecule traverses the detection volume. For lag time zero the ACF converges to,
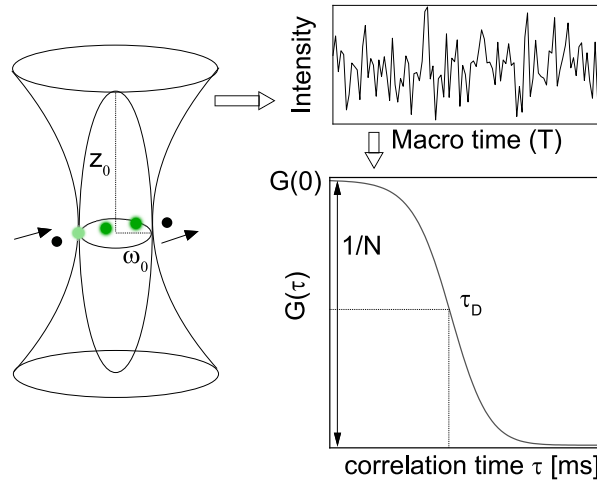
Figure 2.5: Scheme of an FCS measurement. Fluorescence intensity fluctuations arise from fluorescent molecules moving in and out of the confocal detection volume. The intensity fluctuations are autocorrelated to generate the ACF, whose y-intercept, G(0) is the reciprocal of the number of molecules in the detection volume and the inflection point represents the average diffusion time (τ_D). Z_0 represents the half height of the confocal detection volume and ω_0 represents the radius. Determination of the effective detection volume is explained in Methods 3.4.3.

$$G(0) = \frac{\langle (\delta F)^2 \rangle}{\langle F \rangle^2} \tag{2.17}$$

where $G(0)$ is the correlation amplitude at $\tau = 0$. For Poisson statistics governed stochastic processes, variance $Var(N)$ is given by

$$Var(N) = \langle (\delta N)^2 \rangle = N \tag{2.18}$$

where N is the number of molecules in the detection volume. Since N is proportional to fluorescence intensity

$$q\langle N \rangle = \langle F \rangle \tag{2.19}$$

Applying equation (2.19) and (2.18) in equation (2.17) [119],

$$G(0) = \frac{\langle (\delta F)^2 \rangle}{\langle F \rangle^2} = \frac{\langle (\delta N)^2 \rangle}{\langle N \rangle^2} = \frac{\langle N \rangle}{\langle N \rangle^2} = \frac{1}{\langle N \rangle} \tag{2.20}$$

Equation (2.20) shows how the correlation amplitude would increase with a decrease in the number

of molecules. Thus, FCS is sensitive to less molecules in the detection volume. [119]. The inflection point in figure 2.5 corresponds to the diffusion time (time it took a molecule to traverse the detection volume) from which the diffusion constant could be calculated (equation (3.14)). Another parameter that is of importance is the molecular brightness, η. It gives the average number of photons emitted by one fluorophore over unit time. Deviation in η reflects the presence of oligomerised states and aggregates and is given by equation (2.21) [119].

$$\eta = \frac{\langle F(t) \rangle}{N} = \langle F(t) \rangle \cdot G(0) \tag{2.21}$$

In its simplest case, an ACF can be described as dominated by only diffusion as given by equation (2.22). The dynamic parameters that FCS is capable of accessing has been greatly improved through various works [89, 90, 130–133]. In particular by having polarisation resolved detection [90, 131] and continuous wave (CW) laser excitation [130], it is possible to do a full correlation (fullFCS) from s all the way down to ps, limited only by the dead time of the photodetector. Thus rotational correlation times and antibunching effects can be taken into account (figure 2.6). Photon antibunching gives the finite probability for a fluorophore to emit a photon at time t given the last one emitted was at t = 0. Equations (2.25) and (2.27) describe how rotation and antibunching are taken into account respectively.
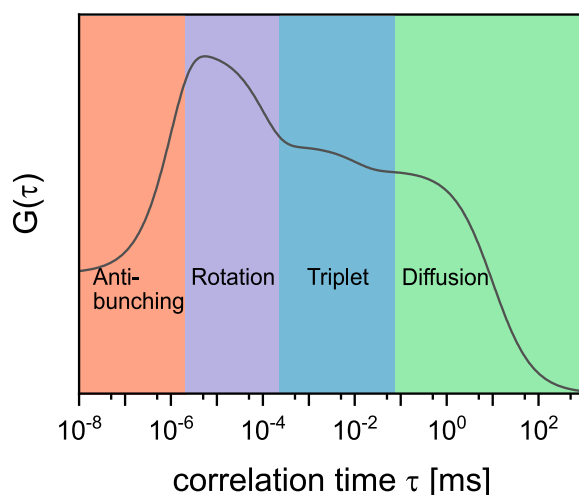
Figure 2.6: Dynamics and timescales covered by fullFCS. A simulation of an ACF exhibiting different dynamics and kinetics based on equation (3.17). The ACF shows molecules inside an effective confocal volume exhibiting free diffusion of 10 ms (green), two relaxation kinetics of 10 µs (triplet, blue) and 0.1 µs (rotation, violet) and one antibunching time of 1 ns (orange). Made with OriginPro.

Taking pure diffusion into account,

$$G(\tau) = G(0) \cdot G_{diff}(\tau) \tag{2.22}$$

where $G_{diff}(\tau)$ is the correlation function for free diffusion [119].

Given polarised excitation and polarisation resolved detection, rotational diffusion (spherical particle) slower than the fluorescence lifetime can be calculated as

$$G(\tau) = G(0) \left[1 + a_1 \cdot exp(-6D_R t) + a_2 \cdot exp(-20D_R t) \right] G_{diff}(\tau) \tag{2.23}$$

$$= G(0) \left[1 + a_1 \cdot exp\left(\frac{\tau}{\tau_{rot}} \right) + a_2 \cdot exp\left(\frac{3\tau}{10\tau_{rot}} \right) \right] G_{diff}(\tau) \tag{2.24}$$

$$= G(0) \cdot G_{rotation}(\tau) \cdot G_{diff}(\tau) \tag{2.25}$$

where D_R is the rotational diffusion constant, $a_{1,2}$ are pre-exponential factors dependent on the particular experimental geometry and τ_{rot} is the rotational correlation time [119, 134].

Given CW excitation and full correlation, antibunching can be calculated as

$$G(\tau) = G(0) \left[1 + \frac{1}{m} \left[-exp\left(-\frac{\tau}{\tau_A} \right) \right] \right] G_{diff}(\tau) \tag{2.26}$$

$$= G(0) \cdot G_{antibunching}(\tau) \cdot G_{diff}(\tau) \tag{2.27}$$

where τ_A is the anitbunching time and m is the number of fluorescent labels per particle [134].

$$\frac{1}{\tau_A} = k_{ex} + k_f \tag{2.28}$$

where k_{ex} is the rate of excitation and k_f is the rate of fluorescence [134].

FCS has also been combined with different imaging methods such as total internal reflection fluorescence microscopy [135], laser scanning confocal microscopy [95], stimulated emission depletion microscopy [71, 136], two photon microscopy [137, 138] and single plane illumination microscopy [93] making it a versatile and feasible technique for cell biological and biophysical studies.

The FCS technique used in this work involves a confocal setup with a single spot without a scanner (Methods 3.4.1) with polarisation resolved detection and both pulsed and CW excitation. Hence normal FCS was performed parallelly with TRA using pulsed excitation and fullFCS with CW excitation.

2.3 Saffman-Delbrück model

The Saffman-Delbrück model theorises the Brownian motion of a cylindrical molecule (membrane proteins) in biological membranes [57]. It assumes the protein molecule to be a cylinder with its axis

perpendicular to the plane of the membrane undergoing Brownian motion. The following derivation was taken from Saffman and Delbrück [57].

The two main parameters that describe diffusion of a molecule on a planar surface is the translational diffusion constant D_T and the rotational diffusion constant D_R. Assuming lateral motion in the plane of the membrane and rotation perpendicular to the axis of the plane, D_T and D_R can be written as

$$x^2 = 4D_T t \tag{2.29}$$

where x^2 is the mean square displacement in time t and

$$\theta^2 = 2D_R t \tag{2.30}$$

where θ^2 is the angular displacement in time t. Both diffusion are in turn related to mobility as

$$D_T = k_B T b_T \tag{2.31}$$

$$D_R = k_B T b_R \tag{2.32}$$

where k_B is Boltzmann's constant, T is the absolute temperature and b_T and b_R are the translational and rotational mobility respectively. Both mobility can be expressed as,

$$b_R = \frac{1}{4\pi\mu a^2 h} \tag{2.33}$$

where μ is the viscosity of the membrane, a is the radius of the cylinder and h is the thickness of the membrane.

$$b_T = \frac{1}{4\pi\mu h} \cdot \left(log \frac{\mu h}{\mu' a} - \gamma \right) \tag{2.34}$$

where μ' is the viscosity of the cytosol and γ is the Euler's constant.

The ratio between these mobility gives,

$$\frac{D_T}{D_R} = \frac{b_T}{b_R} = \left(log \frac{\mu h}{\mu' a} - \gamma \right) \cdot a^2 \tag{2.35}$$

For transmembrane proteins bound to a plasma membrane expected values for the parameters are,

$a \approx h \approx 10^{-7}$ cm, $\mu \approx 1$ poise, $\mu' \approx 10^{-2}$ poise. Applying these values in equation (2.35) gives,

$$\frac{D_T}{D_R} = \frac{b_T}{b_R} = 16 \times 10^{-14} cm^2 \tag{2.36}$$

Thus, the Saffman-Delbrück model gives a good approximation of a membrane protein diffusing in a fluid membrane and how its translational and rotational diffusion could be related to the local membrane viscosity. Although it does not take into account the diverse membrane composition and the crowded environment of a live cell in addition to its varying membrane viscosity [53, 54, 139], it serves as a good approximation for estimating the range of diffusion constants without having dynamics simulations for crowding and cell rheology measurements to calculate the local viscosity.

3 Methods

3.1 Sample preparation

3.1.1 Cell culture

Chinese hamster ovary (CHO-K1) cells were cultured using DMEM/F12 medium and human embryonic kidney (HEK-293T) cells using DMEM medium both supplemented with 10% (vol/vol) featal calf serum, 1% (vol/vol) penicillin (180 mM stock), 1% (vol/vol) streptomycin (15 mM stock) and 1% (vol/vol) L-glutamine (200 mM stock) on 100 mm Petri dishes at 37 °C and 5% (vol/vol) CO_2.

On a regular basis, CHO-K1 and HEK-293T cells were passaged after reaching ~80% confluency. The CHO-K1 cells were first washed with phosphate buffer saline, then treated with trypsin (~2 mL for a 100 mm Petri dish) and incubated for 5 min to dissociate them from the Petri dish. Fresh culture medium (~8 mL for a 100 mm Petri dish) was added to the dissociated cells to stop the proteolytic action of trypsin. These cells were seeded onto a new Petri dish at a higher dilution. The HEK-293T cells in turn were dissociated by pipetting rapidly instead of using trypsin and seeded onto a new Petri dish at a higher dilution.

3.1.2 Coverglass cleaning and preparation

For microspectrometer measurements or imaging the cells were seeded on clean 24 mm circular coverglass or 4-well chambered coverglass. The 24 mm glass coverslips were cleaned to minimize background fluorescence by sonicating the coverslips in an ultrasonic bath at 35 kHz submerged in chloroform and subsequently in 5 M NaOH for 1 hr each followed by washing with double distilled water, then dried and stored in absolute ethanol. The cells were then seeded at a density of 2 x 10^5 per well on the circular coverglass or 2.5 x 10^3 on the chambered coverglass and grown overnight. In the case of HEK-293T cells, the circular coverglass/ chambered coverglass were further treated with poly-D-lysine (100 µM with incubation for 10 min followed by washing once with phosphate buffer saline and air-drying for a couple of hours). For measurements, the coverslips were placed in an attofluor cell chamber with culture media containing 15 mM HEPES without phenol red.

3.1.3 Transfection

Transfection in CHO-K1 was achieved using Lipofectamine 2000 and in HEK-293T cells using Polyplus Jetprime, both in accordance with the manufacturer′s protocol. All transfections except for unnatural amino acid constructs were performed in CHO-K1 cells. In the case of unnatural amino acid constructs, HEK-293T cells were cotransfected with equal amounts of construct DNA and the tRNA plasmid (pCMV tRNA^{Pyl}/NESPylRS^{AF}) [140, 141], where the total amount of DNA was per the transfection protocol from Polyplus Jetprime. When the cells were seeded in 4-chambered coverglass the reagents were scaled down linearly vol/vol to one fourth. After transfection at least 8-12 hr of incubation time was given before measurement.

3.1.4 Fluorescent labelling of β_2-AR^{SNAP} and β_2-AR^{A186TCO}

Cells transfected with SNAP constructs or the genetic code expansion (GCE) constructs were labelled before measurement. The cells expressing SNAP constructs were labelled with 1 µM SNAP surface AF488 for 30 min in the cell culture incubator at 37 °C and 5% (vol/vol) CO_2 followed by washing thrice with phosphate buffer saline. The cells expressing the unnatural amino acid constructs were labelled with ~1.5 µM of Tet-Cy5 or M-Tet-ATTO 488 for initial characterisations and ~400 nM M-Tet-ATTO 488 for spectroscopy measurements. The incubation time for labelling was 10 min at room temperature followed by washing thrice with phosphate buffer saline.

3.1.5 Ligand stimulation

Ligand stimulation was done during measurements, by adding the ligand and incubating for 5 min before starting a measurement. The ligands used and their concentrations are given in table 3.1.

Table 3.1: Ligands used in the study. A list of ligands used in the study along with their final concentration.

Ligand	Concentration, µM
isoproterenol (ISO), agonist	1
salbutamol (SAL), partial agonist	2.4
carazolol (CAR), inverse agonist	1

3.1.6 cAMP test for functional activity

The β_2-AR constructs used in this study were tested for their functionality by detecting their cAMP expression upon activation using a commercial ELISA test kit (cAMP assay kit, ab138880, Abcam). The exception was β_2-AR$^{NT-EGFP}$ as it has been shown elsewhere [142, 143]. The test was performed based on the manufacturer's protocol with a cAMP standard. Figure 3.1 shows how the cAMP expression in the mutated constructs are similar to the wildtype being expressed in

cells. All constructs were expressed in CHO-K1 cells except β_2-AR^{A186TCO} which was expressed in HEK293T cells and were activated with 10 μM of ISO which is known to induce cAMP expression [144]. The cAMP concentration corresponding to figure 3.1b,d is given in table 3.2.
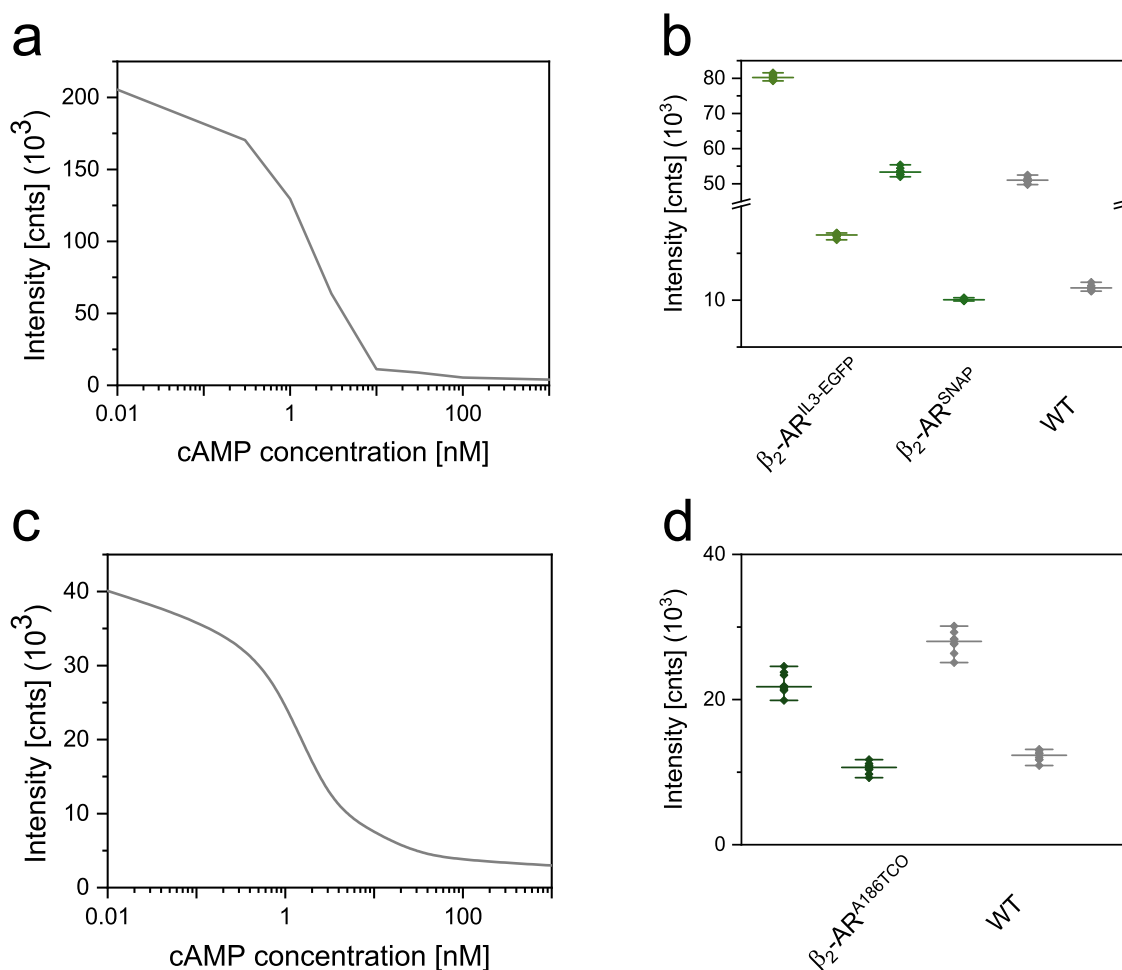

Figure 3.1: Test for functionality of mutated contructs. a. The standard curve corresponding to the data in **b** which gives the cAMP expression levels in β_2-AR$^{IL3-EGFP}$ (green), β_2-AR^{SNAP} (meadow green) and wild type β_2-AR (WT, grey). **c**. Standard curve corresponding to the data in **d** which shows the cAMP expression levels in β_2-AR^{A186TCO} (dark green) and WT.

Table 3.2: cAMP concentration before and after agonist activation measured using cAMP assay.

Construct	Inactive conc. cAMP (nM)	Activated conc. cAMP (nM)
β_2-AR^{SNAP}	4.0 (4.1 WT)	20 (15 WT)
β_2-AR^{A186TCO}	1.26 (0.79 WT)	4.39 (3.47 WT)
β_2-AR$^{IL3-EGFP}$	2.3 (4.1 WT)	11.2 (15 WT)

3.2   Western blot

For Western blots, HEK293T cells seeded in a 15 cm diameter dish were transfected transiently with β_2-AR$^{NT-EGFP}$ with Lipofectamine 2000, according to the manufacturer's instructions. 48 hours after transfection, cells were washed twice with phosphate buffer saline and placed on ice. After addition of 1 mL of lysis buffer (250 µM TRIS, 100 µM EDTA, 100 µM PMSF, 20 µg/mL trypsin, and 60 µg/mL benzamidine), cells were scraped off the plate and the suspension collected. The cells were lysed for 20 s by sonication at 35 kHz and 100 µL were removed (whole lysate sample, W). Separation of soluble, cytosolic cell components from the insoluble membrane debris was done via ultracentrifugation for 20 min at 157,000 g on a Beckmann TLA 120.2 ultracentrifuge at 4 °C. The supernatant (cytosolic fraction, C) was removed carefully and the pellet (membrane fraction, M) was solved in 200 µL of lysis buffer. 10 µL of each sample and the controls were separated on two 12.5% SDS gels (one for the anti-GFP and one for the anti-β_2-AR blot) and transferred onto a nitrocellulose membrane (0.22 µm, Sartorius). The membrane was blocked overnight in 100 mL of TBST buffer (100 mM NaCl, 0.01% Tween20, 30 mM TRIS pH 7.6) supplemented with 5% blocking solution (100 mM NaCl, 50 g/L dry milk powder, 0.01% Tween20, 30 mM TRIS pH 7.6). The buffer was removed and the membrane washed 3x for 10 min with TBST buffer. Next, the primary antibodies were added for 2 hrs: anti-GFP was diluted 1:5000 in TBST supplemented with 5% BSA and anti-β_2-AR was diluted 1:2000. After washing 3x for 10 min with TBST, the secondary antibody HRP Goat Anti-Rabbit was diluted 1:1000 in TBST supplemented with 5% BSA and incubated for 1 hr, followed by 3x washing for 10 min with TBST. 2 mL of ECL Western Blotting Substrate was added and the image captured using the Vilber Fusion FX.

3.3   Confocal imaging

Confocal imaging was used for the fluorescence characterisation of transfected cells using a laser scanning confocal microscope (TCS-SP8, Leica Microsystems) equipped with an HC PL APO CS2 63x/1.40 OIL objective. All samples unless mentioned were excited with a 488 nm Ar$^+$ laser (5 µW at the back aperture). Images were scanned bidirectionally at 100 Hz (pixel size of 43 × 43 nm^2) in accordance with the Nyquist criterion and a pinhole of 1 AU.

3.4   Spectrometer setup, calibration and data acquisition

3.4.1   Time-resolved fluorescence spectrometer setup

All time-resolved fluorescent spectroscopy measurements performed in this study were on a custom time-resolved fluorescence spectrometer setup built by Mike Friedrich (AG Heinze, University of Würzburg) based on an inverted microscope IX-71 stand (Olympus) equipped with a TCSPC module (Hydraharp 400, Picoquant). The materials used in the setup are listed in table 6.9.
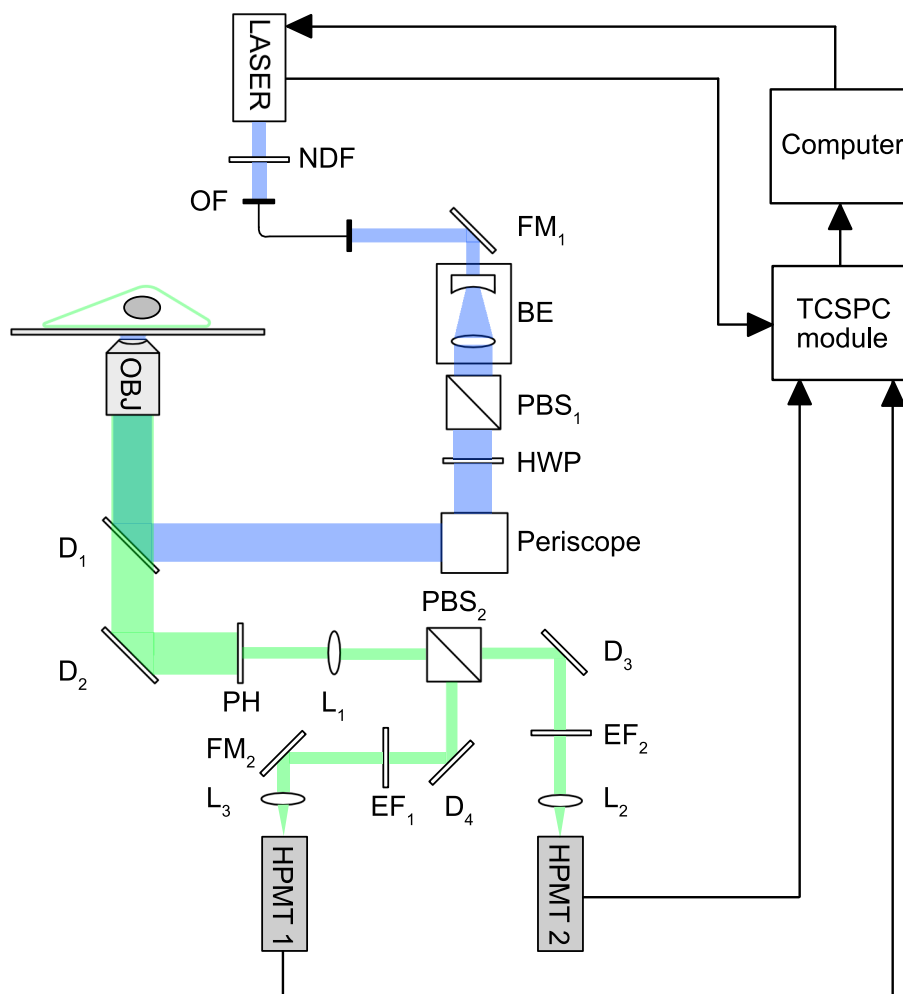
Figure 3.2: Schematic of the time-resolved microspectrometer setup. The beam from the laser passes through a NDF and is then transported through a OF where it passes a FM and is expanded by a BE and controlled for its polarisation using PBS$_1$ followed by an achromatic HWP. The beam is then lifted to the level of the D$_1$ using a periscope and finally focussed onto the sample using an OBJ. The fluorescence is collected using the same OBJ and passes through D$_1$, D$_2$ and PH which controls the amount of fluorescence light that enters the detection arm. The fluorescence beam is then focussed to the right detector using L$_1$, L$_2$ or L$_3$. PBS$_2$ splits the fluorescence based on polarisation, such that the HPMT$_2$ detects parallel and HPMT$_1$ detects perpendicular fluorescence light. D$_3$ and EF$_2$ or D$_4$ and EF$_1$ in tandem allows the right wavelength to reach the detectors HPMT$_2$ and HPMT$_1$ respectively. The laser and the detectors are connected to the TCSPC module (Hydraharp 400) which records the photon arrival times as TTTR data.

Figure 3.2 gives the schematic of the setup. The excitation laser passes through a neutral density filter (NDF) to have a coarse control over the laser power. NDF had four positions 0, 1, 2 and 3 explained in table 6.7. The beam was then fibre coupled through a single mode optical fibre (OF) and later expanded using a galilean beam expander (BE) to a diameter of 7 mm to overfill the back aperture of the objective (OBJ) (100x oil immersion, NA 1.49) and thus create a diffraction limited focal spot. The laser power was measured using a laser diode after BE as a reference, the values of laser power provided in table 6.7 were measured after BE. The size of the effective volume element was calibrated every day before measurement. In the excitation path depolarisation was minimized by a polarising beam splitter (PBS), PBS$_1$ and the laser polarisation was adjusted by an achromatic half-wave plate (HWP). The beam is raised to the height of the back aperture of the OBJ using a

periscope and the dichroic filter (D), D_1 guides the laser through the objective epi-illuminating the sample. A dichroic D_2 guides the fluorescence beam in the detection path where a pinhole (PH) rejects the out of focus light before being projected on hybrid photo multiplier tube (HPMT), $HPMT_1$ and $HPMT_2$ by a telescope in a 4f configuration with lens (L), L_1, L_2 and L_1, L_3 . The beam was split via PBS2 in parallel ($HPMT_2$) and perpendicular emission ($HPMT_1$) after L_1 of the telescope. Dichroic D_3, D_4 and emission filter (EF), EF_1 and EF_2 reject unspecific light in each detection path.

3.4.2 Alignment

The microspectrometer setup had to be aligned and calibrated before measurement every day. All the electronics of the setup was switched on and SymPhoTime 64 was used for the data acquisition. The acquisition parameters were set as in table 6.8 in appendix. The laser power was set to 65% through SymPhoTime and the NDF was set to position 1 and the laser power was measured using a photodiode after the BE. Usually at NDF position 1 was measured to be ~30 µW and if there were fluctuations, the laser box and the output of the single mode fibre were checked to make sure there were no obstacles. The alignment was performed using ~2 nM AF488 solution. The solution was prepared fresh from 1 mM stock by serial dilution and was not used for more than a week. Around 50 µL of this solution was placed on a 24 x 40 mm^2 coverglass and focussed through the OBJ. The focus position was adjusted to the position of the highest online photon counts. The PH xy plane position was then adjusted to get the maximum possible molecular brightness for both channels in the case of oil objective. In the case of the water objective the correction collar was adjusted in addition and with each adjustment of the correction collar the pinhole xy position had to be readjusted to acquire the maximum possible molecular brightness. The intensity fluctuations were then acquired for 3 x 30 s. The corresponding ACF of these measurements were then fitted using equation (3.2) to obtain the shape factor, $\frac{z_0}{\omega_0}$. The PH xy position, focus position and correction collar were adjusted until a shape factor with the range of 3-5 for the oil objective and 4-7 for the water objective.

3.4.3 Calibration

Effective volume

The effective detection volume V_{eff} was determined as described before [119] by diffusion analysis of Alexa Fluor 488 (AF488) (2 nM) in ddH$_2$O by fitting with equation (3.2). The excitation laser power was set based on a power series of AF488 on the setup as shown in figure 3.3 and was well below the saturation point at 25 µW. The power was measured at the back aperture.

V_{eff} of a confocal setup is given by equation (3.1),

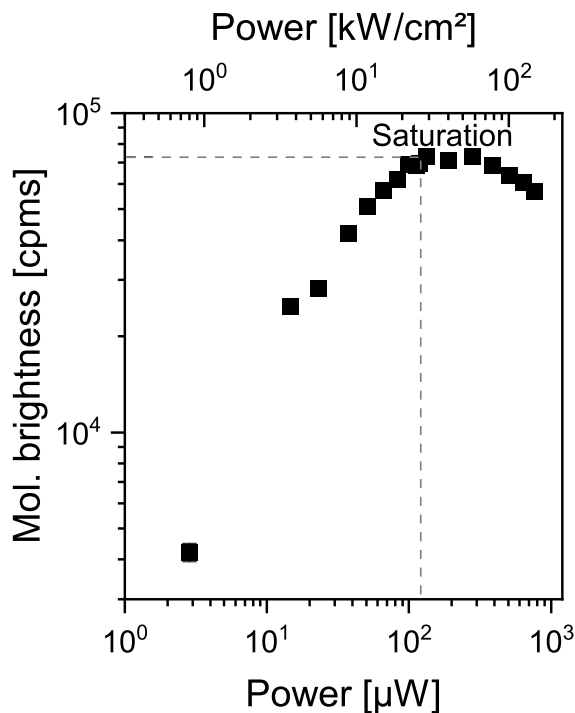$$V_{eff} = \pi^{\frac{3}{2}} z_0 \omega_0^2 \tag{3.1}$$

Figure 3.3: Alexa Fluor 488 power series. Power series of a 2 nM aqueous solution of AF488 to determine the saturation excitation power.

where z_0 is the axial half width of the effective confocal volume, ω_0 the lateral half width of the effective confocal volume [119]. Both width can be extracted by fitting the ACF using,

$$G(\tau) = G_0 \left[1 - T + T \cdot \exp\left(\frac{-\tau}{\tau_T} \right) \right] \cdot \left[\left(\frac{1}{1 + \frac{\tau}{\tau_D}} \right) \left(\frac{1}{\sqrt{1 + \left(\frac{\omega_0}{z_0}\right)^2 \frac{\tau}{\tau_D}}} \right) \right] \qquad (3.2)$$

where G_0 is the correlation amplitude at $\tau = 0$, τ the lag time, T the fractions of molecules in the triplet state (dark state), τ_T the lifetime of the T, and τ_D the diffusion time. The calibration ACF and its corresponding fit and residuals for an AF488 measurement are shown in figure 3.4.

G-factor

G-factor (g) is the ratio of channel sensitivities and is calculated as described [145, 146] by TRA analysis of ~2 nM AF488 in ddH2O using a "tail matching" fit in Origin Pro (Originlab). The microtime data acquired is from the same calibration measurement as mentioned above. The fit is possible as a small dye molecule like AF488, with excited state lifetime of 4.1 ns has a rotational correlation time of ~150 ps. Due to this, all influence of rotation is void after ~1 ns. For an ideal setup, the count rates on both the parallel and perpendicular detection channel should be the same and difference that exist is g. The acquired fluorescence intensity decays from both channels are fitted globally using equations (3.4) (figure 3.5),
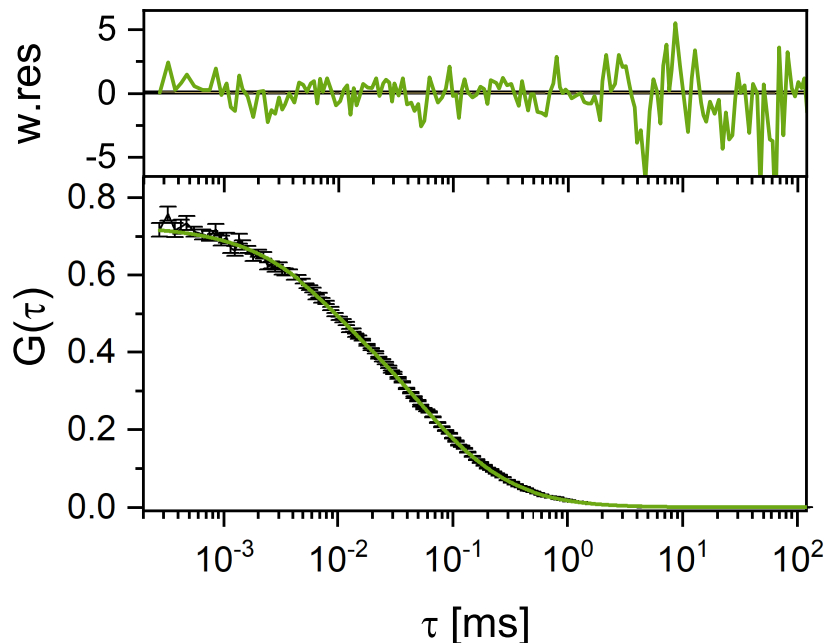
Figure 3.4: FCS calibration. ACF acquired from a 30 s measurement of 2 nM AF488 in ddH2O is given in black and the green overlay corresponds to the fit based on equation (3.2). The top gives the corresponding weighted residuals.

$$I_{VV}(t) = I_0 \left[exp\left(\frac{-t}{\tau_{fl}} \right) \right] + BG_{VV} \tag{3.3}$$

$$g \cdot I_{VH}(t) = I_0 \left[exp\left(\frac{-t}{\tau_{fl}} \right) \right] + BG_{VH} \tag{3.4}$$

where I_0 is the overall emission amplitude, τ_{fl} is the fluorescence lifetime attributed to excited state population. The background BG is the only parameter that was fit independently for both channels, all others were shared between the channels.

3.4.4 Instrument response function acquisition

The instrument response function (IRF) was acquired using 10 mM solution of Erythrosine B in ddH2O. This IRF was then used for reconvolution during the global fit of the fluorescence decay histograms acquired from cells. Figure 3.6 shows an IRF acquired from Erythrosine B solution fitted with gaussian and has a full width half maximum (FWHM) of 255 ps for VV and 276 ps for VH.

Fluorescence anisotropy

The setup was tested with scatter light to understand if excitation was plane polarised and to check the detection path. Diluted milk was used as scatter media and was excited with a 562 nm laser at 1 µW power (power measured at the back aperture). 562 nm excitation was used since the EF
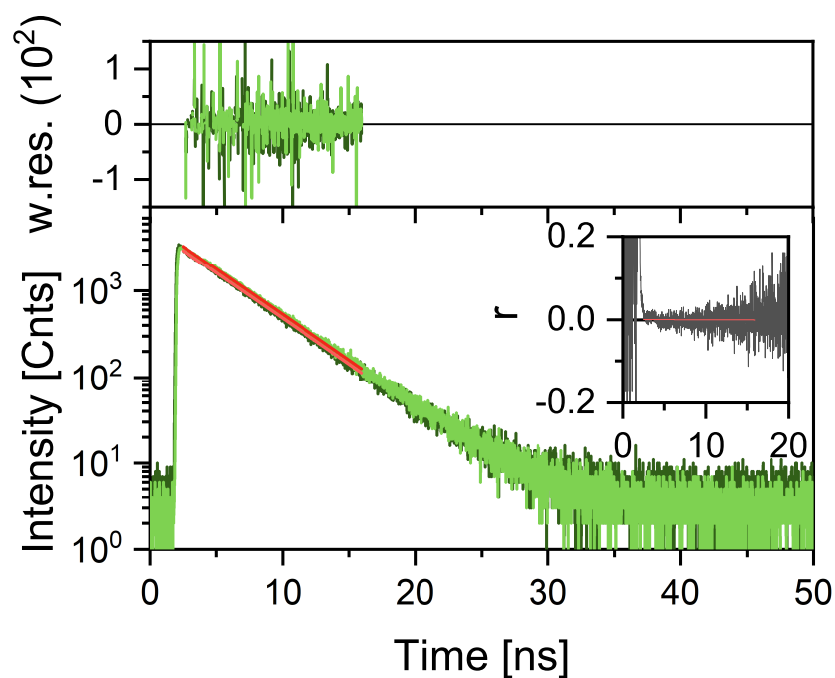
Figure 3.5: G-factor calibration. TCSPC decay of both parallel (dark green) and perpendicular (light green) channels from a 2 nM AF488 solution measurement. Both decays are fitted globally using equations (3.4), shown in dark grey for parallel and grey for perpendicular channel. Top panel shows the corresponding weighted residuals. Inlay on the right shows the corresponding anisotropy decay, to signify that rotational diffusion after 1 ns of the peak is absent.
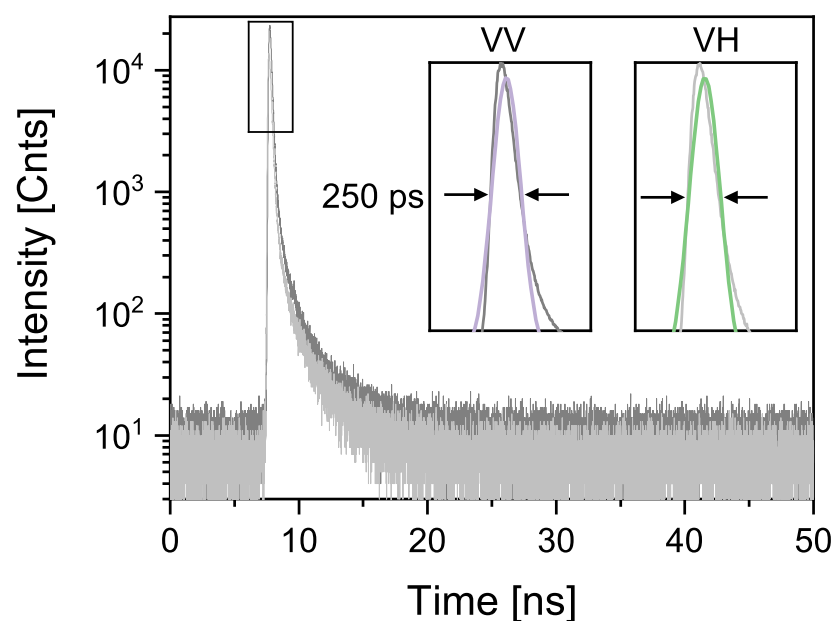
Figure 3.6: Instrument response function of the time-resolved setup. IRF acquired from an aqueous solution of erythrosine B. Grey represents the IRF of the parallel channel and Light grey represents the IRF of the perpendicular channel. The inlay shows the gaussian fit (Violet:VV and light green:VH) performed to determine a FWHM of ~250 ps for both detection channels.

are designed to let light above 525 nm, the detector would sense the scatter light. A λ/2 (HWP in the setup) wave plate was used to change laser polarisation between vertical (V) and horizontal (H)

and a $\lambda/4$ wave plate was used to convert the laser polarisation to circular (C). With V excitation, the detected scatter light should be dominated by light with V polarisation than H, with H excitation the detected scatter light should be dominated likewise by H polarisation. And with C excitation, in the ideal case, detected scatter light should be equally spread with V and H polarisation. Figure 3.7 shows the scatter light decays detected with different excitations. It can be clearly seen that the excitation is indeed plane polarised and the detectors likewise are detecting light with different polarisations.
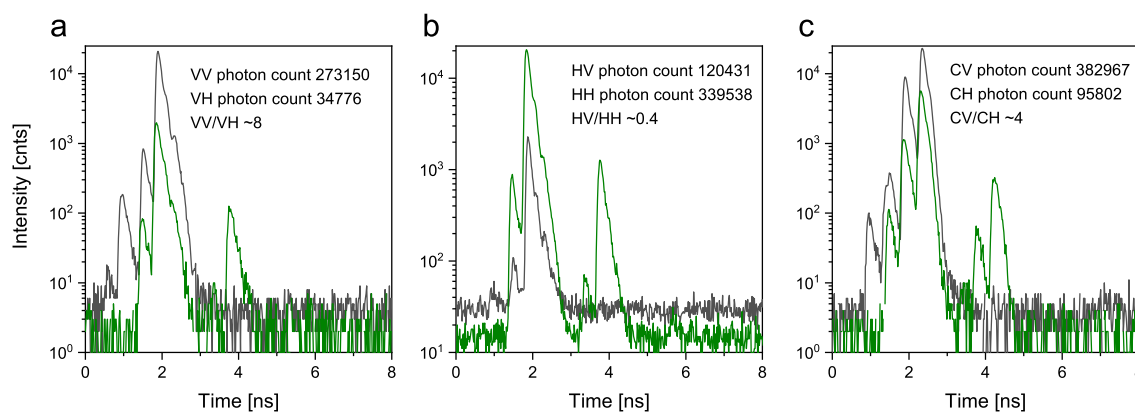

Figure 3.7: Characterising the setup for anisotropy measurements. Scatter light detected by $HPMT_1$ and $HPMT_2$ and the quantification of V and H polarised scatter light when excited with **a**. V polarised light **b**. H polarised light and **c**. C polarised light. Diluted milk was used as the scatter medium and excitation was with 562 nm laser. Excitation polarisation was changed using either a $\lambda/2$ or a $\lambda/4$ wave plate.

Correction factor

Measurement with high-numerical aperture (NA) objectives (NA 1.49 used in this work) lead to depolarisation which can cause artefacts in polarisation resolved measurements. Correction factors, described by Koshioka, Sasaki and Masuhara (k_1 and k_2 in [147], in this work l_1 and l_2) are needed to compensate this effect. A fluorescent molecule that is rotationally symmetric with respect to the emission dipole and randomly oriented in the medium is needed as the reference. In this case, AF488 was used as the reference due to its absorption maxima at 488 nm and it being randomly oriented in a medium. Although it is not rotationally symmetric, its rotational correlation time of 176 ps [148] is hard to fit with less uncertainty as the IRF of the setup is around 250 ps.

AF488 (2 nM) diffusion was measured in aqueous condition and fitted with equations (3.5) and (3.6). The parameters extracted are then fixed and fitted with 3.7 and 3.8 to calculate l_1 and l_2. Equations (3.5) and (3.6) are modifications of equations (3.7) and (3.8) to account for the depolarisation as described in [147]. The latter two were used for further fitting of data from live cell measurements. Figure 3.8 shows the fluorescence decay of AF488 in water and glycerol. In our setup, $l_1 = 0.3329$, $l_2 = 0.1613$ were obtained for 485 nm excitation. The correction factors were checked by fitting AF488 in 70% glycerol with equations (3.7) and (3.8) to observe how its anisotropy changes. It must be noted that this correction factor is highly dependent on the excitation wavelength. Other methods to tackle depolarisation by high-NA have been discussed by Bahlmann and Hell [149, 150] but was not pursued in this work.
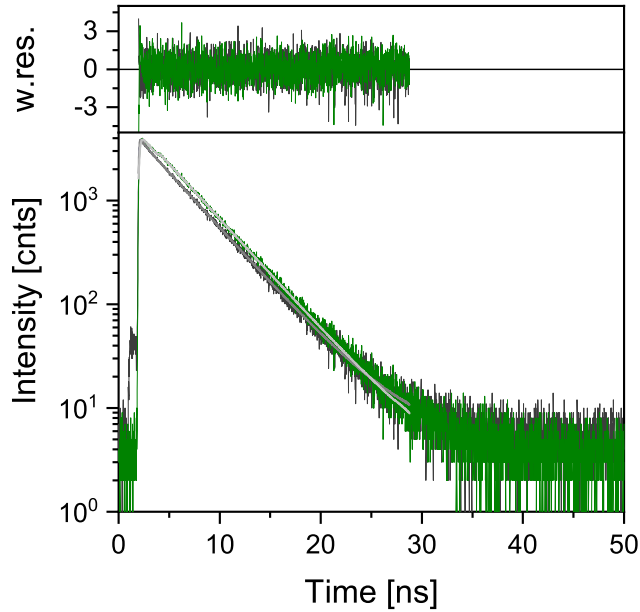
Figure 3.8: Correction factor determination. Fluorescence decay of 2 nM AF488 fitted with equations (3.7) and (3.8) with all parameters except I_1 and I_2 fixed. The fixed parameters were calculated by fitting the same decay with equations (3.5) and (3.6) (not shown). Dark grey represents VV and green represents VH, with fits corresponding to VV and VH are shown in grey and light grey respectively. Weighted residuals corresponding to the fits are given on top, with dark grey corresponding to VV and green corresponding to VH.

$$I_{VV}(t) = \frac{1}{3} I_0 \left[\sum_{i=1}^{n} F_{fl,i} \cdot exp \left(\frac{-t}{\tau_{fl,i}} \right) \right] \left[1 + 2 \cdot \sum_{j=1}^{m} r_{int,j} \cdot exp \left(\frac{-t}{\tau_{rot,j}} \right) \right] + BG_{VV} \qquad (3.5)$$

$$g \cdot I_{VH}(t) = \frac{1}{3} I_0 \left[\sum_{i=1}^{n} F_{fl,i} \cdot exp \left(\frac{-t}{\tau_{fl,i}} \right) \right] \left[1 - \sum_{j=1}^{m} r_{int,j} \cdot exp \left(\frac{-t}{\tau_{rot,j}} \right) \right] + BG_{VH} \qquad (3.6)$$

3.4.5 Data acquisition in live cells

Experimental power for live cell measurements was set to 1 µW (0.8 kW/cm², measured at the back aperture) as this has been well established from studies earlier [151, 152]. During measurement, a dim cell had to be visually picked, then the laser spot was focussed onto the membrane of the cells by displacing the laser focus from bottom to top and simultaneously tracking the online ACF available in SymPhoTime64. Once the focus position hits a positive correlation with at least few hundred counts per molecule per second (cpms) as molecular brightness a measurement is made. Usually, the focus position is cross checked again visually to know if it is in the bottom membrane or top. All measurements, unless stated otherwise were carried out on the basolateral membrane. A typical time-resolved spectroscopy dataset from a cell was acquired for 5-10 min depending on photon count while in the case of fullFCS data was acquired for 20 min to 40 min to gain a high signal

to noise ratio for further analysis. In the case, where only intensity fluctuations were measured, only one detector was used and 5 x 10 s measurements were made per cell, that were then averaged. Note that measurement on cells per coverglass did not exceed two hours since they were at room temperature and not in ideal incubator conditions.

3.5 Data analysis

3.5.1 Time-Resolved Anisotropy

The single photon arrival times acquired were exported to text files using SymPhoTime 64. Decay curve fits were performed using MATLAB using custom scripts and fitted globally using equations (3.7) and (3.8) [153].

$$I_{VV}(t) = \frac{1}{3}I_0 \left[\sum_{i=1}^{n} F_{fl,i} \cdot exp\left(\frac{-t}{\tau_{fl,i}}\right) \right] \left[1 + 2(2 - 3l_1) \cdot \sum_{j=1}^{m} r_{int,j} \cdot exp\left(\frac{-t}{\tau_{rot,j}}\right) \right] + BG_{VV} \quad (3.7)$$

$$g \cdot I_{VH}(t) = \frac{1}{3}I_0 \left[\sum_{i=1}^{n} F_{fl,i} \cdot exp\left(\frac{-t}{\tau_{fl,i}}\right) \right] \left[1 - (1 - 3l_2) \cdot \sum_{j=1}^{m} r_{int,j} \cdot exp\left(\frac{-t}{\tau_{rot,j}}\right) \right] + BG_{VH} \quad (3.8)$$

where I_0 is the overall emission amplitude, $F_{fl,i}$ and $\tau_{fl,i}$ are the fraction and fluorescence lifetime attributed to excited state population decay component i, $r_{int,j}$ is the initial anisotropy (here fixed to the fundamental anisotropy $r_{int,j}$ = 0.38 [154, 155]) and $\tau_{rot,j}$ is the rotational relaxation time of the component j respectively. The background BG is the only parameter that was fit independently for both channels, all other were shared between the channels. g was calculated before every measurement day as described above in section 3.4.3.

3.5.2 Fluorescence Correlation Spectroscopy

The photon traces acquired were autocorrelated and exported to text files using SymPhoTime 64. Correlation curve fits were performed using Origin Pro using different fit models:

1. 2D3DT: one 2D diffusion component, one 3D diffusion component, one Triplet (T, exponential) component
2. 22DT: two 2D diffusion components, one T component
3. 2D2T: one 2D diffusion component, one T and one additional exponential component
4. 2D3D2T: one 2D diffusion component, one 3D diffusion component, one T and one additional exponential component

The general equation has a diffusion part and a relaxation part as given in equation (3.9).

$$G(\tau) = G_{diff}(\tau) \cdot G_{rel}(\tau) \tag{3.9}$$

Model 2D3DT:

$$G(\tau) = \left(\frac{1}{N}\right) \cdot \left(\left(\frac{x_1}{1 + \frac{\tau}{\tau_{d1}}}\right) + \left(\frac{1 - x_1}{1 + \frac{\tau}{\tau_{d2}}}\right) \left(\frac{1}{\sqrt{1 + (\frac{\omega_0}{z_0})^2 \frac{\tau}{\tau_{d2}}}}\right) \right) \cdot$$
$$\left(1 - T_i + T_i \cdot exp\left(\frac{-\tau}{\tau_{Ti}}\right)\right) + G_\infty \tag{3.10}$$

Model 22DT:

$$G(\tau) = \left(\frac{1}{N}\right) \cdot \left(\left(\frac{x_1}{1 + \frac{\tau}{\tau_{d1}}}\right) + \left(\frac{1 - x_1}{1 + \frac{\tau}{\tau_{d2}}}\right) \right) \cdot$$
$$\left(1 - T_i + T_i \cdot exp\left(\frac{-\tau}{\tau_{Ti}}\right)\right) + G_\infty \tag{3.11}$$

Model 2D2T:

$$G(\tau) = \left(\frac{1}{N}\right) \cdot \left(\left(\frac{x_1}{1 + \frac{\tau}{\tau_{d1}}}\right) \right) \cdot \prod_{i=1}^{2} \left(1 - T_i + T_i \cdot exp\left(\frac{-\tau}{\tau_{Ti}}\right)\right) + G_\infty \tag{3.12}$$

Model 2D3D2T:

$$G(\tau) = \left(\frac{1}{N}\right) \cdot \left(\left(\frac{x_1}{1 + \frac{\tau}{\tau_{d1}}}\right) + \left(\frac{1 - x_1}{1 + \frac{\tau}{\tau_{d2}}}\right) \left(\frac{1}{\sqrt{1 + (\frac{\omega_0}{z_0})^2 \frac{\tau}{\tau_{d2}}}}\right) \right) \cdot$$
$$\prod_{i=1}^{2} \left(1 - T_i + T_i \cdot exp\left(\frac{-\tau}{\tau_{Ti}}\right)\right) + G_\infty \tag{3.13}$$

N is the number of molecules in the focus volume, τ is the lag time or delay time, T_i is the dark triplet fractions or protonated fractions of molecules, τ_{Ti} is the lifetime of singlet/triplet or protonated/unprotonated transition dynamics, x_1 is the fraction of the 1st diffusion component, τ_{d1} is the corresponding diffusion time, $1 - x_1$ is the fraction of the 2nd diffusion component, τ_{d2} is its corresponding diffusion time, z_0 is the axial half-width of the effective confocal volume, ω_0 is the lateral half-width of the effective confocal volume and G_∞ is the offset.

With the extracted diffusion times from the fit, and ω_0 from the calibration, the diffusion coefficient D can be calculated using equation (3.14),

$$D = \frac{\omega_0^2}{4 \cdot \tau_d} \tag{3.14}$$

In some cases, D was weighted over the corresponding molecules exhibiting it as a way to normalise using the following equation

$$D_{AVG,i} = D_i \cdot x_i \tag{3.15}$$

where i was the respective component.

3.5.3 Polarisation resolved fullFCS

The fullFCS analysis was performed by Dr. Katherina Hemmen (AG Heinze, University of Würzburg) based on the work by Ries et al. [129] with customisations to take membrane protein dynamics into consideration. The custom scripts can be found in github*. The intensity traces were split into pieces (5-60 s range) and each piece was correlated. Instead of considering all the curves for averaging ($G_{j \neq k}$ in [129]) only the first x curves were taken (depending upon the split size, x = 5-30). This is based on the assumption that membrane proteins, due to their decreased mobility [45], only the first minutes reflect the ground truth before photobleaching, or cell movement, comes into play. The mean square deviation d in this case is given by equation (3.16),

$$d = \frac{(A_n - A_{avg})^2}{n_{points}} \tag{3.16}$$

where d is normalised to the amounts of data points n_{points} used to calculate A_n, A_n is the individual average of each of the n curves and A_{avg} is the average of the first x curves. The value of x was adjusted such that the macro time between comparisons were the same, e.g. for the 10 s slices 30 curves were averaged and for the 60 s slices the first 5 curves were averaged.

$*$ - https://github.com/khemmen/katcorr/

The obtained correlation curves for each measurement were globally fitted using ChiSurf [156] with the same model as for the pulsed FCS experiments (equation (3.10)) except for the crosscorrelation function where we added the additionally required photon antibunching term as described in equation (3.17),

$$G_{CCF}(\tau) = \left(\frac{1}{N}\right) \cdot \left(\left(\frac{x_1}{1+\frac{\tau}{\tau_1}}\right)\left(\frac{1-x_1}{1+\frac{\tau}{\tau_2}}\right)\left(\frac{1}{\sqrt{1+\frac{1}{s^2}\frac{\tau}{\tau_2}}}\right)\right)$$

$$\cdot \left(-a_{ab}exp\left(\frac{-\tau}{\tau_{ab}}\right)\right) \quad (3.17)$$

$$\cdot \left[1 - \sum_{i=1}^{n}\left(a_{Ri} - a_{bi}exp\left(\frac{-\tau}{\tau_{Ri}}\right)\right)\right] + G_{\infty}$$

where a_{ab} denotes the amplitude of the photon bunching (usually ~1) and τ_{ab} is related to the fluorescence lifetime. Note that here usually several relaxation times τ_{Ri} (3 and 4 in our case for EGFP and SNAP constructs respectively) are required as for pulsed FCS due to the extended measurement range.

In the global fit, the relaxation times for all curves corresponding to each measurement were jointly fitted while τ_1, τ_2, N and x_1 were shared among each time slice. Only the amplitudes a_{Ri} of τ_{Ri} were individually optimized. This global, joint fitting approach reduced the number of fitting parameters drastically and stabilized the results. A schematic of the data selection and fitting procedure is shown in figure 4.18.

To compare the absolute, polarisation dependent differences between ACF$_{VV}$ and ACF$_{VH}$, $\Delta ACF(\tau)$ we extracted the kinetics $A_R(\tau)$ for both ACFs:

$$A_R(\tau) = 1 - \sum_{i=1}^{n}\left[a_{Ri} - a_{bi}exp\left(\frac{-\tau}{\tau_{Ri}}\right)\right] \quad (3.18)$$

$$\Delta ACF(\tau) = |A_{R,VV}(\tau) - A_{R,VH}(\tau)| \quad (3.19)$$

3.5.4 Statistical analysis

2t-test

Students 2t-test was performed in Origin Pro using its built-in analysis pipeline for the diffusion constants and rotational diffusion times calculated from FCS and TRA.

F-test

F-test was performed using ChiSurf [156] on the χ^2 ratio (χ^2_{bi}/χ^2_{tri}) for TRA data fitted with bi- and triexponential models. The f-test was performed with the null hypothesis that the biexponential model describes the dataset better than the triexponential model for a 95% confidence interval. The limits of the χ^2 obtained were used as the χ^2 ratio threshold above which the triexponential model was chosen as the better fit.

3.5.5 HYDROPRO calculation

Calculations for hydrodynamic radius and diffusion constants for a given PDB crystal structure was performed using HYDROPRO [157]. The initial parameters for the calculation were the following

Radius of atomic elements: 2.84 Å
Mode: Shell-model from atomic-level
Solute partial specific volume: 0.730 cm^3/g
Solvent density: 1 g/cm^3
Solvent viscosity: 0.01 poise
Temperature: 20 °C

4 Results

This chapter presents the results of the thesis including the receptor construct characterisation and time-resolved fluorescence spectroscopic measurements. The time-resolved fluorescence results presented here are part of the manuscript Balakrishnan et al [158].

4.1 Receptor constructs and experimental design

In order to make use of fluorescence spectroscopic methods, the receptor being studied (β_2-AR) had to be fluorescent. This was achieved by conjugating the receptor to a fluorescent label. Both label position and size were taken into consideration, hence two different labelling strategies were used. One was with fluorescent protein, using EGFP (~27 kDa) conjugated to different positions: N-terminal (β_2-AR$^{NT-EGFP}$) and Intracellular loop-3 (β_2-AR$^{IL3-EGFP}$) (Appendix 6). The other was with organic fluorophores, using SNAP tag (~23 kDa) conjugated to the N-terminal (β_2-AR^{SNAP}, Appendix 6) and using GCE where β_2-AR$^{IL3-EGFP}$ and β_2-AR had a point mutation, A186TCO (β_2-AR$^{A186TCO-IL3-EGFP}$ and β_2-AR^{A186TCO}) to encode for an unnatural amino acid trans-cyclooctene (TCO*lysine) via amber suppression technology [141, 159] (Appendix 6). Both SNAPtag and GCE based constructs were capable of covalently binding to an organic fluorophore of interest. The reason for utilising an organic labelling strategy was to understand the influence of fluorophore size on mobility since they are considerably smaller. β_2-AR$^{NT-EGFP}$, has been established and used in other studies [142, 143]. β_2-AR$^{IL3-EGFP}$, β_2-AR$^{A186TCO-IL3-EGFP}$ and β_2-AR^{A186TCO} are characterised in this work. The α_{2A}-AR constructs mentioned in Appendix materials 6 have also been established elsewhere [45] and were used as controls for the time-resolved fluorescence spectroscopy measurements.

4.2 Characterisation of new constructs

The constructs were first checked for their functional efficacy. This was done by checking their cAMP levels when activated by an agonist [160], using a commercial cAMP detection kit as described in methods 3.1.6. In the case of β_2-AR$^{IL3-EGFP}$, transfection was optimised to get minimal expression of receptors. In the case of GCE constructs, β_2-AR$^{A186TCO-IL3-EGFP}$ acted as the control for β_2-AR^{A186TCO} to know if it is the receptor that fluoresces. For β_2-AR^{SNAP} and β_2-AR^{A186TCO} labelling was optimised to reduce free dye in the solution.

4.2.1 Optimising transfection for β_2-AR$^{IL3-EGFP}$

CHO-K1 cells were transfected with different amounts of the vector DNA (2 µg, 4 µg and 6 µg DNA / 2 x 10^5 cells) to find the right degree of transfection for spectroscopic measurements (figure 4.1). The starting amount (2 µg) was based on the protocol of the reagent manufacturer (Lipofectamine 2000) and has been reported earlier [143] for β_2-AR$^{NT-EGFP}$ and α_{2A}-AR$^{NT-EGFP}$ for FCS measurements. It can be seen that transfection with 2 µg DNA provided minimal expression that was good for a time-resolved fluorescence spectroscopic measurement while 4 µg DNA gave a higher expression and 6 µg DNA resulted in cell death post transfection. Hence for further experiments 2 µg DNA was used for transfection.
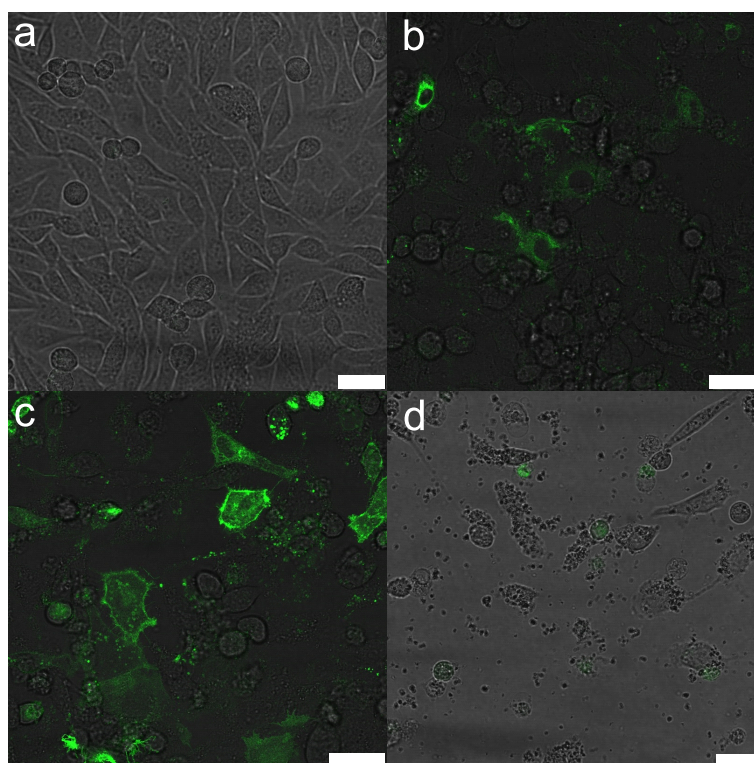

Figure 4.1: Characterisation of β_2-AR$^{IL3-EGFP}$ concentration for optimal expression. a. Untransfected CHO-K1 cells. **b**. β_2-AR$^{IL3-EGFP}$ transfected CHO-K1 cells with 2 µg of DNA/ 2 x 10^5 cells. **c**. β_2-AR$^{IL3-EGFP}$ transfected CHO-K1 cells with 4 µg of DNA/ 2 x 10^5 cells. **d**. β_2-AR$^{IL3-EGFP}$ transfected CHO-K1 cells with 6 µg of DNA/ 2 x 10^5 cells. Scale is 25 µm.

4.2.2 Expression of β_2-AR$^{A186TCO-IL3-EGFP}$ and β_2-AR^{A186TCO}

HEK-293T cells were transfected with β_2-AR$^{A186TCO-IL3-EGFP}$ to check whether the mutation at A186TCO worked and can incorporate an unnatural amino acid capable of binding to an organic dye. EGFP served as the reference for expression of the receptor. Figure 4.2a-c shows expression of EGFP and the unnatural amino acid labelled with Cy5. Colocalisation analysis (performed on Fiji [161]) of selected cells (figure 4.2d) gives a mean Mander's coefficient [162, 163] M_1 of 0.61 ± 0.08 and M_2 of 0.66 ± 0.10 and a mean Pearson's correlation coefficient [162, 163] of 0.4 ± 0.2 (figure 4.2e). M_1 gives the amount of Cy5 pixels that overlap with EGFP pixels

and M_2 gives the amount of EGFP pixels that overlap with Cy5 pixels. The Pearson's coefficient here gives the average correlation between the Cy5 intensity and EGFP intensity. Both coefficients showed Cy5 colocalises with EGFP and since it was clear that the mutation does not affect the expression of the protein, β_2-AR^{A186TCO} was designed by Dr. Gerti Beliu (AG Sauer, University of Würzburg) which does not possess an EGFP and this construct was used for further experiments.
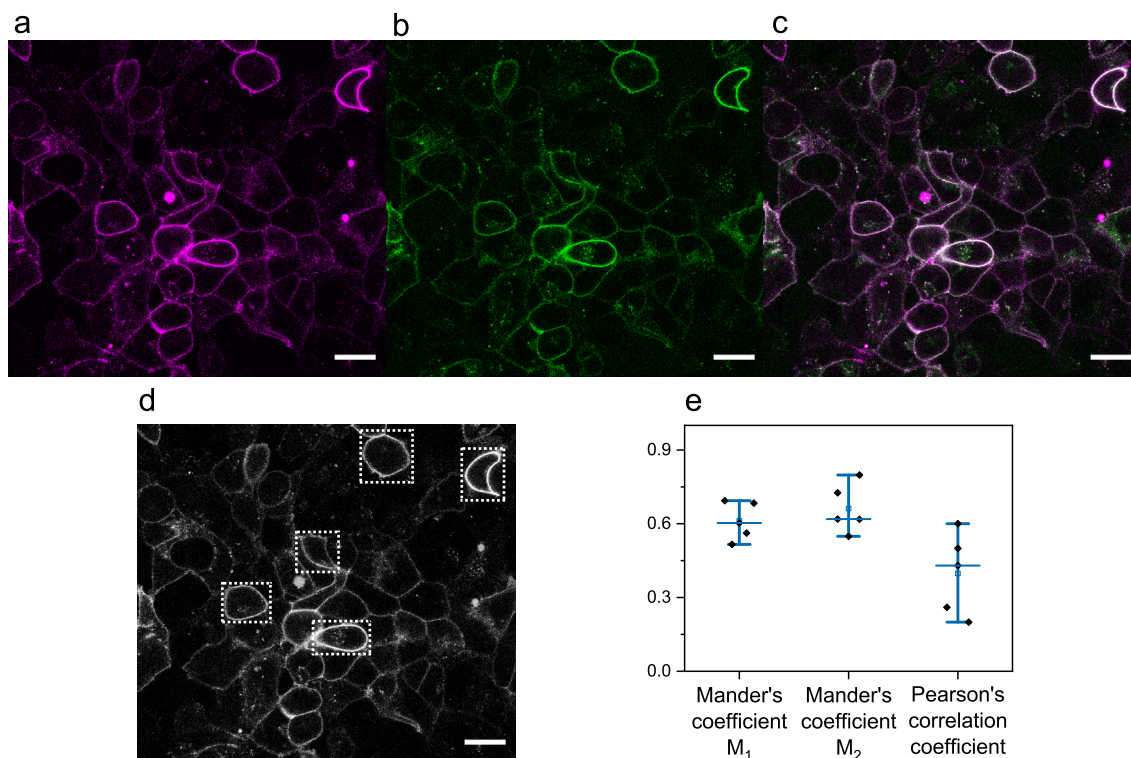

Figure 4.2: Expression and colocalisation of β_2-AR$^{A186TCO-IL3-EGFP}$. **a**. Cy5 bound to unnatural amino acid TCO*Lysine. **b**.β_2-AR$^{A186TCO-IL3-EGFP}$ being expressed in HEK 293T cells. **c**. Composite image of a and b showing the majority of Cy5 seen in a are receptor bound. **d**. Composite image with cells randomly selected for quantifying colocalisation highlighted with dashed-white boxes. The cells were selected by drawing an outline on their periphery and colocalisation parameters of Mander's overlap coefficients, M_1, M_2 and Pearson's correlation coefficient were calculated using Fiji [161]. M_1 here stands for the correlation between Cy5 and EGFP intensity and M_2 for the correlation between EGFP and Cy5 intensity. Scale is 20 µm.

4.2.3 Labelling characterisation of β_2-AR^{SNAP} and β_2-AR^{A186TCO}

Different concentrations of dyes were tested to find which suited best for a spectroscopy measurement. First, confocal imaging was used to discern between different concentrations and then the chosen concentration was used for a spectroscopy measurement to test whether there is any influence of free dye.

β_2-AR^{SNAP}

In the case of β_2-AR^{SNAP} the suggested concentration of SNAP Surface Alexa Fluor 488 labelling was 5 µM with 30 min incubation followed by washing thrice with phosphate buffered saline. I tested different concentrations ranging from 1 - 5 µM keeping the time of incubation and washes the same. Figure 4.3 shows confocal images of different concentrations. At first glance, all images look dim and more or less the same, meaning 1 µM already saturates the receptors that are bound to the plasma membrane.
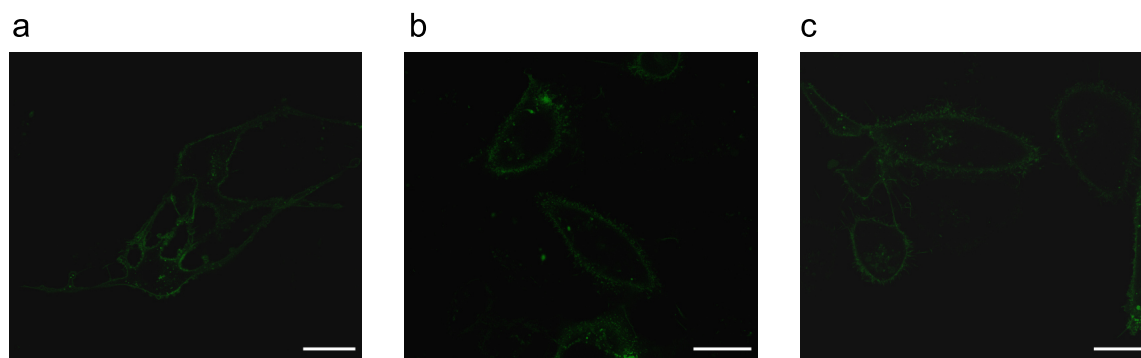

Figure 4.3: Labelling optimisation of β_2-AR^{SNAP}. CHO-K1 cells expressing β_2-AR^{SNAP} labelled with SNAP Surface Alexa Fluor 488 at **a**. 1 µM **b**. 3 µM and **c**. 5 µM. 1 µM AF488 saturates plasma membrane bound β_2-AR^{SNAP} receptors as seen from **a**. Scale is 20 µm.

β_2-AR^{A186TCO}

For labelling β_2-AR^{A186TCO}, ATTO 488 was chosen as the label, since it had a similar excitation and emission spectra as EGFP and AF488 used for SNAP labelling. In addition, M-Tet-ATTO 488 which is the conjugate that reacts with the TCO of the unnatural amino acid, has different photophysical properties when unbound and bound and has 20x less fluorescence when unbound, as shown in Beliu et al. [141]. This means the influence of free unbound dye on the autocorrelation amplitude is minimal. Figure 4.4 also shows how the intensity and short rotation changes from M-Tet-ATTO 488 to TCO*Lysine bound ATTO 488.

The suggested concentration of M-Tet-ATTO488 is between 1-3.5 µM [141]. A range of 1-4 µM was tested with confocal imaging and figure 4.5 shows that at 1 µM very few cells were saturated with fluorescent plasma membrane bound receptors. Spectroscopy measurements showed presence of free dye as a shorter rotational component even with the 1 µM labelling although the brightness of the free dye was 20x lesser than bound dye. Even though fluorescence inside the cell was less in confocal imaging, ATTO 488 unlike in the case of AF488 is not certified as membrane impermeable. Sungkaworn et al., describes a labelling protocol for SNAP labelling to decrease the density of fluorescent receptors available for SPT [45]. They explain labelling for 30 min at room temperature with three washes with PBS with 5 min incubation between each wash. I used a similar approach with 500-100 nM ATTO 488. The lowest possible labelling concentrations in which selecting cells using the ocular were still possible was 400 nM. Yet, the short rotation was still present in fluorescence decay histograms. Hence, during analysis, the
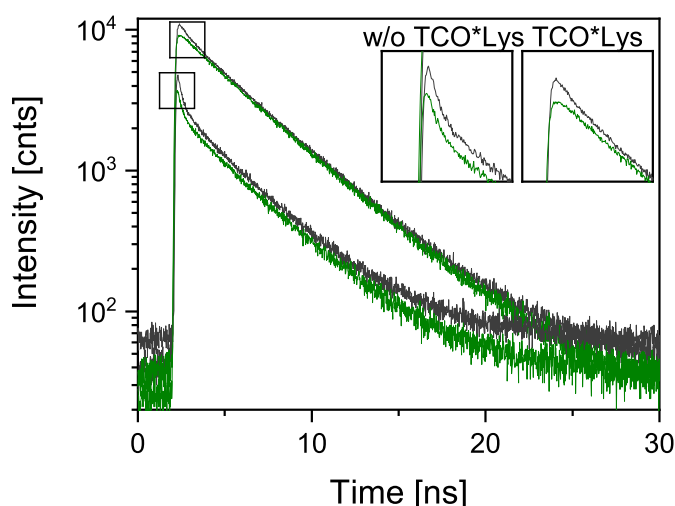
Figure 4.4: M-Tet-ATTO488 fluorescence decay in presence and absence of TCO*Lysine. Fluorescence decay of M-Tet-ATTO 488 (2 nM) in ddH$_2$O, dark grey represents parallel detection channel and green represents perpendicular detection channel. After adding 1 nM TCO*Lysine the shorter decay component decreases with a visible increase in photon count rate, hence the shift in peaks although measurement time was 300 s for the sample with TCO against 450 s for the sample without.

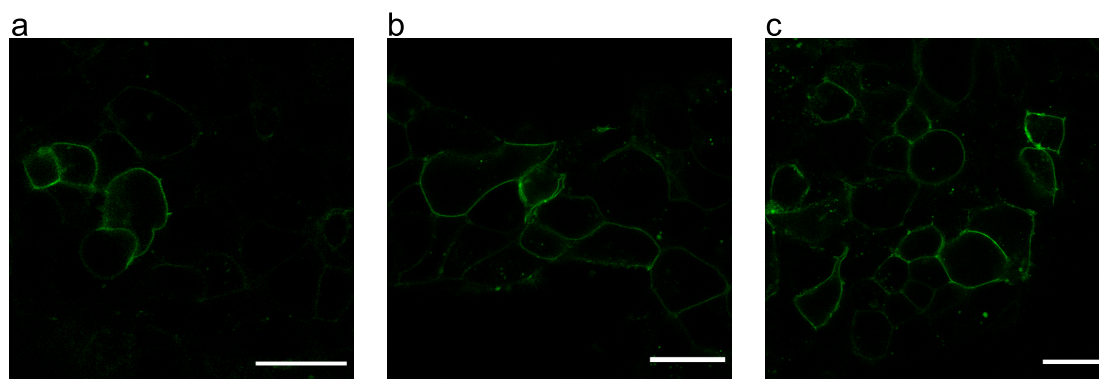fluorescence decay histograms were fitted with an additional rotation component to compensate for this.

Figure 4.5: Labelling optimisation of β$_2$-AR^{A186TCO}. **a**. HEK 293T cells expressing β$_2$-AR^{A186TCO} labelled with M-Tet-ATTO 488 at **a**. 1 µM **b**. 2.5 µM and **c**. 4 µM. Scale is 20 µm.

4.2.4 Optimal concentration of receptors for a measurement

For spectrometric measurements cells with minimal expression were chosen. First, the cells were visually selected based on their brightness (dimmest). Then during the measurement, the online apparent particle number from SymPhoTime64 was used as the indicator and a cell was rejected if the apparent particle number was more than 250. Figure 4.6 gives a CHO-K1 cell with minimal

expression and receptor density (570 receptors/µm², calculated using the particle number from fit shown in Figure 4.6) good for a spectrometric measurement. The ACF calculated from the intensity fluctuation from the cell was fitted with equation (3.10). The parameters derived were τ_{dfast} 0.63 ms, τ_{dslow} 34.7 ms, x_{fast} 0.42, x_{slow} 0.58, τ_{T1} 35.4 µs and τ_{T2} of 1.8 µs.

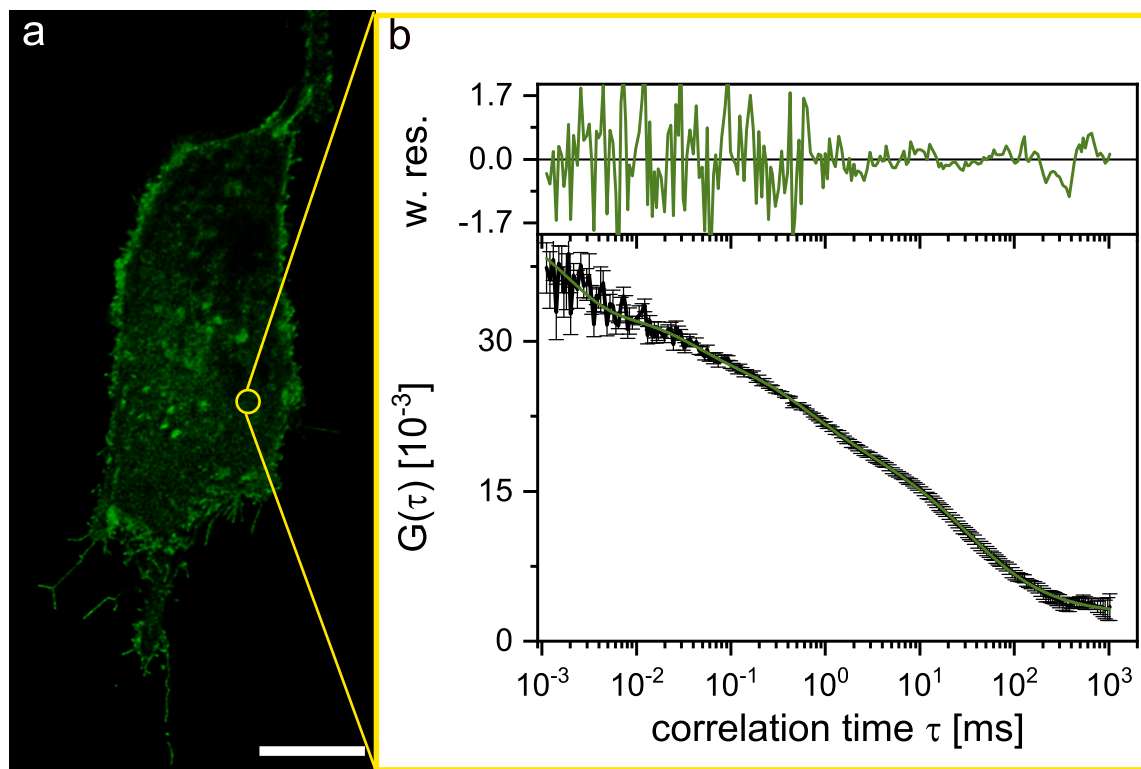**Figure 4.6: Scheme of a spectroscopy measurement. a**. An example image of the basal membrane from a CHO-K1 cell expressing β_2-AR$^{IL3-EGFP}$, the yellow spot (not to scale, 0.7 µm diameter for this measurement) indicates the confocal spot where the spectrometric measurement was made. Scale is 10 µm. **b**. ACF (with standard error) calculated from the intensity fluctuations at the yellow spot, fitted with equation (3.13). The number of fluorescent receptors in the detection volume is 38, with a fraction of 0.4 of the molecules exhibiting a diffusion time, τ_d of 0.6 ms and the rest exhibiting τ_d of 35 ms. In addition, two relaxation times (triplet or other fast kinetics) of 35 µs and 2 µs are derived from the fit. Top window gives the weighted residuals corresponding to the fit.

4.3   Time-resolved fluorescence spectroscopy measurements on β_2-AR

After the constructs were characterised, I started with the fluorescence spectroscopy measurements. Theory 2.2.1, 2.2.2 and 2.2.4 explains in detail how and what data is acquired in a time-resolved fluorescence spectroscopy measurement. Briefly, for a live cell measurement the focus was set to the basolateral membrane of a cell and data acquired for ~5 min. Methods 3.4.5 explains in more detail how live cell measurements are performed on the time-resolved fluorescence spectroscopy setup.

The experiments were conducted with the 100 µm pinhole and both detectors and the cells which

expressed fluorescent receptors below 200 were chosen for further measurement as a high particle number would lead to photobleaching and artefacts in the ACF in addition to a low correlation amplitude (equation (2.20)). This led to measuring the cells with less particle number for five minutes or a max photon counts of 8,000 to 10,000 to get a good signal to noise ratio in terms of anisotropy. The cells measured this way produced TTTR data which had macro time intensity fluctuations which could be used for calculating ACF and also the micro time fluorescence decay which could be globally fitted to derive the rotational diffusion/anisotropy underlying in the sample. Briefly, the photon traces acquired were software correlated and fitted with equations (3.10)-(3.13) to find the best fit. The fluorescence decay histograms acquired from the same measurement were globally fitted with equations (3.7) and (3.8). Any measurement in which either of both data could not be fitted or were artefact prone were discarded as only the cells in which both translational and rotational mobility could be acquired can be used to understand the complete dynamic fingerprint of β_2-AR.

4.4 β_2-AR translational diffusion

The macro time intensity fluctuations from a live cell measurement were autocorrelated in SymPhoTime64 where I could check the intensity fluctuations myself by eye. Figure 4.7a shows an intensity trace measured from a CHO-K1 cell expressing β_2-AR^{SNAP} and there is no photobleaching prominently present. If a cell, which was undergoing rapid photobleaching was picked the measurement was discarded. On the other hand, if the photobleaching was only towards the end, the initial part was chosen for correlating. This way, most photobleaching artefacts could be avoided. Figure 4.7b shows a live cell measurement where bleaching was prominent and was discarded. Even if the first 40 s shown as inlay was correlated, there were still bleaching artefacts. The autocorrelation function (ACF) extracted from the intensity fluctuations were then fitted with the model (equations (3.12), (3.11), (3.10) and (3.13)) that best described the underlying kinetics and diffusion dynamics.

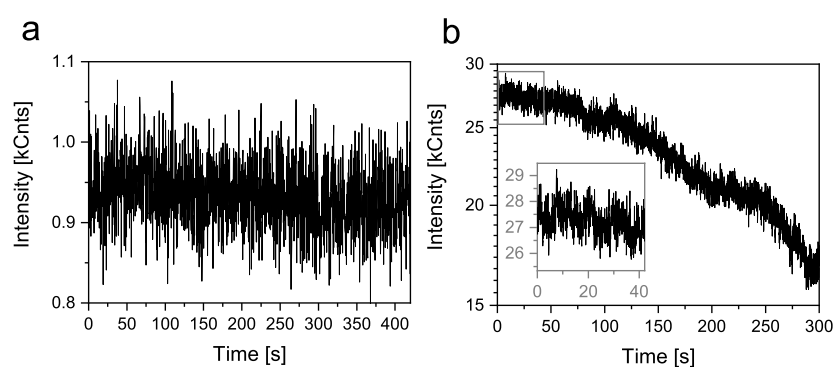**Figure 4.7: Avoiding artefacts from photobleaching. a.** Ideal fluorescence intensity trace of a live cell measurement. **b.** Fluorescence intensity trace of a live cell measurement which underwent considerable photobleaching. To avoid artefacts from photobleaching only the first 40 s were correlated (shown in the inlay, which in turn is an expanded view of the grey box overlaying the original time trace).

4.4.1 Live cell ACF fitting

The ACF that was calculated from the selected intensity fluctuation was fitted with different models to find the model which could best describe the ACF. The fit was checked visually from its residuals and the adjusted R² value. From visual inspection of an ACF it is clear that it needs multiple terms to describe it, not only a diffusion term and a relaxation term which is the norm. I tried different models 1 (equation (3.10)), 2 (equation (3.11)) and 3 (equation (3.12)). Briefly, model 1 describes the ACF to have one 2D diffusion, one 3D diffusion and one relaxation component; model 2 describes the ACF to have two 2D diffusion and one relaxation component and model 3 describes the ACF to have a 2D diffusion component and two relaxation terms. For the representative cell in figure 4.8a model 1 fits the ACF quite good and has an adjusted R² of 0.978, it gives τ_{3D} of ~1 ms, τ_{2D} of ~88 ms and τ_T of ~13.03 μs. Model 2 also exhibits minimal deviations in its residuals and seems to be equally good as model 1 and has an adjusted R² of 0.975, τ_{2D1} of ~1 ms, τ_{2D2} of ~93 ms and τ_T of ~5.00 μs. With model 3 it is clearly discernible that its residuals deviate a lot and does not fit the ACF in its totality although its adjusted R² value is on par with model 1 and model 2. Although the diffusion times from fitting with model 1 and model 2 were more or less the same, the concept of a fast 2D translational diffusion on the plasma membrane seemed improbable. Hence, model 1 was used to fit most of the cells. In some cases, as in figure 4.6, an extra relaxation term was needed. Model 4 serves this purpose as it is an extension of model 1 and has an additional relaxation term. For figure 4.6 this additional relaxation was ~2 μs.
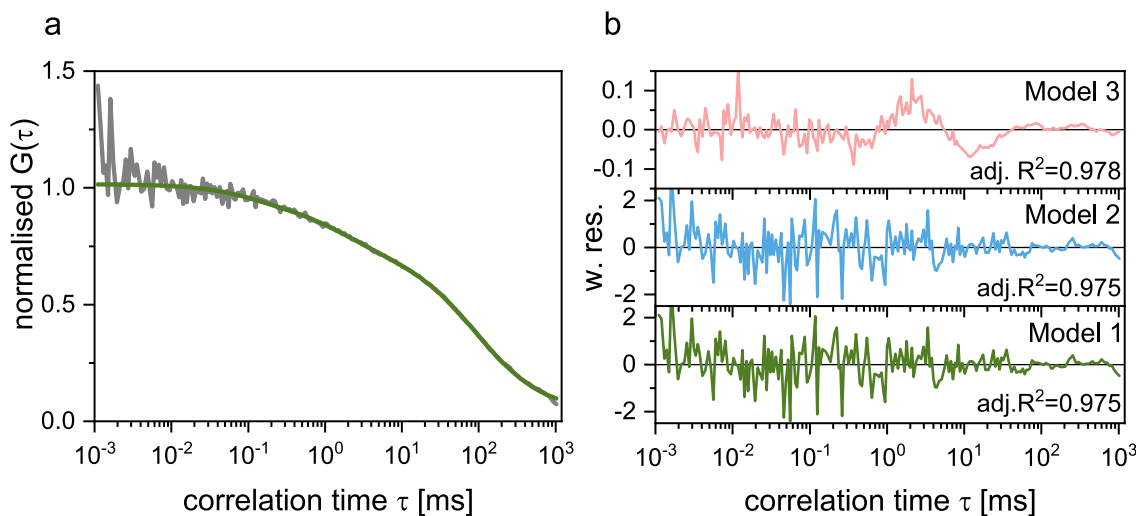

Figure 4.8: Fitting the ACF from live cells. a. ACF (grey) calculated from the intensity fluctuations measured on the basal membrane of a CHO-K1 cell expressing β_2-AR[NT-EGFP]. A fit with Model 1 (equation (3.10)) is given as overlay in green. **b.** Weighted residuals corresponding to the ACF in **a** fit with different models. Top in pink gives the residuals corresponding to the fit with model 3 (2d2t, equation (3.12)). Middle in blue gives the residuals corresponding to the fit with model 2 (22dt, equation (3.11)). Bottom in green gives the residuals corresponding to the fit with model 1 (2d3dt, equation (3.10)).

4.4.2 β_2-AR exhibits translational diffusion in two different timescales

Model 1 described the data best for all constructs and all constructs regardless of their tags exhibited two diffusion components as shown in figure 4.9. They exhibited a slow diffusion constant, D_{slow} in the range of 0.05 - 0.13 µm²/s and a fast diffusion constant, D_{fast} in the range of 3 - 20 µm²/s. One exception was the fraction of the fast component, x_{fast} that each construct exhibited, which was quite less for β_2-AR^{SNAP} with only 0.07 while it was 0.33 for β_2-AR$^{NT-EGFP}$, 0.31 for β_2-AR$^{IL3-EGFP}$ and 0.27 with a wider distribution for β_2-AR^{A186TCO}. α_{2A}-AR$^{NT-EGFP}$ and α_{2A}-AR^{SNAP} were measured as controls and found two similar diffusion constants. The diffusion constants and the fast fraction from the fit results are summarised in table 4.1 and the complete fit results are summarised in table 4.7.

Table 4.1: Summary of diffusion times from FCS fits.

Construct	D_{slow} (µm²/s)	D_{fast} (µm²/s)	x_{fast}
β_2-AR$^{NT-EGFP}$	0.10 ± 0.02	6.08 ± 2.80	0.33 ± 0.05
β_2-AR$^{IL3-EGFP}$	0.13 ± 0.06	8.09 ± 3.65	0.31 ± 0.04
β_2-AR^{SNAP}	0.06 ± 0.03	11.0 ± 13.2	0.07 ± 0.03
β_2-AR^{A186TCO}	0.06 ± 0.01	4.74 ± 1.36	0.27 ± 0.10
α_{2A}-AR$^{NT-EGFP}$	0.08 ± 0.08	6.29 ± 3.18	0.34 ± 0.07
α_{2A}-AR^{SNAP}	0.11 ± 0.05	43.3 ± 34.3	0.10 ± 0.05

The perplexing question was why is there a fast diffusion component in the first place and if it is cell bound what could its significance be. There have been previous reports that it could be caused due to photophysics or free fluorophore in solution [164]. But in this case, it was clear that the 0.5-2 ms diffusion was not arising from photophysics as EGFP, AF488 and ATTO 488 photophysics all occur in the tens of µs range [165–167]. One straightforward experiment to rule out if the component arises from diffusion was changing the pinhole size to see how it behaves. Figure 4.10 shows diffusion times extracted from fitted cells measured using different pinhole sizes, and it is clear that both the components increase in number when the detection volume increases whereas in the case of photophysics, it should be independent of the detection volume as it is an electronic process (figure 2.1). The second reported source of the fast component was free fluorophore in the cytosol. Initial calculation of translational diffusion constants for the fluorophores and receptor constructs were done on HYDROPRO [157] with the assumption of cytoplasmic viscosity as 1 cP [168, 169] to get an understanding of what diffusion constants free fluorescent receptors and fluorophores in cytosol might possess. Table 4.2 summarises the results which shows the diffusion constants of free fluorophores to be an order of magnitude faster than what is calculated from the fits. These values give a range in which the diffusion constants of free receptors or fluorophores could be expected and it has to be noted that recent findings show that the cytosol behaves more as a gel than an aqueous solution with its viscosity being dynamic and dependent on the region within the cell [170, 171].
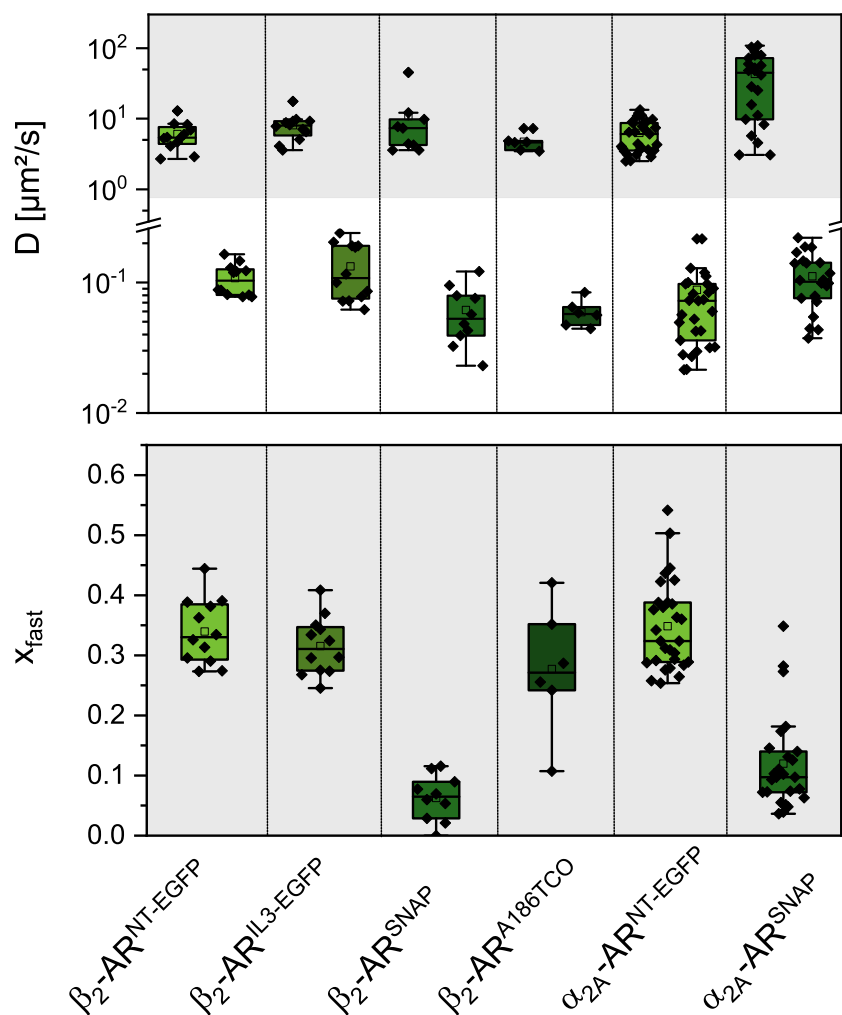
Figure 4.9: β_2-AR exhibits two diffusion constants over all constructs. Diffusion constants (D_{fast}, D_{slow}, top) and fraction of molecules exhibiting D_{fast}(x_{fast}, bottom) of all β_2-AR and α_{2A}-AR constructs used in this work. D_{fast} and D_{slow} were calculated from the corresponding diffusion times τ_{d1} and τ_{d2} respectively from fitting with equation (3.10), x_{fast} was directly obtained from the same fits. β_2-AR$^{NT-EGFP}$ (light green) exhibits D_{fast} of 6.08 ± 2.80 µm²/s, D_{slow} of 0.10 ± 0.02 µm²/s and x_{fast} of 0.33 ± 0.05 for n = 12, β_2-AR$^{IL3-EGFP}$ (green) exhibits D_{fast} of 8.09 ± 3.65 µm²/s, D_{slow} of 0.13 ± 0.06 µm²/s and x_{fast} of 0.31 ± 0.04 for n = 12, β_2-AR^{SNAP} (meadow green) exhibits a D_{fast} of 11.0 ± 13.2 µm²/s, D_{slow} of 0.06 ± 0.03 µm²/s and x_{fast} of 0.07 ± 0.03 for n = 10, β_2-AR^{A186TCO} (dark green) exhibits a D_{fast} of 4.74 ± 1.36 µm²/s, D_{slow} of 0.06 ± 0.01 µm²/s and x_{fast} of 0.27 ± 0.10 for n = 6, α_{2A}-AR$^{NT-EGFP}$ (light green) exhibits a D_{fast} of 6.29 ± 3.18 µm²/s, D_{slow} of 0.08 ± 0.08 µm²/s and x_{fast} of 0.34 ± 0.07 for n = 19 and α_{2A}-AR^{SNAP} (meadow green) exhibits a D_{fast} of 43.3 ± 34.3 µm²/s, D_{slow} of 0.11 ± 0.05 µm²/s and x_{fast} of 0.10 ± 0.05 for n = 22. Data are mean ± s.d. The light grey background on both the top and bottom plots signify values corresponding to molecules exhibiting D_{fast}.

Table 4.2: HYDROPRO results for fluorophores and receptor constructs.

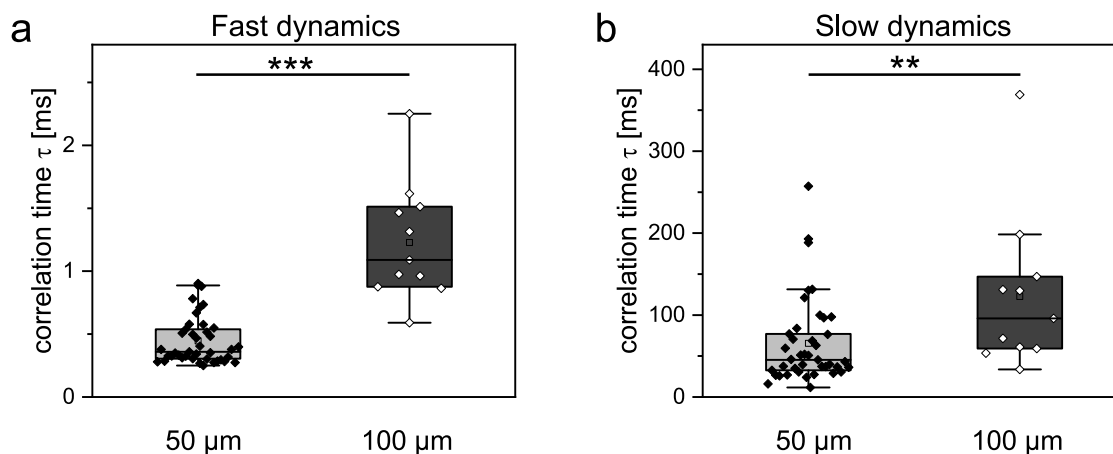| Molecule	Translational diffusion coefficient (µm²/s) at 20 °C and 1 cP
GFP (PDB: 3EVP [172])	~90
SNAP bound to substrate (PDB: 3KZZ [173])	~100
Tet-ATTO dye	~260
β_2-AR (PDB: 2RH1 [21])	~80
β_2-AR$^{NT-EGFP}$ (PDB: 2RH1 [21], 2Y0G [174])	~60
β_2-AR^{SNAP} (PDB: 2RH1 [21], 3KZZ [173])	~60

Figure 4.10: Fast dynamics exhibited by β_2-AR originates from diffusion. Correlation times obtained from fitting data measured using pinhole diameter sizes of 50 and 100 µm thereby changing the effective confocal detection volume. Data were acquired from CHO-K1 cells expressing β_2-AR$^{NT\text{-}EGFP}$. **a**. Correlation time of the fast dynamics from 50 µm measurement is 0.45 ± 0.19 ms and from 100 µm measurement is 1.23 ± 0.44 ms. Diffusive processes exhibit a higher dynamic time as the effective volume is increased whereas photophysical processes are independent of the effective volume. The 100 µm pinhole creates a larger effective volume relative to the 50 µm. Here, the 100 µm measurement shows a significant increase in the correlation time over the 50 µm measurement. **b**. Correlation time of slow dynamics stemming from plasma membrane bound receptors exhibit a similar pattern. 50 µm measurement gives 73.04 ± 71.41 ms while the 100 µm measurement gives 170.73 ± 189.59 ms. $* * *$ is P<0.001, $**$ is P<0.05.

Different hypotheses were tested to pin down the source of the fast component.

Artefact caused due to basal versus apical membrane mobility

Spectroscopy measurements were performed in the basal membrane directly attached to the coverslip. One possibility is that the receptors exhibit different diffusion constants on the basal and apical membranes, since the basal membrane is bound to the coverslip while the apical membrane is open to the bulk media. Measurements from the apical membrane showed almost double the number of receptors relative to measurements on the basal membrane but similar distribution of diffusion constants/receptor mobility and fraction of the fast diffusing molecules (figure 4.11a-c). Hence, the attachment (through extracellular matrices) of cells to the glass coverslip does not affect mobility behaviour of the receptors.

Receptor densities influence mobility constants

A recent study by Wäldchen et al., has shown that the density of receptors on the apical and basal membrane are different by using 3D lattice light-sheet *d*STORM [175]. This is in line with the FCS measurements at the basal and apical membrane. However, there was no correlation between receptor concentration and mobility (figure 4.11d), suggesting that receptor clustering or oligomerisation if present, does not affect receptor mobility. Receptor concentration was recalculated for all constructs based on the effective detection volume (Methods 3.4.3) and the number of molecules in focus calculated from fitting the ACF.

Intracellular diffusion of membrane bound receptor

The effective confocal detection volume has an axial height of ~2 µm (calculated from calibration,
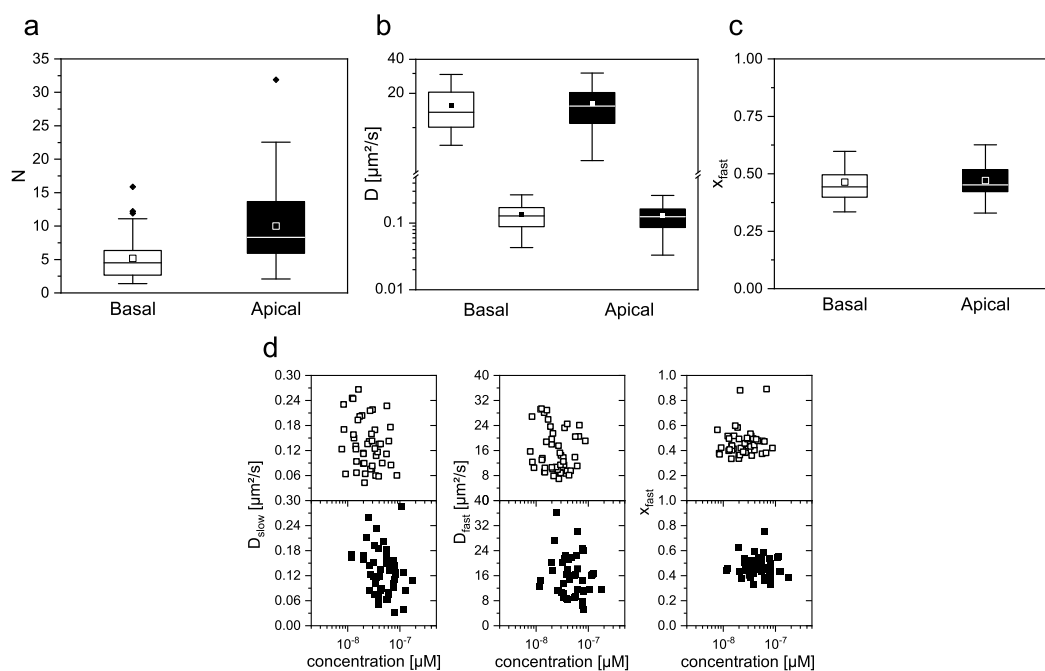
Figure 4.11: Measurement at apical and basal membrane exhibit similar pattern of diffusion times. Translational mobility calculated from CHO-K1 cells expressing β_2-AR$^{NT\text{-}EGFP}$ measured with the focal spot positioned on the basal and apical plasma membrane. **a.** Number of fluorescent receptors in the basal (5.2 ± 3.2) and apical membrane (10.0 ± 6.0). **b.** Diffusion constants corresponding to the measurement. Basal membrane shows D_{fast} = 16.28 ± 6.95 µm²/s and D_{slow} = 0.17 ± 0.24 µm²/s. Apical membrane shows D_{fast} = 16.84 ± 8.14 µm²/s and D_{slow} = 0.34 ± 1.13 µm²/s. **c.** Fraction of the molecules exhibiting fast diffusion for data acquired from basal and apical plasma membrane. Basal membrane measurement shows x_{fast} = 0.48 ± 0.14 and apical membrane measurement shows x_{fast} = 0.48 ± 0.10. **d.** The mobility measures D_{fast}, D_{slow} and x_{fast} show no dependence on the receptor density in the measured concentration range of 10 nM – 200 nM for the apical and basal membrane comparison. Note: The measurement for this dataset was performed by Dr. Julia Wagner, a former postdoctoral researcher at AG Heinze, University of Würzburg.

Methods 3.4.3) which is relatively much thicker compared to the plasma membrane of a eukaryotic cell which is ~10 nm in thickness [2]. In consequence, fluorescence from molecules inside the cell are also unavoidably collected [137] in addition to plasma membrane bound receptors. Another strong hint that D_{fast} arises from intracellular mobility can be seen from the really low x_{fast} exhibited by β_2-AR^{SNAP} (figure 4.9). As mentioned earlier in this chapter, the organic fluorophore (SNAP Surface Alexa Fluor 488) used for labelling β_2-AR^{SNAP} is membrane impermeable. This means that only the plasma membrane bound receptors are labelled, hence the low x_{fast} relative to other constructs in this work. This assumption is further strengthened by the low x_{fast} calculated for α_{2A}-AR^{SNAP}.

To shed light into this further, I measured at different axial points in the cell, not just the basolateral membrane, by shifting the focus from the basolateral membrane to the apical membrane. The ACFs derived from these measurements were fit using Model 1 (equation (3.10)). Figure 4.12 shows how the fast component derived from these fits varies with the region (focus either centred or decentred to the plasma membrane) where the measurement was made. The fast fraction increases as the focal volume moves more into the cell and decreases when reaching the apical membrane. In turn, molecules exhibiting D_{slow} were more pronounced for focus positions centred on the plasma membrane, regardless of being basal or apical, signifying that the fast component arises from the
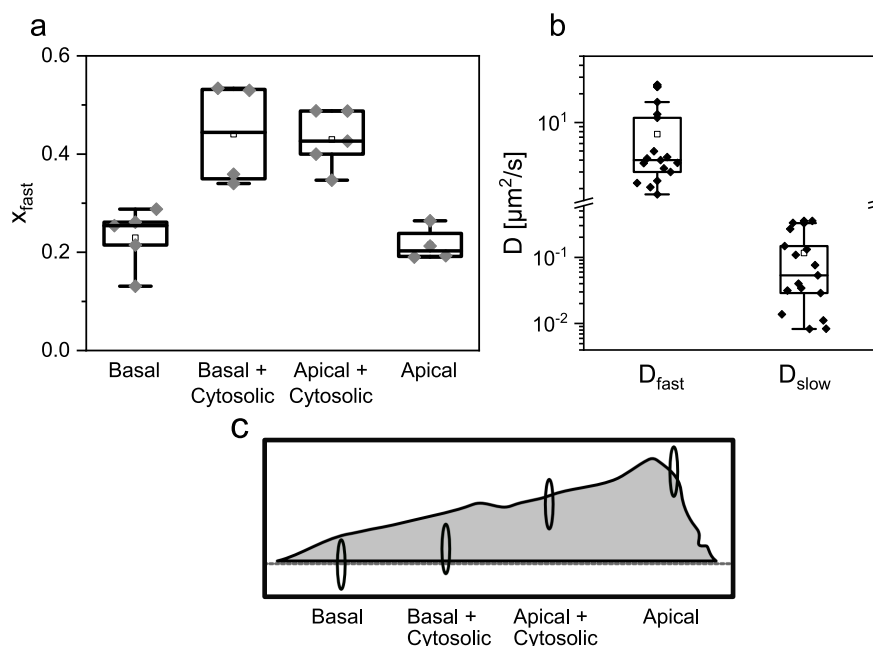
cytosol.

Figure 4.12: Changing focal volume position shows that the fast diffusion arises from the cytosol.
Mobility parameters calculated from measurements made on CHO-K1 cells expressing β_2-AR$^{NT-EGFP}$ with the focal volume centred and decentred on the basal and apical plasma membrane. **a**. x_{fast} corresponding to the measurements made at different positions, Basal 0.22 ± 0.06; Basal + Cytosolic 0.44 ± 0.10; Apical + Cytosolic 0.42 ± 0.06; Apical 0.21 ± 0.03. **b**. Diffusion constants from measurements at all positions pooled together, the receptors exhibit a D_{fast} of 7.54 ± 7.51 μm^2/s and D_{slow} of 0.11 ± 0.12 μm^2/s. Data are mean $\pm$ s.d. **c**. Cartoon representing the different focal positions. The focal volume and the dimension of the cell are drawn to scale. The dimensions of the focal volume are 2.72×0.46 μm^2 and the dimensions of the representative cell are 9×40 μm^2.

To recapitulate, the low x_{fast} of β_2-AR^{SNAP} and axial scanning through cells agree that D_{fast} arises from within the cell and not the plasma membrane. In addition, the theoretical simulation with HYDROPRO gave a hint that the source of D_{fast} could not be free fluorophores in the cytosol.

To zero in on the source of this intracellular mobility further, a western blot was performed on fractionated cytosol, membrane and whole cell lysate. Kerstin Jansen helped me by performing the fractionation and western blot which are shown in figure 4.13. As controls CHO-K1 cell stably expressing β_2-AR [176] and purified GFP were used. Two different secondary antibodies were selected for the experiment. One against β_2-AR and one against EGFP, to know if EGFP is truncated. The full-length β_2-AR$^{NT-EGFP}$ has a molecular weight of ~90 kDa when glycosylated and 75 kDa when not. Truncated EGFP has a molecular weight of ~30 kDa. It can be seen from figure 4.13a-b that the cytosol does not show any signal either for the antibody against β_2-AR or for the one against EGFP, meaning that both β_2-AR$^{NT-EGFP}$ and truncated EGFP are absent in the cytosol. This in turn indirectly tells that the protein is still bound to some membrane in addition to the confirmation from the two bands of ~90 and 75 kDa in the membrane fraction, albeit not the plasma membrane as inferred from the results before. No truncated EGFP in the cytosol means that the protein is not being spliced by proteases inside the cell. Figure 4.13c-d shows antibody staining for Gβ, which was performed as a control for the amount of protein loaded in each well. This was done by first stripping the blot from antibodies against β_2-AR and EGFP. The interaction of the anti-GFP antibody was so strong that it could not stripped perfectly, which is visible in figure

4.13c, but Gβ band is still visible. To sum up, the western blot shows that there is no fluorescent receptor freely diffusing in the cytosol and that all fluorescent receptors are membrane bound. One possible candidate for the source inside the cell could be vesicular transport, which can possess similar mobility [177, 178]. All results from FCS are summarised in table 4.7.
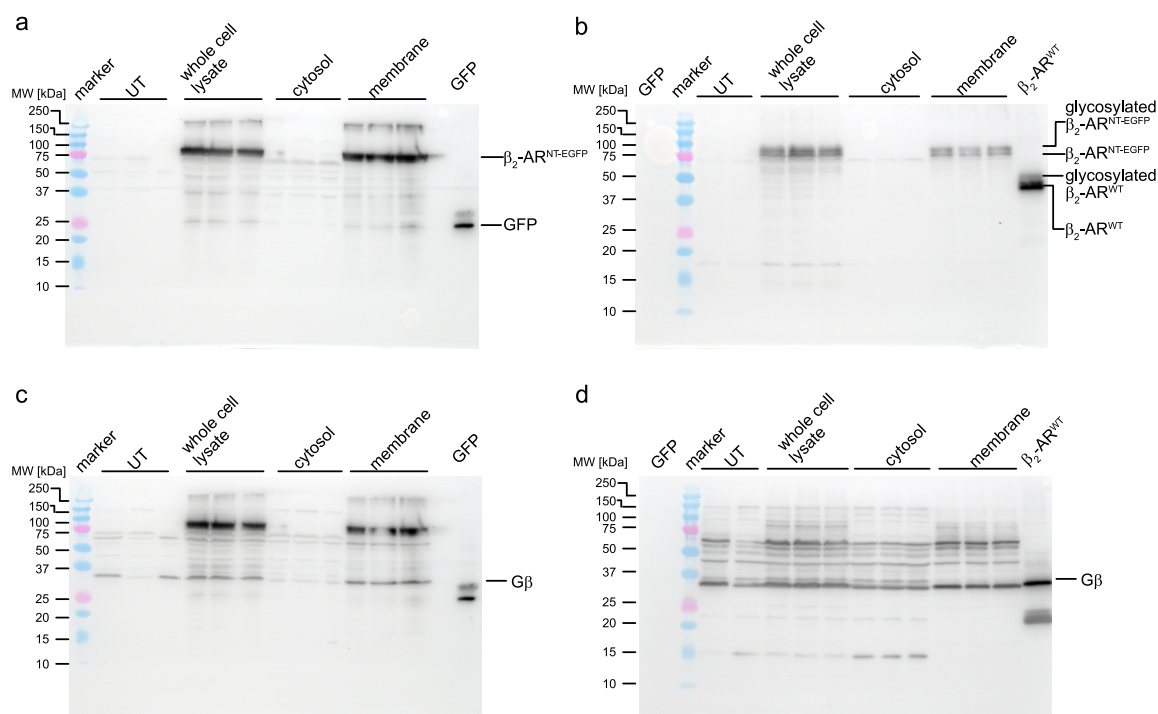

Figure 4.13: Western blot shows that the source of fast diffusion is membrane bound receptor. Western blot of fractionated cytosol, membrane and whole cell lysate. GFP and the whole cell lysate of CHO-K1 cell expressing β_2-AR^{WT} were used as positive controls for the respective antibodies against GFP and β_2-AR. As negative control for antibody specificity untransfected cells (UT) were fractionated and tested. Gβ was used as control for the concentration of protein loaded in each well.**a**. Anti-GFP western blot, The three lanes of UT are cytosol fraction, membrane fraction and whole cell lysate respectively. The dark bands visible ~90 kDa show the presence of β_2-AR$^{NT-EGFP}$ in the whole cell lysate and membrane fractions of transfected cells. GFP can be seen as the band at ~30 kDa. The corresponding anti-Gβ western blot is given in **c**. The bands from the anti-GFP antibody could not be completely stripped off and can be seen in addition to the band corresponding to Gβ at ~37 kDa. **b**. Anti-β_2-AR western blot. The first lane has GFP, acting as another negative control in addition to UT. In this case only the whole cell lysate and cytosolic fraction were used for UT in lane 3 and 4 respectively. Whole cell lysate and membrane fractions of transfected cells show two bands around 75-100 kDa corresponding to the glycosylated and non-glycosylated versions of β_2-AR$^{NT-EGFP}$. β_2-AR^{WT} can be seen as the two bands at ~50 kDa and no truncated β_2-AR can be seen from the fractions. The corresponding anti-Gβ western blot is given in **d**. Overall both anti-GFP and anti-β_2-AR western blots show the absence of any receptors in the cytosol.

4.5 β_2-AR shows fast rotational correlation consistent with earlier observations

The time-resolved fluorescence spectroscopy setup as described in the Methods 3.4.1 has two detectors capable of resolving polarisation. By exciting with a plane polarised light source (485 nm laser) and resolving the obtained fluorescence into parallel and perpendicular polarisation to the plane of excitation we can calculate the rotational correlation time that a molecule within the focal

volume possesses. Microtimes recorded during the measurement from the parallel and perpendicular channels, constitute the fluorescence decay histograms and could be fitted to derive the rotational diffusion of a molecule or the changes in orientation of a molecule as mentioned in theory 2.2.1, in this case, the fluorescent receptor. It has to be noted that by rotational correlation time or diffusion, it does not necessarily mean that the fluorescent receptor is rotating around its own axis rather that the protein wobbles with its orientation changing at a certain rate. The fluorescence decays from live cell measurements were jointly fitted (i.e., the fluorescence lifetime and rotational correlation time parameters when fitted converged to the same global minima for both VV and VH fluorescence decays) as mentioned in Methods 3.5.1 by a global fit using equations (3.7) and (3.8) with multiexponential fluorescent times and a biexponential rotational correlation time. The biexponential rotational correlation time arises from freedom of movement of the fluorophore head group in addition to the wobbling of the protein. In case of small organic dyes, rotational diffusion arising from free dye movement can be clearly discerned from that of the bulky protein. Hence, for β_2-AR^{A186TCO}, a triexponential rotational correlation time fit was needed to describe the decay better. For interpretation only the slowest rotational correlation time was taken as that should be associated with the wobbling of the protein. The fundamental anisotropy of EGFP, AF488 and ATTO 488 were fixed to 0.38 as shown in literature [154, 155]. Figure 4.14 shows a representative set of fluorescence decays obtained from a live cell measurement globally fitted to give a rotational correlation time (τ_{rot}) of 39 ns. The initial fast decay due to fluorophore rotation (< 1 ns) can be differentiated from the slower rotation (> 20 ns).
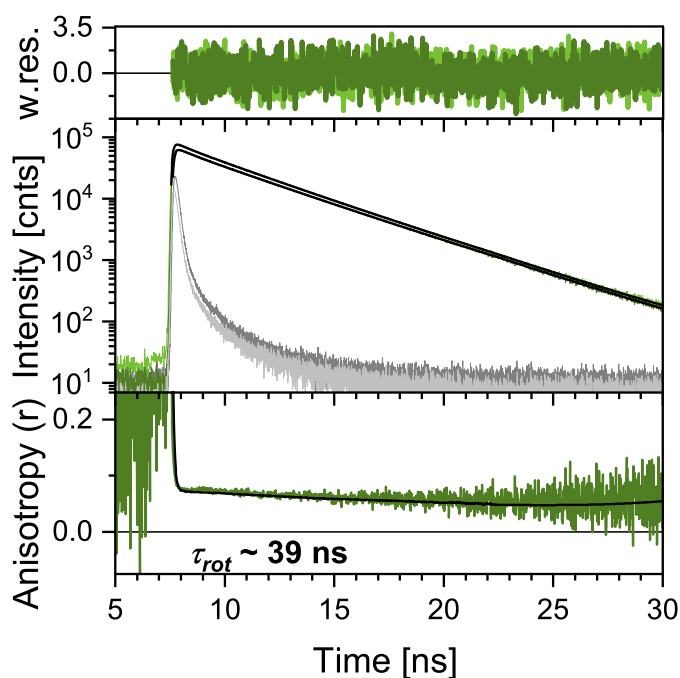
Figure 4.14: Representative global fit for a set of fluorescence decays. Global fit of photon arrival time histograms of VV (green) and VH (light green) polarised fluorescence photons from CHO-K1 cells expressing β_2-AR^{SNAP}. The IRF corresponding to VV and VH are shown in grey and dark grey respectively. The fits from equations (3.7) and (3.8) are given in black. The fit gave a rotational correlation time (τ_{rot}) of 39 ns. Weighted residuals corresponding to the global fit are shown on top and reconstructed anisotropy decay and its fit are shown at the bottom.

Figure 4.15 shows the summary of all fits and all constructs show times in the range between

20-300 ns. This would signify a really fast wobbling motion from the receptor which albeit reported before in Spille et al. [80] contradicts the Saffman-Delbrück model for diffusion of membrane proteins. The Saffman-Delbrück model predicts a rotational correlation time in the µs for the adrenergic receptor. Time-resolved anisotropy in effect is limited by the fluorescence lifetime of the probe/fluorophore used, which, in our case, being either EGFP, AF488 or ATTO 488 all range between 2.9-4.1 ns. Rotational correlation times above 50 ns calculated from fits have a large uncertainty. The τ_{rot} results are summarised in table 4.3 and all results from TRA are summarised in table 4.8.

Table 4.3: Summary of rotational correlation times from TRA fits.

Construct	τ_{rot} (ns)	r_{ss}
β_2-AR[NT-EGFP]	113.7 ± 70.5	0.10 ± 0.02
β_2-AR[IL3-EGFP]	165.1 ± 14.6	0.13 ± 0.02
β_2-AR[SNAP]	40.0 ± 27.5	0.08 ± 0.01
β_2-AR[A186TCO]	118.3 ± 51.8	0.10 ± 0.01
α_{2A}-AR[NT-EGFP]	177.0 ± 20.8	0.10 ± 0.01
α_{2A}-AR[SNAP]	50.3 ± 9.2	0.10 ± 0.01
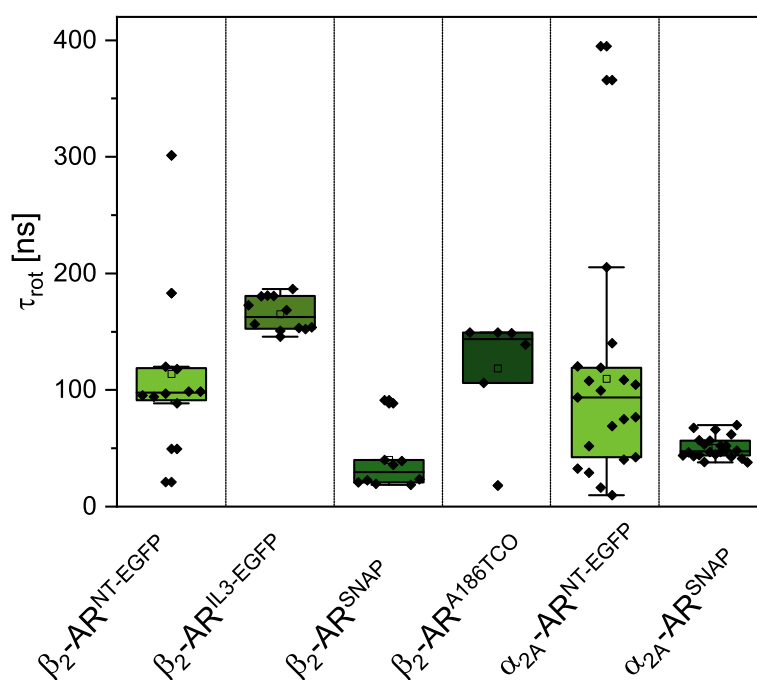
Figure 4.15: Rotational correlation times of all constructs. Rotational correlation time of all constructs calculated from the global fits. β_2-AR[NT-EGFP] shows 113.7 ± 70.5 ns; β_2-AR[IL3-EGFP] shows 165.1 ± 14.6 ns; β_2-AR[SNAP] shows 40.0 ± 27.5 ns; β_2-AR[A186TCO] shows 118.3 ± 51.8 ns; α_{2A}-AR[NT-EGFP] shows 81 ± 48 ns and α_{2A}-AR[SNAP] shows 37 ± 15 ns. The colour scheme is the same as in figure 4.9.

4.6   Homo-FRET and influence of receptor density

Owing to the FCS and TRA data being obtained from the same intensity traces, both data can be directly compared and related. One question that could be answered by comparing them is the oligomerisation state of the receptors. One way is to look at the influence of receptor density/concentration on the derived translational and rotational diffusion constants. The concentration was calculated from the number of fluorescent receptors in the plasma membrane and the effective detection confocal volume from calibration (Methods 3.4.3). Figure 4.16 shows the concentration of receptors in the plasma membrane correlated against the mobility parameters calculated from both FCS and TRA fit results. D_{fast} of β_2-AR^{A186TCO} shows a slight dependence on concentration, D_{fast} decreases with increase in concentration (figure 4.16a, lower left corner). τ_{rot} of β_2-AR^{SNAP} also shows dependence on receptor concentration, it decreases with increasing concentration (figure 4.16d, upper right corner). Mobility parameters in the case of all constructs other than these do not show a correlation towards receptor concentration.
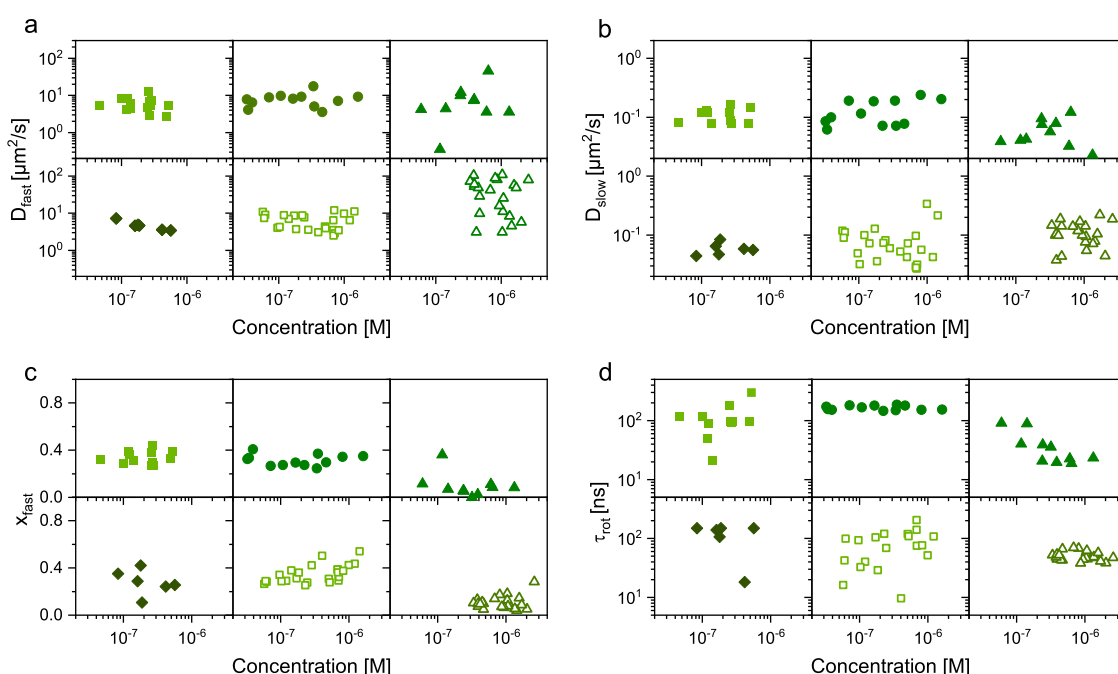

Figure 4.16: Receptor density does not influence receptor mobility. The concentration of receptors (20 nM to 5 µm) does not seem to influence the diffusion constants D_{fast} (**a**), D_{slow} (**b**), the fraction of the fast diffusing molecules, x_{fast} (**c**) and rotational correlation time, τ_{rot} (**d**) for all β_2-AR and α_{2A}-AR constructs used in this work. The clear exceptions include the D_{fast} in the case of β_2-AR^{A186TCO} (a, lower left corner) and τ_{rot} in the case of β_2-AR^{SNAP} (d, upper right corner). Squares represent β_2-AR$^{NT-EGFP}$, circles represent β_2-AR$^{IL3-EGFP}$, triangles represent β_2-AR^{SNAP}, diamonds represent β_2-AR^{A186TCO}, Empty squares represent α_{2A}-AR$^{NT-EGFP}$ and α_{2A}-AR^{SNAP}. The colour code follows the same as in figure 4.9.

Another approach is to identify the presence or absence of Homo-FRET, which is an electronic transition that happens between identical fluorophores (Theory 2.2.3) when they come closer than 10 Å . Presence of Homo-FRET would signify that there is some form of clustering in the sample. Homo-FRET would be reflected as a decrease in the steady-state anisotropy (r_{ss}) or final anisotropy (r_{inf}) with increase in receptor concentration. Figure 4.17 shows the receptor concentration plotted against r_{ss} and no change in r_{ss} can be seen with the receptor concentrations between 20 nM and

5 μm, although the r_{ss} values are low for all. Hence, both results point at the absence of clustering because of receptor crowding but a presence of oligomerisation in the basal state.
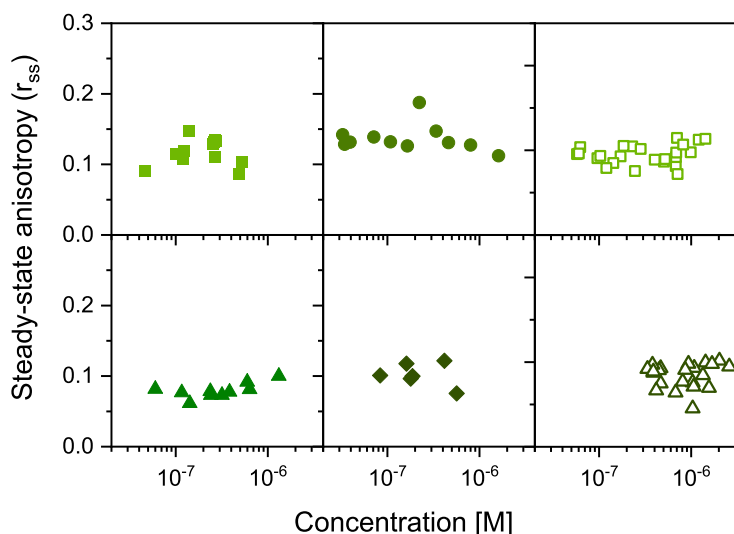

Figure 4.17: β₂-AR and α₂A-AR show absence of Homo-FRET. r_{ss} of all constructs plotted against receptor concentration. r_{ss} seems independent of receptor concentration, thereby showing an absence of Homo-FRET. r_{ss} was calculated from the photon arrival time histogram data. The colour code is the same as in figure 4.9.

4.7 fullFCS reveals an additional rotational correlation time in β₂-AR

With Time-resolved fluorescence spectroscopy using pulsed laser excitation combined polarisation resolved detection and TCSPC electronics it is possible to simultaneously study translational dynamics and rotational dynamics using time-resolved anisotropy and fluorescence correlation spectroscopy. But FCS and TRA in our case are privy to the μs region hence creating a blindspot which effectively is not being covered. FCS and TRA data shows the presence of two translational diffusion constants and only one rotational correlation time. In addition to this, the Saffman-Delbrück model predicts a much slower rotational correlation time in the μs range as mentioned earlier. In order to measure dynamics in the μs range a polarisation resolved fullFCS approach was used. fullFCS makes use of a cw-mode laser excitation and polarisation resolved detection, to correlate intensity fluctuations and show dynamics from ps to s, thereby covering the blindspot between FCS and TRA.

I performed fullFCS on CHO-K1 cells expressing β₂-AR[NT-EGFP] and β₂-AR[SNAP]. These two constructs were selected on the basis of the fluorophores, one representative for fluorescent protein (β₂-AR[NT-EGFP]) and one for organic fluorophore (β₂-AR[SNAP]). One limitation of the fullFCS measurement is its measurement time. To get a reasonable signal to noise ratio in the μs range cells had to be measured for 20 - 40 min. In essence, long measurement times lead to photobleaching and aggregate formation which in turn show up as artefacts in all correlation curves. In order to overcome this, Dr. Katherina Hemmen performed data analysis by adapting an approach as described in Ries et al. [129] where it is possible to automate FCS data analysis with

efficient rejection of corrupted parts of the signal (Methods 3.5.3). The approach schematically shown in figure 4.18 is explained in Methods 3.5.3. Briefly, the intensity time traces were split into pieces from 5-60 s (figure 4.18a) and correlated depending on the slice width (i.e., If 60 pieces were used for 5 s slices then 5 pieces were used for 60 s slices, such that the total macro time taken into consideration was the same.) (figure 4.18b). The slices were either considered for further analysis and comparison or discarded based on the mean square deviation (equation (3.16), figure 4.18c). The selected correlation curves for each measurement were then globally fitted with equation (3.17). This approach enabled fullFCS measurements on live cells despite its large photon statistic required for a good signal to noise ratio.
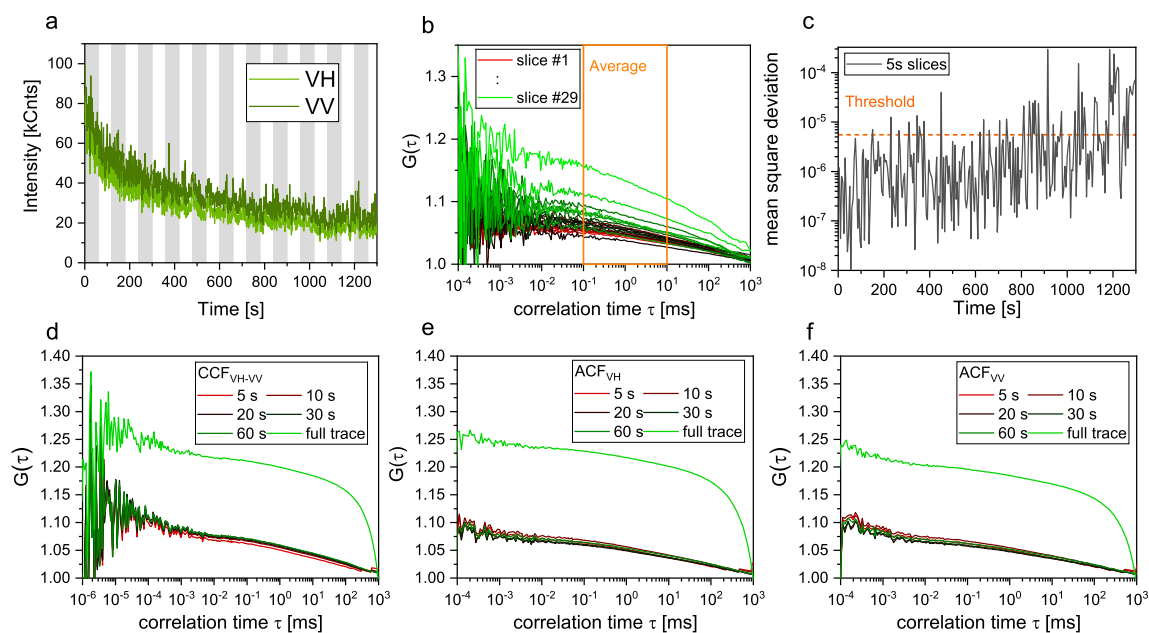

Figure 4.18: The split correlation approach to remove photobleaching artefacts. a. A representative intensity time trace of a CHO-K1 cell expressing β_2-AR$^{NT-EGFP}$, with each grey and white bar having a width of 60 s, representing where the intensity trace was split into single slices. **b**. Each slice was correlated and the average value A_i in the range from 0.1 – 10 ms was calculated (orange box). **c**. The calculated values of A_i were compared to the average of the first n curves (here n = 30) and the mean squared deviation d_i for each curve i was calculated. All curves with a $d_i < d_{max}$ (threshold, orange line, here: 5.5e-6) were averaged and used for further data analysis. **d**. Crosscorrelation curves CCF$_{VH-VV}$ for all time slices and the full trace used as a whole. **e**. Autocorrelation curves ACF$_{VH}$ for all time slices and the full trace used as a whole. **f**. Autocorrelation curves ACF$_{VV}$ for all time slices and the full trace used as a whole.

Figure 4.19 shows a representative fullFCS measurement of a CHO-K1 cell expressing β_2-AR$^{NT-EGFP}$. It shows the crosscorrelation function VV x VH (CCF$_{VV-VH}$, black in figure 4.19), autocorrelation functions (ACF), ACF$_{VV}$ (dark green in figure 4.19), ACF$_{VH}$ (light green in figure 4.19) and the corresponding fits. CCF$_{VV-VH}$ extends to the ns time range and exhibits photon antibunching at ~3 ns which is related to the excited state lifetime of EGFP in this case. By contrast, ACF$_{VV}$ and ACF$_{VH}$ only cover the range up to 100 ns.

In the case of β_2-AR$^{NT-EGFP}$, ACF$_{VH}$, ACF$_{VV}$ and CCF$_{VV-VH}$ showed three additional exponential relaxation times in addition to the two translational diffusion times obtained in FCS fitting (Results 4.4.2). The fastest relaxation time (99 ± 52 ns) agrees well with the rotational correlation time from TRA (113 ± 70 ns) (Results 4.5), thus we named this one τ_{rot}, the two other relaxation times τ_{R1} (1.9
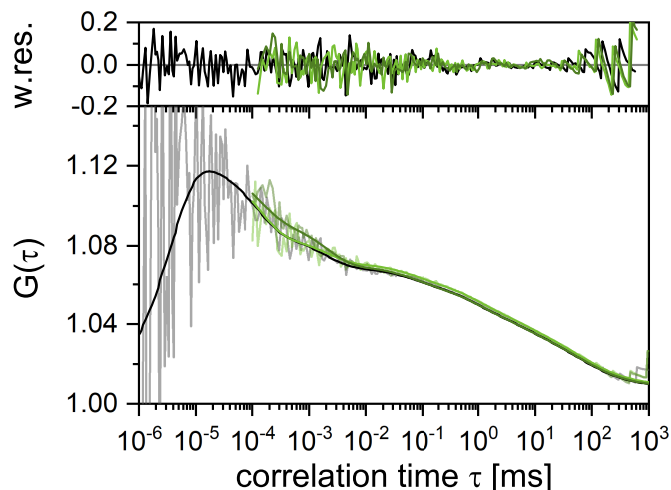
Figure 4.19: Polarisation resolved total correlation from ns to s. A representative fullFCS measurement from a CHO-K1 cell expressing β_2-AR$^{NT\text{-}EGFP}$. The data correspond to 5 s pieces. CCF$_{VV\text{-}VH}$ is shown in black, ACF$_{VV}$ is shown in dark green, ACF$_{VH}$ is shown in light green along with the corresponding fits in the same colour scheme. A difference in amplitude can be clearly seen between the CCF and ACFs. The data were globally fitted with equation (3.17). Weighted residuals are shown on top.

± 0.45 µs) and τ_{R2} (128 $\pm$ 39 µs) are in the µs range. The faster relaxation time τ_{R1} maybe the typical time constant for EGFP photophysics [133]. As mentioned in theory 2.2.2, rotational dynamics can be characterised by differences in the polarisations of the emitted fluorescence after being excited by a plane polarised light. This can be seen as differences in amplitude between ACF$_{VH}$, ACF$_{VV}$ and CCF$_{VV\text{-}VH}$ [130]. In this case, the differences were expected in the 100 ns - 10 µs range. Each set of fitted ACF$_{VH}$, ACF$_{VV}$ and CCF$_{VV\text{-}VH}$ was then compared to see changes in amplitude of the fitted relaxation terms. The absolute difference Δ between the fit results of ACF$_{VV}$ and ACF$_{VH}$ (equation (3.19)) was calculated as a way to visualise this difference (figure 4.20). There were two differences, a minor one at ~50 µs and a prominent one at ~500 ns.
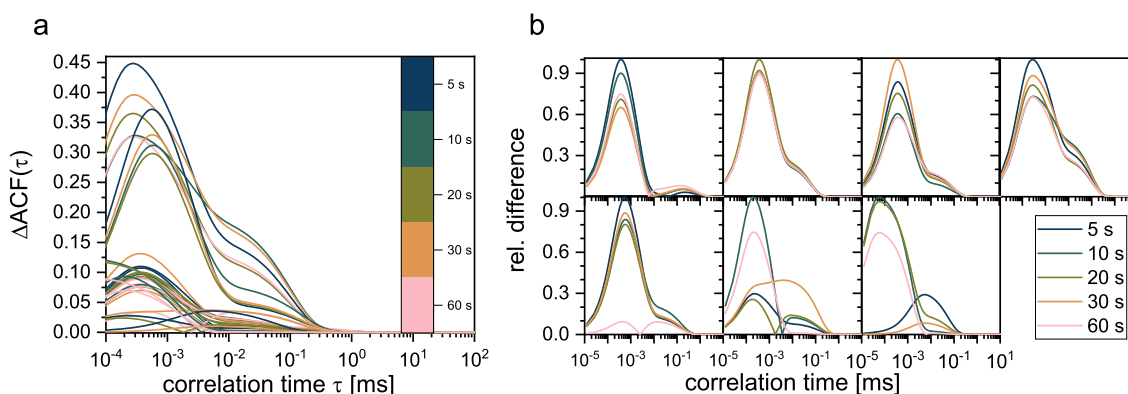
Figure 4.20: Polarisation dependent correlation amplitude difference is visible for fullFCS measurements of β_2-AR$^{NT\text{-}EGFP}$. Correlation amplitude difference between ACF$_{VV}$ and ACF$_{VH}$ for seven cell measurements with each split correlated with slice width of 5-60 s. **a.** The absolute difference in amplitude between ACF$_{VV}$ and ACF$_{VH}$ calculated from the fit parameter (equation (3.19)). **b.** For clarity, the absolute difference shown in **a** for various slice widths are plotted here per measurement and were normalized such that the maximal value per sample reached 1.

To test whether one of the additional relaxation times τ_{R1} and τ_{R2} might reflect a rotational

correlation time that had been missed so far, their fractions were plotted against each other and the fraction of τ_{rot} (figure 4.21a,b,c) and then correlated the amplitude of the identified τ_{rot} with the fraction of slow diffusion (figure 4.21d). Interestingly, the amplitude of τ_{rot} of the ACF_{VH} was negatively correlated with both τ_{R1} and τ_{R2} with correlation coefficients R^2 of 0.89 and 0.82, respectively, while τ_{R1} and τ_{R2} were slightly positively correlated with R^2 of 0.58 (figure 4.21a). The analysis of ACF_{VV} and CCF_{VV-VH} amplitudes shows similar results (figure 4.21c,d). Most important is that the amplitude of τ_{rot} decreased with an increased amount of slow diffusion in the sample, indicating a relation between the fast diffusion and fast rotation, whereas the slower relaxation times, might be associated with the slower diffusion in the membrane.
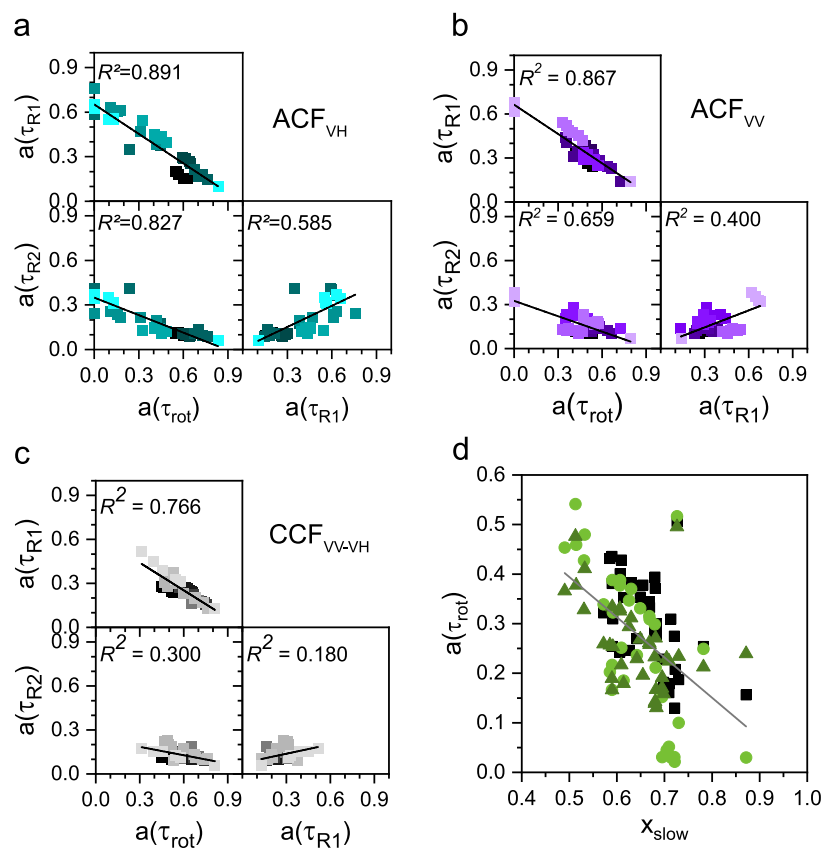
Figure 4.21: β_2-AR$^{NT-EGFP}$ relaxation times correlate with each other. a,b,c. Normalised amplitudes of τ_{rot}, τ_{R1} and τ_{R2} for the ACF_{VH}, ACF_{VV} and CCF_{VV-VH} respectively. Each colour represents measurement from one cell (n = 7). The fit results are summarised in table 4.9. **d**. An increased amount of slow, membrane diffusion, x_{slow}, is related to a decreasing amplitude of τ_{rot}. ACF_{VH} is given in light green circles, ACF_{VV} is given in dark green triangles and CCF_{VV-VH} is given in black squares.

β_2-AR^{SNAP} behaves similar to β_2-AR$^{NT-EGFP}$ except that the fits showed four relaxation times unlike three for β_2-AR$^{NT-EGFP}$. The fastest relaxation time (194 ± 189 ns) also agrees with the rotational correlation time from TRA and was termed as τ_{rot}. The other three relaxation times τ_{R1} (5.4 ± 3.6 µs), τ_{R2} (56 ± 33 µs) and τ_{R3} (390 ± 194 µs) are in the µs range. Figure 4.22 shows the differences seen in this case, a prominent difference at ~500 ns and a slight difference at ~200 µs.

As seen with its ACF_{VH} (figure 4.23a), the amplitude of τ_{rot} was negatively correlated with τ_{R1}, τ_{R2} and τ_{R3} with correlation coefficients R^2 of 0.72, 0.74 and 0.52, respectively. τ_{R1} and τ_{R2} were slightly positively correlated with R^2 of 0.61. In the case of τ_{R1}, τ_{R3} and τ_{R2}, τ_{R3}, the correlation was very

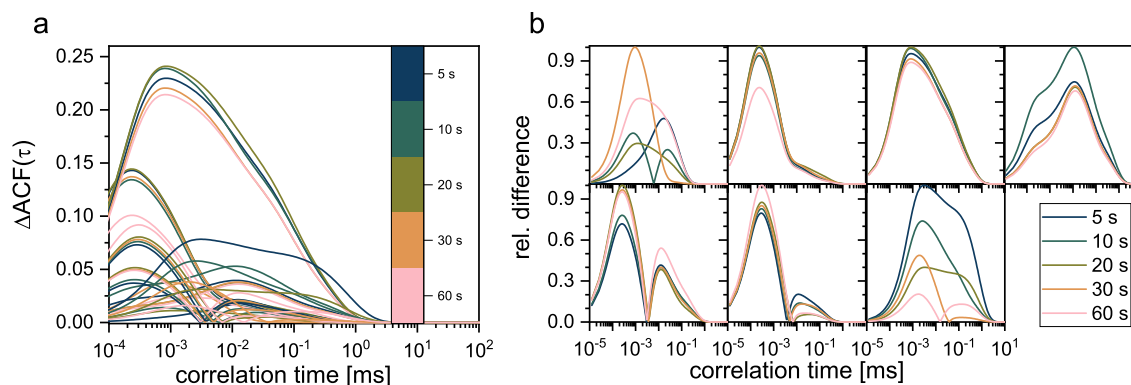**Figure 4.22:** β_2-AR^{SNAP} **is in line with** β_2-$AR^{NT\text{-}EGFP}$ **fullFCS measurements and exhibits polarisation dependent correlation amplitude difference.** Correlation amplitude difference between ACF_{VV} and ACF_{VH} for seven cell measurements with each split correlated with slice width of 5-60 s. **a**. The absolute difference in amplitude between ACF_{VV} and ACF_{VH} calculated from the fit parameter (equation (3.19)) for fullFCS measurements of β_2-AR^{SNAP}. **b**. For clarity, the absolute difference shown in **a** are plotted per measurement for slice widths from 5-60 s and were normalized such that the maximal value per sample reached 1.

less but positive with R^2 of 0.17 and 0.28 respectively. Although the trend was the same in the case of ACF_{VV} and $CCF_{VV\text{-}VH}$ (figure 4.23b,c), there was no correlation between the correlation amplitude of τ_{rot} and x_{slow} (figure 4.23d) unlike with β_2-$AR^{NT\text{-}EGFP}$. Yet, from the differences in the correlation amplitudes the data from β_2-AR^{SNAP} also hints at rotational correlation times in the µs range.

Taken together, the analysis thus hints to an additional (slow) rotational diffusion in the 1-200 µs time range which would be the missing piece needed to resolve contradictions in applying the Saffman-Delbrück model (55) to describe GPCR dynamics. The results of all rotational and relaxation times are summarised in table 4.4 and all fit results are summarized in table 4.9.

Table 4.4: Summary of rotational and relaxation times from fullFCS fit results.

Construct	τ_{rot} (ns)	τ_{R1} (µs)	τ_{R2} (µs)	τ_{R3} (µs)
β_2-$AR^{NT\text{-}EGFP}$	99 ± 52	1.9 ± 0.45	128 ± 39	-
β_2-AR^{SNAP}	194 ± 189	5.4 ± 3.6	56 ± 33	390 ± 194

4.8 Ligand stimulation of β_2-AR shows effects on diffusion constants

After the basal state dynamics was measured, effects of ligand stimulation on these dynamics were measured. This part deals with data from FCS and TRA of stimulated β_2-$AR^{NT\text{-}EGFP}$ and β_2-AR^{SNAP} using different ligands. I used three different ligands ISO, an agonist; SAL, a partial agonist and CAR, an inverse agonist [144, 179]. The process of the stimulation itself is described in Methods 3.1.5. From the measurements performed both FCS and TRA were calculated and fitted with the right models to derive diffusion/mobility parameters. Both fullFCS and ligand stimulation were done only on β_2-$AR^{NT\text{-}EGFP}$ and β_2-AR^{SNAP} as they were representative for the two classes of constructs
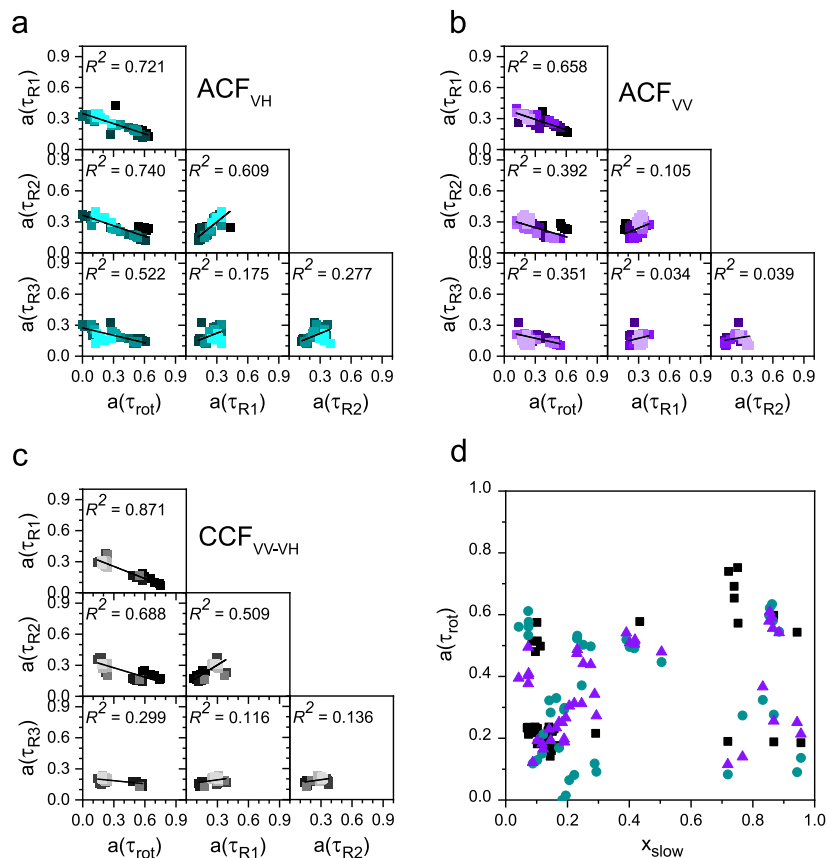
Figure 4.23: β_2-AR^{SNAP} exhibits correlation between different relaxation times. a,b,c τ_{rot}, τ_{R1} and τ_{R2} for the ACF$_{VH}$, ACF$_{VV}$ and CCF$_{VV-VH}$ respectively. Colour scheme is the same as in figure 4.21a-c, with n = 7. **d**. No clear dependency between rotational correlation amplitude $a(\tau_{rot})$ and fraction of slow membrane diffusion x_{slow} can be seen. ACF$_{VH}$ is given in turquoise circles, ACF$_{VV}$ is given in violet triangles and CCF$_{VV-VH}$ is given in black squares.

used in this work.

FCS fit results show that the ACFs still require Model 1 (equation (3.10)) to best describe them. To normalise for the variability between cells a weighted average of the diffusion coefficient was used to compare between the ligand stimulations. The main difference that can be seen (figure 4.24) is the significant decrease in diffusion constant with ISO and SAL in β_2-AR$^{NT-EGFP}$. In the case of β_2-AR^{SNAP}, the diffusion constant seems to be undisturbed by ligand stimulation which agrees with previous works by Calebiro et al. [69] and Sungkaworn et al.[45]. The summary of diffusion constants for ligand stimulation are given in table 4.5 and the summary of all FCS data for ligand stimulation are given in table 4.10.

Table 4.5: Summary of the diffusion constants from FCS fit results after ligand stimulation.

Ligand	Construct	D_{slow} (µm²/s)	D_{AVG} (µm²/s)	D_{fast} (µm²/s)	x_{fast}
ISO	β_2-AR$^{NT\text{-}EGFP}$	0.04 ± 0.02	0.04 ± 0.02	4.81 ± 2.23	0.27 ± 0.04
	β_2-AR^{SNAP}	0.09 ± 0.04	0.08 ± 0.03	18.6 ± 30.6	0.10 ± 0.08
SAL	β_2-AR$^{NT\text{-}EGFP}$	0.07 ± 0.03	0.06 ± 0.03	6.68 ± 3.28	0.26 ± 0.04
	β_2-AR^{SNAP}	0.04 ± 0.03	0.03 ± 0.02	5.95 ± 7.74	0.30 ± 0.25
CAR	β_2-AR$^{NT\text{-}EGFP}$	0.06 ± 0.05	0.05 ± 0.04	4.45 ± 2.07	0.26 ± 0.04
	β_2-AR^{SNAP}	0.07 ± 0.04	0.06 ± 0.03	14.7 ± 11.5	0.08 ± 0.04

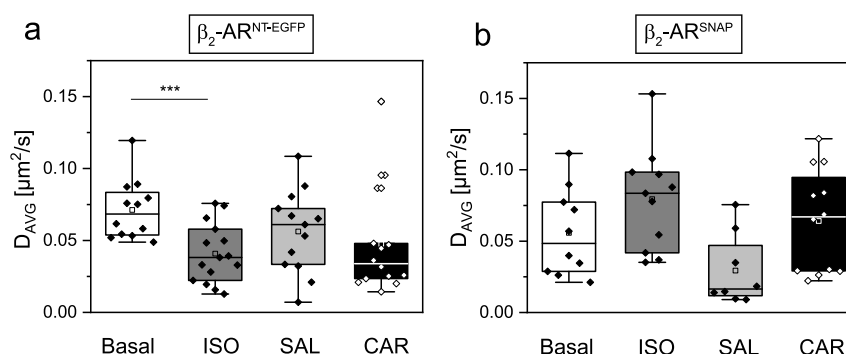**Figure 4.24: Ligand stimulation has very less influence on receptor diffusion. a**. Ligand effects on membrane diffusion of β_2-AR$^{NT\text{-}EGFP}$ expressed in CHO-K1 cells. The cells were incubated for 5 min with each of the ligands (ISO and CAR at 1 µm and SAL at 2.4 µm) prior to measurement. Average diffusion constants, D_{AVG}, weighted over the corresponding species fractions (equation (3.15)), are shown: Basal untreated state (white) 0.07 ± 0.04 µm²/s, ISO (dark grey) 0.04 ± 0.02 µm²/s, SAL (light grey) 0.06 ± 0.03 µm²/s and CAR (black) 0.05 ± 0.04 µm²/s. *** is P < 0.001. **b**. Ligand effects on membrane diffusion of β_2-AR^{SNAP} expressed in CHO-K1 cells. The incubation time and concentration of ligands were the same as β_2-AR$^{NT\text{-}EGFP}$. Average diffusion constants, D_{AVG} for the basal and ligand treated states are shown: Basal untreated state 0.05 ± 0.02 µm²/s, ISO 0.08 ± 0.03 µm²/s, SAL 0.03 ± 0.02 µm²/s and CAR 0.06 ± 0.03 µm²/s.

TRA fits show that the fluorescence decays require either a biexponential (all of β_2-AR$^{NT\text{-}EGFP}$ and most β_2-AR^{SNAP}) or a triexponential (in some cases for β_2-AR^{SNAP}) fit depending on the measurement. For the triexponential fits, both bi- and triexponential fits were performed and the final fit was chosen based on visual inspection of the residuals and χ^2-criterion (figure 4.25c). We calculated the relative χ^2 (χ^2_{rel}) ratio as χ^2_{bi}/χ^2_{tri} and defined the 2σthreshold (95% confidence level, 1700 data points, 16-18 parameters) based on an F-test, to accept the tri-exponential fit if $\chi^2_{rel} < 1.016$. The slowest rotation was considered as τ_{rot} associated with the protein. The fits shows a decrease in the rotational correlation time to a range of 20 - 100 ns for β_2-AR$^{NT\text{-}EGFP}$ for all three ligands (figure 4.25a). In the case of β_2-AR^{SNAP}, ISO stimulation decreases the distribution of the rotational correlation times to around 20 ns whereas the range was not significantly different for stimulation with partial agonist and inverse agonist (figure 4.25b). This decrease has been observed earlier by Spille et al., for α_{2A}-AR [80]. However, it has to be understood that rotational correlation times above 50 ns from the fits have a large uncertainty and cannot be taken as a significant difference. Considering this aspect, figure 4.25 shows that in the case of both constructs, rotational correlation times do not show a significant difference after ligand stimulation. This mean that the fast wobbling of proteins is largely independent of ligand

stimulated effects. The τ_{rot} and r_{ss} values from TRA fits after ligand stimulation are given in table 4.6 and all data from the fits are summarised in table 4.11.

Table 4.6: Summary of rotational correlation times from TRA fits after ligand stimulation.

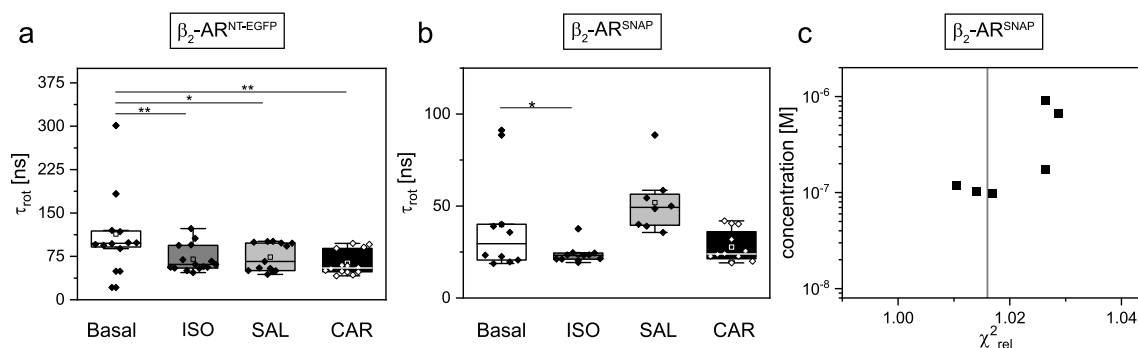| Ligand	Construct	τ_{rot} (ns)	r_{ss}
ISO	β_2-AR$^{NT\text{-}EGFP}$	70.1 ± 23.0	0.12 ± 0.02
	β_2-AR^{SNAP}	23.6 ± 4.9	0.08 ± 0.02
SAL	β_2-AR$^{NT\text{-}EGFP}$	73.7 ± 24.3	0.13 ± 0.04
	β_2-AR^{SNAP}	51.8 ± 16.8	0.09 ± 0.03
CAR	β_2-AR$^{NT\text{-}EGFP}$	63.0 ± 20.6	0.12 ± 0.02
	β_2-AR^{SNAP}	27.7 ± 8.62	0.08 ± 0.02

Figure 4.25: Rotational correlation times speed up on ligand stimulation. Rotational correlation times (slowest from the biexponential fits) calculated by fitting the photon counting histograms of live cell measurements in basal state and when treated with different ligands. Colour code is the same as in figure 4.24. **a**. β_2-AR$^{NT\text{-}EGFP}$ in its untreated basal state shows 113 ± 70 ns, with ISO shows 70 ± 23 ns, SAL shows 74 ± 24 ns and CAR shows 63 ± 21 ns. ** is P < 0.05 and * is P < 0.1. **b**. β_2-AR^{SNAP} in its untreated basal state shows 40 ± 27 ns, with ISO shows 24 ± 5 ns, SAL shows 52 ± 17 ns and CAR shows 28 ± 9 ns. * is P < 0.1. **c**. In the case of β_2-AR^{SNAP}, some cells post stimulation showed strong deviations in the weighted residuals when fitting with a biexponential rotational correlation model, thus we analysed all data also with a triexponential model, yielding a third fast rotational correlation time. To decide which model to accept as more appropriately describing the data , (i) the deviations of the weighted residuals were inspected and (ii) an F-test was performed (1700 data points, 16-18 parameters) with the null-hypothesis "The bi-exponential model describes the data significantly better than the tri-exponential fit". We employed a 2σ-criterion (95% confidence interval), which brings our threshold line to a relative χ² (χ^2_{bi}/ χ^2_{tri}) of 1.016. The values of the additional rotational correlation times are given in table 4.11.

Influence of receptor density was checked against the mobility parameters for ligand stimulation as shown in figure 4.26. Largely they seem independent, but there is an evident correlation between receptor density and rotational correlation time in the case of β_2-AR^{SNAP}, but considering the uncertainty of times above 50 ns, this behaviour can be disregarded. One other exception is the rotational correlation time of β_2-AR$^{NT\text{-}EGFP}$ (figure 4.26), that are tightly clustered for the ligand stimulation while the untreated cells show a broad distribution. In addition, the influence of receptor density on r_{ss} was probed (figure 4.27) and it does not indicate an occurrence of Homo-FRET on ligand stimulation. Both results indicate that although the basal oligomerisation state is more or less maintained, there is no indication of ligand induced receptor clustering.
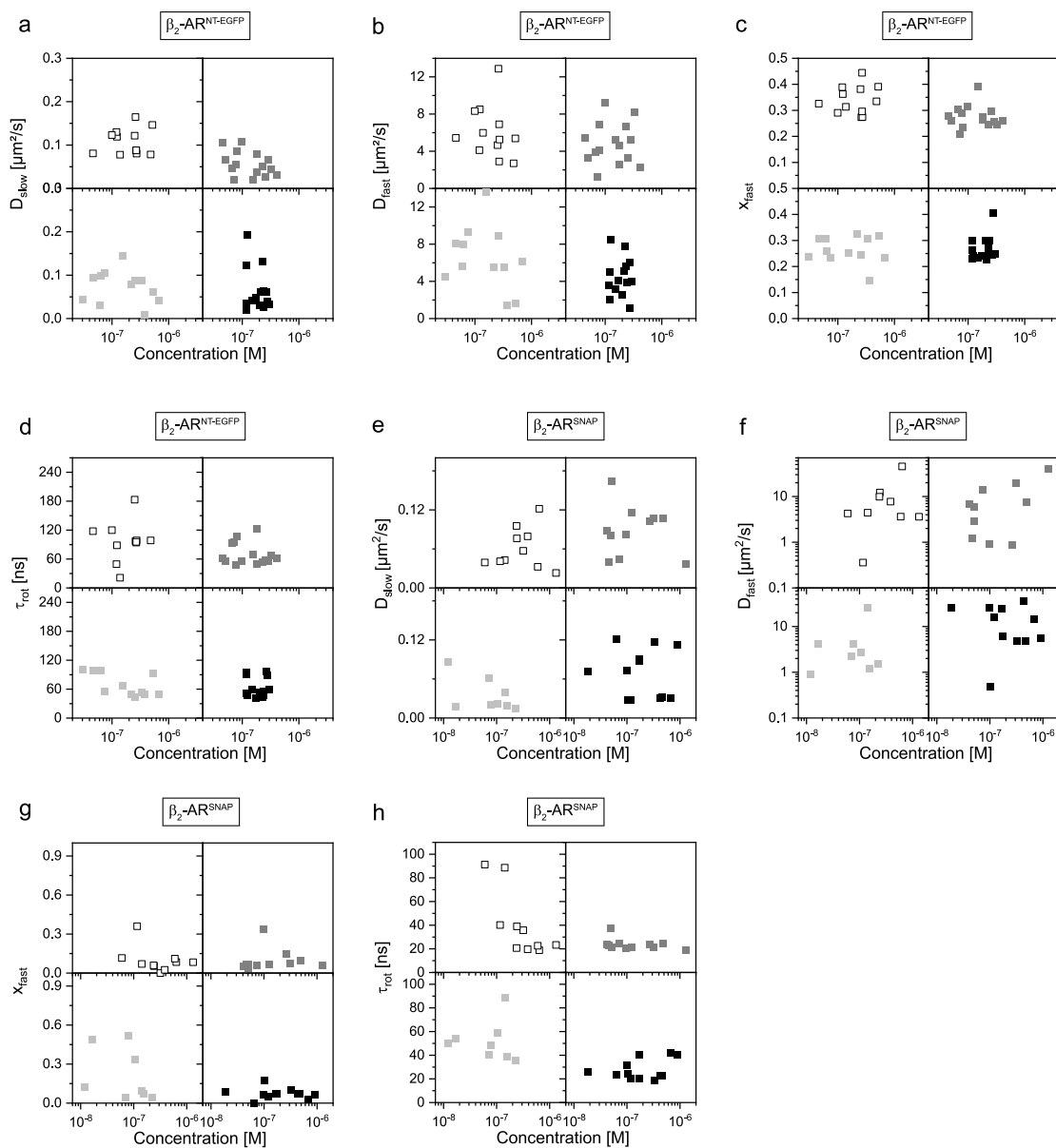
Figure 4.26: Receptor density is not influenced by ligand stimulation. The mobility measures (D_{slow}, D_{fast}, x_{fast} and τ_{rot}) of all measurements with ligand stimulation show largely no dependence on the receptor density in the measured concentration range of 50 nM – 5 µm. White boxes correspond to untreated condition, grey to cells treated with ISO, light grey to cells treated with SAL and black to cells treated with CAR. **a-d**. Mobility parameters plotted against concentration for β_2-AR$^{NT-EGFP}$. **e-h**. Mobility parameters plotted against concentration for β_2-AR^{SNAP}.
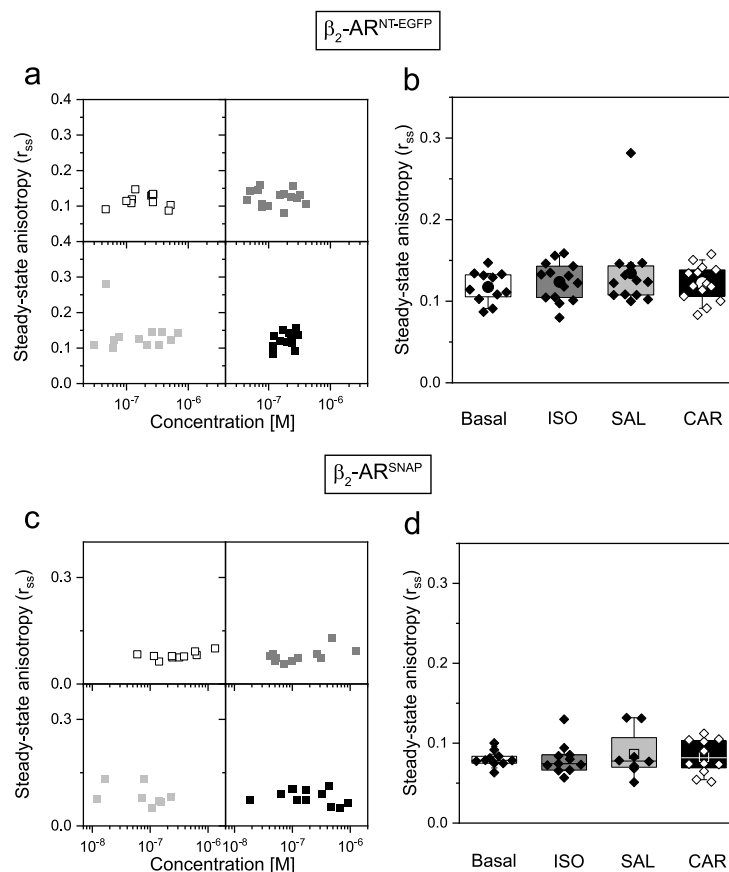
Figure 4.27: Homo-FRET is absent upon ligand stimulation of β_2-AR$^{NT-EGFP}$ and β_2-AR^{SNAP}. Steady-state anisotropy (r_{ss}) plotted against concentration shows absence of Homo-FRET in both β_2-AR$^{NT-EGFP}$ (**a**) and β_2-AR^{SNAP} (**c**). **b,d**. The distribution of r_{ss} for β_2-AR$^{NT-EGFP}$ (**b**) and β_2-AR^{SNAP} (**d**) respectively.

Table 4.7: Summary of Fluorescence Correlation Spectroscopy fit results.

Construct	N_{cells}	N	τ_{dfast} (ms)	x_{fast}	D_{fast} (μm²/s)	τ_{dslow} (ms)	D_{slow} (μm²/s)
β_2-AR$^{NT\text{-}EGFP}$	12	59.9 ± 36.9	2.71± 1.21	0.33 ± 0.05	6.08 ± 2.80	136.6 ± 35.2	0.10 ± 0.02
β_2-AR$^{IL3\text{-}EGFP}$	12	89.1 ± 115.5	2.01 ± 0.87	0.31 ± 0.04	8.09 ± 3.65	128.5 ± 59.0	0.13 ± 0.06
β_2-AR^{SNAP}	10	75.2 ± 58.7	1.88 ± 1.03	0.07 ± 0.03	11.0 ± 13.2	25.0 ± 23.9	0.06 ± 0.03
β_2-AR^{A186TCO}	6	44.7 ± 31.1	3.08 ± 0.75	0.27 ± 0.10	4.74 ± 1.36	243.7 ± 53.5	0.06 ± 0.01
α_{2A}-AR$^{NT\text{-}EGFP}$	19	77.7 ± 59.4	1.83 ± 0.89	0.34 ± 0.07	6.29 ± 3.18	172.0 ± 111.8	0.08 ± 0.08
α_{2A}-AR^{SNAP}	22	164.5 ± 101.8	0.69 ± 0.89	0.10 ± 0.05	43.3 ± 34.3	101.7 ± 55.7	0.11 ± 0.05

Table 4.8: Summary of Time-resolved Anisotropy fit results.

Construct	N_{cells}	τ_{rot} (ns)	$\tau_{rot,fast1}$ (ns)	$\tau_{rot,fast2}$ (ns)	N_{fast1}	N_{fast2}	x_{fast1}	x_{fast2}	r_{ss}
β_2-AR$^{NT\text{-}EGFP}$	12	113.7 ± 70.5	0.04 ± 0.02	-	12	0	0.81 ± 0.11-	-	0.10 ± 0.02
β_2-AR$^{IL3\text{-}EGFP}$	12	165.1 ± 14.6	0.06 ± 0.02-	-	12	0	0.69 ± 0.10-	-	0.13 ± 0.02
β_2-AR^{SNAP}	10	40.0 ± 27.5	0.06 ± 0.03	-	10	0	0.56 ± 0.07	-	0.08 ± 0.01
β_2-AR^{A186TCO}	6	118.3 ± 51.8	0.82 ± 0.55	0.09 ± 0.03	4	2	0.32 ± 0.02	0.41 ± 0.10	0.10 ± 0.01
α_{2A}-AR$^{NT\text{-}EGFP}$	19	177.0 ± 20.8	-	-	0	0	-	-	0.10 ± 0.01
α_{2A}-AR^{SNAP}	22	50.3 ± 9.2	0.27 ± 0.20	-	4	-	0.20 ± 0.19	-	0.10 ± 0.01

Table 4.9: Summary of fullFCS fit results.

Construct	Correlation	N	τ_{rot} (ns)	x_{rot}	τ_{R1} (μs)	x_{R1}	τ_{R2} (μs)	x_{R2}	τ_{R3} (μs)	x_{R3}	τ_{d2} (ms)	$1-x_{d1}$	τ_{d1} (ms)
β_2-AR$^{NT\text{-}EGFP}$	CCF$_{VH\text{-}VV}$	10.7 ± 6.9	99 ± 52	0.52 ± 0.18	1.9 ± 0.45	0.26 ± 0.08	128 ± 39	0.13 ± 0.04	-	-	2.04 ± 1.34	0.35 ± 0.08	109.3 ± 112.4
	ACF$_{VH}$			0.39 ± 0.27		0.39 ± 0.19		0.20 ± 0.11		-			
	ACF$_{VV}$			0.44 ± 0.01		0.37 ± 0.12		0.17 ± 0.06		-			
β_2-AR^{SNAP}	CCF$_{VH\text{-}VV}$	3.54 ± 3.91	194 ± 189	0.33 ± 0.19	5.4 ± 3.6	0.24 ± 0.08	56 ± 33	0.27 ± 0.07	390 ± 194	0.19 ± 0.02	1.64 ± 0.98	0.71 ± 0.30	119.0 ± 247.1
	ACF$_{VH}$			0.35 ± 0.20		0.24 ± 0.08		0.25 ± 0.08		0.20 ± 0.06			
	ACF$_{VV}$			0.35 ± 0.06		0.27 ± 0.11		0.23 ± 0.06		0.17 ± 0.06			

Table 4.10: Summary of Fluorescence Correlation Spectroscopy fit results after ligand stimulation.

Ligand	Construct	N_{cells}	N	τ_{dfast} (ms)	x_{fast}	D_{fast} (µm²/s)	τ_{dslow} (ms)	D_{slow} (µm²/s)	D_{AVG} (µm²/s)
ISO	β_2-AR$^{NT-EGFP}$	15	25.0 ± 16.9	2.98 ± 1.94	0.27 ± 0.04	4.81 ± 2.23	256.3 ± 144.8	0.04 ± 0.02	0.04 ± 0.02
	β_2-AR^{SNAP}	11	37.8 ± 53.3	11.6 ± 85.4	0.10 ± 0.08	18.6 ± 30.6	240.8 ± 211.5	0.09 ± 0.04	0.08 ± 0.03
SAL	β_2-AR$^{NT-EGFP}$	13	32.6 ± 31.5	2.53 ± 2.24	0.26 ± 0.04	6.68 ± 3.28	260.5 ± 346.4	0.07 ± 0.03	0.06 ± 0.03
	β_2-AR^{SNAP}	8	18.4 ± 15.2	4.22 ± 3.44	0.30 ± 0.25	5.95 ± 7.74	354.8 ± 212.5	0.04 ± 0.03	0.03 ± 0.02
CAR	β_2-AR$^{NT-EGFP}$	14	31.1 ± 9.19	3.32 ± 2.23	0.26 ± 0.04	4.45 ± 2.07	260.9 ± 149.6	0.06 ± 0.05	0.05 ± 0.04
	β_2-AR^{SNAP}	12	51.0 ± 47.3	3.32 ± 7.25	0.08 ± 0.04	14.7 ± 11.5	227.4 ± 140.0	0.07 ± 0.04	0.06 ± 0.03

Table 4.11: Summary of Time-resolved Anisotropy fit results after ligand stimulation.

Ligand	Construct	N_{cells}	τ_{rot} (ns)	$\tau_{rot,fast1}$ (ns)	$\tau_{rot,fast2}$ (ns)	N_{fast1}	N_{fast2}	x_{fast1}	x_{fast2}	r_{ss}
ISO	β_2-AR$^{NT-EGFP}$	15	70.1 ± 23.0	0.16 ± 0.25	-	15	0	0.24 ± 0.11	-	0.12 ± 0.02
	β_2-AR^{SNAP}	11	23.6 ± 4.9	0.09 ± 0.04	-	11	0	0.55 ± 0.12	-	0.08 ± 0.02
SAL	β_2-AR$^{NT-EGFP}$	13	73.7 ± 24.3	0.26 ± 0.11	-	13	0	0.27 ± 0.11	-	0.13 ± 0.04
	β_2-AR^{SNAP}	8	51.8 ± 16.8	0.08 ± 0.06	-	8	0	0.56 ± 0.09	-	0.09 ± 0.03
CAR	β_2-AR$^{NT-EGFP}$	14	63.0 ± 20.6	0.30 ± 0.89	-	14	0	0.25 ± 0.12	-	0.12 ± 0.02
	β_2-AR^{SNAP}	12	27.7 ± 8.62	0.82 ± 1.20	0.02 ± 0.02	10	2	0.38 ± 0.24	0.48 ± 0.12	0.08 ± 0.02

5   Discussion

Mobility of GPCRs can unlock the understanding of spatial and temporal dynamics of GPCRs in their basal and activated states. Studies have been carried out to understand GPCR translational and rotational mobility (table 1.2) but no study has spanned the whole temporal regime of nanosecond to second. There could be more hidden mobility that a GPCR possesses that has not been brought to light. This thesis aims to uncover the temporal spectrum of β_2-AR mobility, a prototypical GCPR. By employing different complementary time-resolved fluorescence techniques on live cells I am able to show that β_2-AR mobility ranges from nanosecond to second. This chapter discusses the interpretations and physiological implications of the obtained mobility results.

5.1   Dynamic nature of the basal state of β_2-AR

β_2-AR in the human body functions by binding to hormones like epinephrine (adrenaline) and norepinephrine (noradrenaline) and commencing different downstream signalling pathways which results in different physiological responses [1] within a span of seconds. This is reflected as a presence of basal mobility which would increase its chance of binding to a downstream partner. In this work, both translational and rotational mobility were pursued to understand what basal state mobility β_2-AR possesses and how they work in concert.

SPT and FCS has been used to show the basal translational mobility of β_2-AR [45, 164]. Both studies agree on the diffusion constant ranging from 0.05-0.13 µm²/s (corresponding to a diffusion time of ten to hundred ms) but FCS results show an additional component in the sub-millisecond range of 0.5-1 ms which was attributed to be fluorophore photophysics. The fast component has not been reported in the SPT study as it is a limitation of the technique itself to access dynamics above 5 µm²/s [92]. At the same time, with SPT can differentiate between different trajectories and disecting each trajectory based on diffusion coefficient and classifying them into different subpopulations as its spatial resolution is not diffraction limited [45]. With FCS, the mobility of these different subpopulations are averaged out. The FCS results in this work show a similar pattern to Parmar et al. [164], with D_{slow} similar to previous studies and an addition component, D_{fast} that unlike in the previous study, could be shown to be stemming from diffusion rather than from photophysics. By systematically testing out different possibilities the source of the D_{fast} could be localised. One possibility was the receptors in the apical membrane exhibiting faster diffusion as they are not adhered to the coverslip through extracellular matrices. It could be shown that neither being adhered to a coverslip nor having different receptor densities on both apical and basal membrane, affect translational mobility in any way (figure 4.11). The second was if the source was from inside the cell. By varying the focal volume within the cell (figure 4.12), it could

be seen that the fraction of fast component also changes, meaning the source of the fast diffusion was from inside the cell. Western blotting for cytosolic and membrane fractions showed the absence of truncated fluorophore or whole receptor in the cytosol and confirmed that all fluorescent receptors were membrane bound (figure 4.13). Another key insight supporting this hypothesis was the fraction of fast component, x_{fast} for the SNAP constructs, β_2-AR^{SNAP} and α_{2A}-AR^{SNAP} which was significantly less relative to the other constructs (4.9) since the SNAP dye used, SNAP Surface Alexa Fluor 488 is membrane impermeable. This is because only the internalised receptors would be fluorescent and not the receptors being transported to the plasma membrane after translation whereas all expressed receptors are fluorescent in the EGFP conjugated constructs. One contradiction to this point is the β_2-AR^{A186TCO} which does not show a significant difference from the EGFP conjugated constructs although labeled with an organic dye. Although confocal imaging studies have shown almost no fluorescence from within the cell [141, 180], FCS is really sensitive to sub nanomolar concentrations of a molecule added to the fact that M-Tet-ATTO 488 has not shown to be membrane impermeable through any spectroscopic studies that I have knowledge of. Taken together, it could be shown that the source of the D_{fast} is from intracellular membrane bound receptors, possibly from the movement of the membrane to which the receptor is coupled. The main culprit that could constitute to the moving intracellular membrane are vesicles, that transport membrane proteins to and from the plasma membrane. This is further supported by studies showing vesicle diffusion in cells and supported bilayers to be in the range of 2 - 40 µm²/s [177, 178] which is similar to the D_{fast} obtained here. Thus, the FCS measurements in this work shows both fluorescent receptors in the plasma membrane and those being transported to and from it.

TRA has been used to show rotational mobility of GPCRs especially α_{2A}-AR [80] and serotonin$_{1A}$ receptor [61]. The results in this work show the rotational mobility of β_2-AR and α_{2A}-AR ranging between 20-300 ns (figure 4.15) which is in line with the previous studies [61, 80]. These results have one drastic effect, they solidify the notion that adrenergic receptors do not fit the Saffman-Delbrück model [57] (Theory 2.3), an approximation for diffusion of membrane bound proteins. The Saffman-Delbrück approximation predicts the ratio of the lateral to rotational diffusion constant for a given transmembrane protein undergoing Brownian diffusion in a non-crowded environment (equation (2.36)). It predicts rotational correlation time in the µs range for adrenergic receptors. TRA in itself is limited to resolving rotational correlation times of up to 50 ns in this work. This limitation is due to the fluorescence lifetime of the fluorophores [98] used in this work, ranging from 2.9 ns for EGFP to 4.1 ns for AF488 and ATTO 488. Hence, the fullFCS approach was used to overcome this hurdle and quantify mobility in the µs range. Establishing it for measuring membrane protein dynamics in live cells based on correlating spliced intensity traces [129] proved to be key in overcoming the problem of resolving µs diffusion dynamics. fullFCS results hints at a rotational correlation time in the 1-200 µs range. Additional rotational correlation time seen in the case of β_2-AR^{SNAP} can be attributed to the rotational freedom of the bound dye, also seen in the case of TRA fits. This presence of µs rotational correlation time as seen in fullFCS results would imply that β_2-AR can be described by the Saffman-Delbrück approximation. While previous studies have shown ns rotational correlation time using TRA [61, 80] and discussed that the Saffman-Delbrück approximation does not fit for certain GPCRs, this in fact, should have been attributed to the limitation of TRA, which is limited in the time range it can probe due to the choice of fluorophores used. This reasoning explains why methods like fullFCS

albeit its need for a high photon budget, should be pursued if diffusion dynamics in the µs range are in question. To emphasise more on the prediction of the µs correlation time, it has to be noted that the Saffman-Delbrück model is only an approximation of the whole diffusion on a cell's plasma membrane scenario. Nevertheless, based on the mean D_{slow} obtained for β_2-AR, the Saffman-Delbrück model predicts a rotational correlation time of 160 µs, which is within the range of fullFCS results.

5.2 Influence of activation on β_2-AR mobility

Basal state dynamics gives only one part of the picture and to understand mobility of a GPCR in whole its activation needs to be studied. I treated β_2-AR$^{NT-EGFP}$ and β_2-AR^{SNAP} with different ligands. An agonist, Isoproterenol (ISO) capable of starting the activation cascade for β_2-AR; a partial agonist, Salbutamol (SAL) which creates only a part activation and an inverse agonist, Carazolol (CAR) which represses β_2-AR activity when bound.

In this study, ISO treatment shows a decrease in D_{slow} (0.10 µm²/s mean for untreated state to 0.04 µm²/s mean for ligand stimulated state) for β_2-AR$^{NT-EGFP}$ and no change for β_2-AR^{SNAP} while SAL and CAR do not show a change in D_{slow} in both β_2-AR$^{NT-EGFP}$ and β_2-AR^{SNAP}. The results for agonist activation of β_2-AR^{SNAP} calculated here has been seen before through single particle tracking as shown by Sungkaworn et al. [45], and through fluorescence recovery after photobleaching as shown by Dorsch et al. [60]. Diffusion constant data for β_2-AR$^{NT-EGFP}$ agonist activation has not been reported before to my knowledge. An explanation could be in the way the constructs work inherently. Membrane proteins in general are transported to and from the plasma membrane [1]. In the case of β_2-AR$^{NT-EGFP}$ almost all of the overexpressed β_2-AR are fluorescent whereas for β_2-AR^{SNAP}, after the cell has been labelled, during the course of 2-3 hr for a measurement, the amount of fluorescent receptors in the plasma membrane decreases and internalised fluorescent receptors lead to the small fraction of D_{fast} visible from FCS measurements both in basal and activated states. This means that during the measurement, β_2-AR^{SNAP} has fewer plasma membrane bound receptors relative to β_2-AR$^{NT-EGFP}$. During activation, this would be reflected as more fluorescent receptors getting activated in β_2-AR$^{NT-EGFP}$ than in β_2-AR^{SNAP}. Activation in GPCRs has been attributed to an increase in internalisation [181] initiated by the formation of clathrin coated pits [182]. The formation of these clathrin coated pits could be the cause of the decrease in the distribution of the diffusion constants in β_2-AR$^{NT-EGFP}$ upon agonist activation. β_2-AR^{SNAP} on the other hand does not show any effect upon agonist activation due to the presence of less fluorescent receptors.

In terms of rotational mobility, ligand treatment in general seems to decrease the rotational correlation times (becomes faster) in the case of β_2-AR$^{NT-EGFP}$ and only for ISO activation in the case of β_2-AR^{SNAP}. This speeding up of rotational correlation time upon ligand stimulation has been reported before by both Spille et al. [80] and Paila et al. [61]. However, as mentioned before, since EGFP, AF488 and ATTO 488 have their average fluorescence lifetimes in the range of 2.9 - 4.1 ns, for a pulsed excitation their fluorescence intensity completely decays by 30 - 50 ns [98, 99]. Hence, rotational correlation times > 50 ns cannot be determined with confidence. Since the distribution of the rotational correlation times is 114 ± 71 ns for the untreated β_2-AR$^{NT-EGFP}$ which

decreases to 70 ± 23 ns for ligand stimulation (figure 4.25), the difference in distribution should not be taken as significant. Another point is the multiexponential decay needed for the fits. This could either be arising from the freedom of movement of the substrate bound dye molecule or from the presence of Homo-FRET [61, 117, 183] (Theory 2.2.3). Presence of Homo-FRET could be visualised both by a shorter decay component and a decrease in the r_{ss} with increase in concentration of fluorescent receptors [117, 183]. Although, figure 4.27a,c shows no such decrease, it can be seen that the r_{ss} values in general are low (figure 4.27b,d). As previously implied in Results 4.6, this low spread of r_{ss} hints at the presence of a basal oligomerisation state. Extending on this, ligand stimulation also shows no change in this oligomerisation state.

5.3   Influence of fluorescent tags on β_2-AR mobility

Three different tagging strategies have been pursued in this study, a fluorescent protein (β_2-AR$^{NT-EGFP}$ and β_2-AR$^{IL3-EGFP}$), a SNAP tag bound to AF488 (β_2-AR^{SNAP}) and a genetic code expansion approach with point mutations expressing an unnatural amino acid which is later bound to ATTO 488 (β_2-AR^{A186TCO}). All three show consistent translational diffusion behaviour, only the fraction of the diffusion components were different in the case of β_2-AR^{SNAP}. This is because AF488 used to label β_2-AR^{SNAP} is membrane impermeable. Hence tags capable of incorporating membrane impermeable organic dyes serve as a lens to focus only on membrane dynamics and not vesicular transport and other intracellular diffusion. In terms of rotational diffusion, the tagging strategy proved crucial. For fluorescent proteins whose size (EGFP 30 kDa) is nearly half of a GPCR (β_2-AR 60 kDa), it is hard to decouple rotational motion of the fluorophore from the protein. β_2-AR$^{IL3-EGFP}$ aimed to address this problem by restricting the freedom of movement for EGFP, although care should be taken in designing such a construct as it could lead to impairment of the receptor function. Whereas, in the case of β_2-AR^{SNAP} and β_2-AR^{A186TCO} the rotational movement of the bound dye could be clearly decoupled from the receptor rotation, as seen from the additional rotational correlation times needed for fitting. In this work, it has been possible to show that using small organic dyes are favourable for time-resolved spectroscopy measurements. In addition, they also give the flexibility to experiment with different dyes with varying photochemistry and spectral range.

5.4   Conclusion

The thesis shows that the diffusion dynamics of β_2-AR is spread over a time range of nanosecond to second. It pinpoints the source of the ms fast diffusion calculated from FCS fits as arising from intracellular membrane bound sources, most probably vesicular transport and not from photophysics as considered before [164]. fullFCS served as the tool to close the blindspot between TRA and FCS measurements and they show the presence of the so far elusive µs rotational correlation time. This serves as proof that the Saffman-Delbrück approximation also fits in the case of β_2-AR just like Rhodopsin [57]. Finally, ligand stimulation does not seem to induce receptor clustering. Although, there may be a basal oligomerisation state which stays the same

upon activation. This study demonstrates that capturing mobility parameters in a wide range is absolutely important to one day access GPCR dynamics as a whole, all the way from basal state to when it gets activated and how its downstream signals are orchestrated biophysically.

6   Outlook

This study was able to show diffusion dynamics of β_2-AR in live cells exists over a wide time range and sophisticated spectroscopic techniques are necessary to measure time constants over a range of nanosecond to second. fullFCS in particular, although is a powerful technique to access dynamics in the range of ps-s, needs a high photon budget. This becomes a hurdle when measuring in live cells. A split correlation approach was taken in this work to overcome artefacts from aggregates and photobleaching during these long measurements. There are multiple approaches that could be taken to understand different perspective of GPCR dynamics. One way is to establish fullFCS measurements of GPCRs in model membranes or nanodiscs, in order to overcome the shortcomings of live cells such as the measurement time, aggregate formation and photobleaching that could be controlled to a greater extent. Although, the process of membrane protein purification and reconstitution is hard, it has been reported [184–186] and it gives us more control over the system, flexibility over dye chemistry and lets us view dynamics of membrane proteins and its downstream neighbours, one component at a time. This might prove complementary for live cell studies in the future. Another way is to extend the time range of TRA is by using fluorophores with very long lifetimes that could decay over µs. This would let us observe any rotational motions in the ns-µs range without the drawbacks of fullFCS in live cells. One other aspect is the improvements over the last couple of years in analysis of intensity fluctuation data by implementation of Bayesian non-parametrics [187, 188] for standard FCS data. Such improvements in analysis could prove useful for live cell measurements by decreasing the time of measurement significantly and getting more temporal information out of lesser photon statistics.

The major limitations of all techniques used in this thesis is their compromise on spatial scale and resolution for gaining high temporal resolution. The optimum method for measuring GPCR dynamics would be the one which makes a good compromise between spatial scale and spatial and temporal resolution. Various approaches in literature have take this route to gain access to specific information in tandem. These techniques have either been shown or could be extended to the membrane dynamics scenario of a live cell. One study reported that FLIM can be coupled with TRA imaging to obtain information about rotational mobility in addition to intra- and intermolecular conformational dynamics by accessing FRET [189]. Techniques like Phasor S-FLIM has taken this a level further by accessing a wider fluorescence spectrum in not only cells but also spheroids [190]. By combining stimulated emission depletion (STED) microscopy with FCS [136], it has been possible to not just gain spatial resolution but also varying effective confocal volumes made possible by tuning the intensity of the doughnut-shaped depletion beam. This has been extensively applied to study membrane dynamics [5, 6, 72, 191]. A recent study of imaging FCS implemented through a total internal reflection fluorescence (TIRF) [192] modality combines computational super-resolution techniques like super-resolution optical fluctuation imaging (SOFI) [193] and super-resolution radial fluctuations (SRRF) [194] to achieve high spatial localisation

(~60 nm) and resolution (~100 nm) with minimal artefacts [195]. Although their temporal resolution was ~2 ms, it was only limited by the acquisition time of the camera that was used in the study. By additionally implementing number and brightness analysis [196] they were also able to probe the oligomerisation states of the system they were studying [195]. A recent study coupling FCS on a confocal laser scanning microscope with a single-photon array detector has been shown to make a good compromise between the spatial and temporal information gained [197]. This is due to the array detector working like an AiryScan detector [198] combined with its ability to temporally tag photons with picosecond precision. Taken together, there is no one perfect technique for understanding GPCR or membrane dynamics as a whole. Instead, different techniques and methodologies have to be combined to get closer to the ground truth scenario.

Another path that must be explored from the receptor biology context is the concept of biased signalling where different ligands are shown to activate varied downstream signalling pathways. This has been attributed to biased signalling based on the activating ligand [199]. Recently the molecular mechanism of biased signalling using molecular dynamic simulations [200] and conformational changes using single-molecule fluorescence spectroscopy [201] has been reported but mobility changes accompanying such signalling are yet to be addressed. Techniques like FRET-FCCS [202–205] (a technique that can probe dynamic FRET and mobility simultaneously) can reveal how a conformational change works in parallel with a certain mobility change for a given ligand on a given receptor. This study only takes into account the diffusion dynamics arising from the fluorescent receptor itself. It does not delve into intermolecular interactions and how they influence diffusional and conformational dynamics. Such studies approached through different techniques are a necessity to know how different parties interact to orchestrate GPCR activation and signalling.

References

[1] D. L. Nelson and M. M. Cox. *Lehninger principles of biochemistry*. Ed. by K. Ahr. 5th. New York : W.H. Freeman, 2008., 2008, pp. 371–384, 423–432.

[2] S. Heyden and M. Ortiz. 'Investigation of the influence of viscoelasticity on oncotripsy'. In: *Computer Methods in Applied Mechanics and Engineering* 314 (Feb. 2017), pp. 314–322.

[3] E. Sezgin et al. 'The mystery of membrane organization: Composition, regulation and roles of lipid rafts'. In: *Nature Reviews Molecular Cell Biology* 18.6 (June 2017), pp. 361–374.

[4] K. Jacobson, P. Liu and B. C. Lagerholm. 'The Lateral Organization and Mobility of Plasma Membrane Components'. In: *Cell* 177.4 (May 2019), pp. 806–819.

[5] F. Schneider et al. 'Diffusion of lipids and GPI-anchored proteins in actin-free plasma membrane vesicles measured by STED-FCS'. In: *Molecular Biology of the Cell* 28.11 (June 2017). Ed. by R. G. Parton, pp. 1507–1518.

[6] K. Pinkwart et al. 'Nanoscale dynamics of cholesterol in the cell membrane'. In: *Journal of Biological Chemistry* 294.34 (July 2019), pp. 12599–12609.

[7] K. L. Pierce, R. T. Premont and R. J. Lefkowitz. 'Seven-transmembrane receptors'. In: *Nature Reviews Molecular Cell Biology* 3.9 (Sept. 2002), pp. 639–650.

[8] R. J. Lefkowitz. 'A brief history of G-protein coupled receptors (Nobel Lecture)'. In: *Angewandte Chemie - International Edition* 52.25 (June 2013), pp. 6366–6378.

[9] J. E. Dowling. *Nobel prize: Three named for medicine, physiology award*. Oct. 1967.

[10] E. W. Sutherland. 'Studies on the mechanism of hormone action'. In: *Science* 177.4047 (Aug. 1972), pp. 401–408.

[11] T. N. Raju. *The Nobel chronicles. 1994: Alfred G Gilman (b 1941) and Martin Rodbell (1925-98).* June 2000.

[12] R. Axel. 'Scents and sensibility: A molecular logic of olfactory perception (Nobel Lecture)'. In: *Angewandte Chemie - International Edition*. Vol. 44. 38. Wiley-VCH Verlag, Sept. 2005, pp. 6110–6127.

[13] L. B. Buck. 'Unraveling the sense of smell (Nobel Lecture)'. In: *Angewandte Chemie - International Edition*. Vol. 44. 38. John Wiley & Sons, Ltd, Sept. 2005, pp. 6128–6140.

[14] M. Rask-Andersen, M. S. Almén and H. B. Schiöth. 'Trends in the exploitation of novel drug targets'. In: *Nature Reviews Drug Discovery* 10.8 (Aug. 2011), pp. 579–590.

[15] L. F. Kolakowski. 'GCRDb: A G-protein-coupled receptor database'. In: *Receptors and Channels* 2.1 (Jan. 1994), pp. 1–7.

[16] R. Fredriksson et al. 'The G-protein-coupled receptors in the human genome form five main families. Phylogenetic analysis, paralogon groups, and fingerprints'. In: *Molecular Pharmacology* 63.6 (June 2003), pp. 1256–1272.

[17] K. J. Nordström et al. 'Independent HHsearch, Needleman-Wunsch-based, and motif analyses reveal the overall hierarchy for most of the g protein-coupled receptor families'. In: *Molecular Biology and Evolution* 28.9 (Sept. 2011), pp. 2471–2480.

[18] X. Qu, D. Wang and B. Wu. 'Progress in GPCR structure determination'. In: *GPCRs: Structure, Function, and Drug Discovery*. Elsevier, Jan. 2019, pp. 3–22.

[19] C. Munk et al. 'GPCRdb: the G protein-coupled receptor database – an introduction'. In: *British Journal of Pharmacology* 173.14 (2016), pp. 2195–2207.

[20] A. J. Kooistra et al. 'GPCRdb in 2021: Integrating GPCR sequence, structure and function'. In: *Nucleic Acids Research* 49.D1 (Jan. 2021), pp. D335–D343.

[21] V. Cherezov et al. 'High-resolution crystal structure of an engineered human β2-adrenergic G protein-coupled receptor'. In: *Science* 318.5854 (Nov. 2007), pp. 1258–1265.

[22] T. D. Goddard et al. 'UCSF ChimeraX: Meeting modern challenges in visualization and analysis'. In: *Protein Science* 27.1 (Jan. 2018), pp. 14–25.

[23] A. G. Gilman. 'G proteins: transducers of receptor-generated signals.' In: *Annual review of biochemistry* 56 (Nov. 1987), pp. 615–649.

[24] J. M. Baldwin. 'Structure and function of receptors coupled to G proteins'. In: *Current Opinion in Cell Biology* 6.2 (Apr. 1994), pp. 180–190.

[25] W. I. Weis and B. K. Kobilka. 'The Molecular Basis of G Protein-Coupled Receptor Activation'. In: *Annual Review of Biochemistry* 87 (June 2018), pp. 897–919.

[26] F. J. Ehlert. 'Quantifying gpcr allostery and biased signaling'. In: *GPCRs: Structure, Function, and Drug Discovery*. Elsevier, Jan. 2019, pp. 143–169.

[27] M. J. Lohse et al. 'β-arrestin: A protein that regulates β-adrenergic receptor function'. In: *Science* 248.4962 (June 1990), pp. 1547–1550.

[28] S. M. DeWire et al. 'β-Arrestins and cell signaling'. In: *Annual Review of Physiology* 69 (Feb. 2007), pp. 483–510.

[29] K. Zheng et al. 'Arrestin-mediated signaling at GPCRs'. In: *GPCRs: Structure, Function, and Drug Discovery*. Elsevier, Jan. 2019, pp. 243–255.

[30] V. V. Gurevich and E. V. Gurevich. 'Biased GPCR signaling: Possible mechanisms and inherent limitations'. In: *Pharmacology and Therapeutics* 211 (July 2020), p. 107540.

[31] A. Manglik et al. 'Structural Insights into the Dynamic Process of β2-Adrenergic Receptor Signaling.' In: *Cell* 161.5 (May 2015), pp. 1101–11.

[32] K. Palczewski et al. 'Crystal Structure of Rhodopsin: A G Protein-Coupled Receptor'. In: *Science* 289.5480 (Aug. 2000), pp. 739–745.

[33] S. G. Rasmussen et al. 'Crystal structure of the human β2 adrenergic G-protein-coupled receptor'. In: *Nature* 450.7168 (Nov. 2007), pp. 383–387.

[34] S. G. Rasmussen et al. 'Structure of a nanobody-stabilized active state of the β2 adrenoceptor'. In: *Nature* 469.7329 (Jan. 2011), pp. 175–181.

[35] S. G. F. S. Rasmussen et al. 'Crystal structure of the β2 adrenergic receptor-Gs protein complex.' In: *Nature* 477.7366 (July 2011), pp. 549–55.

[36] D. M. Rosenbaum et al. 'GPCR engineering yields high-resolution structural insights into β2-adrenergic receptor function'. In: *Science* 318.5854 (Nov. 2007), pp. 1266–1273.

[37] R. O. Dror et al. 'Activation mechanism of the β 2-adrenergic receptor'. In: *Proceedings of the National Academy of Sciences of the United States of America* 108.46 (Nov. 2011), pp. 18684–18689.

[38] X. Deupi and J. Standfuss. 'Structural insights into agonist-induced activation of G-protein-coupled receptors'. In: *Current Opinion in Structural Biology* 21.4 (Aug. 2011), pp. 541–551.

[39] W. Huang et al. 'Structural insights into μ-opioid receptor activation'. In: *Nature* 524.7565 (Aug. 2015), pp. 315–321.

[40] A. Koehl et al. 'Structural insights into the activation of metabotropic glutamate receptors'. In: *Nature* 566.7742 (Feb. 2019), pp. 79–84.

[41] D. Hilger et al. 'Structural insights into differences in G protein activation by family A and family B GPCRs'. In: *Science* 369.6503 (July 2020).

[42] T. Ikuta et al. 'Structural insights into the mechanism of rhodopsin phosphodiesterase'. In: *Nature Communications* 11.1 (Dec. 2020), pp. 1–12.

[43] Y. Zhuang et al. 'Structural insights into the human D1 and D2 dopamine receptor signaling complexes'. In: *Cell* 184.4 (Feb. 2021), 931–942.e18.

[44] R. Nygaard et al. 'The dynamic process of β2-adrenergic receptor activation'. In: *Cell* 152.3 (Jan. 2013), pp. 532–542.

[45] T. Sungkaworn et al. 'Single-molecule imaging reveals receptor-G protein interactions at cell surface hot spots'. In: *Nature* 550.7677 (Oct. 2017), pp. 543–547.

[46] B. K. Kobilka. 'Structural insights into adrenergic receptor function and pharmacology'. In: *Trends in Pharmacological Sciences* 32.4 (Apr. 2011), pp. 213–218.

[47] F. J. Alenghat and D. E. Golan. 'Membrane protein dynamics and functional implications in mammalian cells'. In: *Current Topics in Membranes*. Vol. 72. Academic Press Inc., Jan. 2013, pp. 89–120.

[48] J. Orly and M. Schramm. 'Coupling of catecholamine receptor from one cell with adenylate cyclase from another cell by cell fusion'. In: *Proceedings of the National Academy of Sciences of the United States of America* 73.12 (Dec. 1976), pp. 4410–4414.

[49] A. M. Tolkovsky and A. Levitzki. 'Mode of Coupling between the β- Adrenergic Receptor and Adenylate Cyclase in Turkey Erythrocytes'. In: *Biochemistry* 17.18 (1978), pp. 3795–3810.

[50] A. De Lean, J. M. Stadel and R. J. Lefkowitz. 'A ternary complex model explains the agonist-specific binding properties of the adenylate cyclase-coupled β-adrenergic receptor'. In: *Journal of Biological Chemistry* 255.15 (Aug. 1980), pp. 7108–7117.

[51] P. Samama et al. 'A mutation-induced activated state of the β2-adrenergic receptor. Extending the ternary complex model'. In: *Journal of Biological Chemistry* 268.7 (Mar. 1993), pp. 4625–4636.

[52] J. M. Weiss et al. 'The cubic ternary complex receptor-occupancy model I. Model description'. In: *Journal of Theoretical Biology* 178.2 (Jan. 1996), pp. 151–167.

[53] M. Javanainen et al. 'Diffusion of Integral Membrane Proteins in Protein-Rich Membranes'. In: *Journal of Physical Chemistry Letters* 8.17 (Sept. 2017), pp. 4308–4313.

[54]   M. Javanainen, O. H. Ollila and H. Martinez-Seara. 'Rotational Diffusion of Membrane Proteins in Crowded Membranes'. In: *Journal of Physical Chemistry B* 124.15 (Apr. 2020), pp. 2994–3001.

[55]   R. A. Cone. 'Rotational Diffusion of Rhodopsin in the Visual Receptor Membrane'. In: *Nature New Biology* 236.63 (Mar. 1972), pp. 39–43.

[56]   M.-m. Poo and R. A. Cone. 'Lateral diffusion of rhodopsin in the photoreceptor membrane'. In: *Nature* 247.5441 (Feb. 1974), pp. 438–441.

[57]   P. G. Saffman and M. Delbrück. 'Brownian motion in biological membranes.' In: *Proceedings of the National Academy of Sciences of the United States of America* 72.8 (1975), pp. 3111–3.

[58]   D. Magde, E. Elson and W. W. Webb. 'Thermodynamic Fluctuations in a Reacting System—Measurement by Fluorescence Correlation Spectroscopy'. In: *Physical Review Letters* 29.11 (1972), pp. 705–708.

[59]   D. Axelrod et al. 'Mobility measurement by analysis of fluorescence photobleaching recovery kinetics'. In: *Biophysical Journal* 16.9 (1976), pp. 1055–1069.

[60]   S. Dorsch et al. 'Analysis of receptor oligomerization by FRAP microscopy'. In: *Nature Methods* 6.3 (Feb. 2009), pp. 225–230.

[61]   Y. D. Paila et al. 'Oligomerization of the serotonin1A receptor in live cells: A time-resolved fluorescence anisotropy approach'. In: *Journal of Physical Chemistry B* 115.39 (Oct. 2011), pp. 11439–11447.

[62]   B. Aguila, M. Simaan and S. A. Laporte. 'Study of G protein-coupled receptor/β-arrestin interactions within endosomes using FRAP'. In: *Methods in Molecular Biology* 756 (2011), pp. 371–380.

[63]   H. Guo et al. 'Methods used to study the oligomeric structure of G-protein-coupled receptors'. In: *Bioscience Reports* 37.2 (Apr. 2017).

[64]   M. J. Lohse. 'Dimerization in GPCR mobility and signaling'. In: *Current Opinion in Pharmacology* 10.1 (Feb. 2010), pp. 53–58.

[65]   A. Kusumi, Y. Sako and M. Yamamoto. 'Confined lateral diffusion of membrane receptors as studied by single particle tracking (nanovid microscopy). Effects of calcium-induced differentiation in cultured epithelial cells'. In: *Biophysical Journal* 65.5 (Nov. 1993), pp. 2021–2040.

[66]   K. Ritchie et al. 'The fence and picket structure of the plasma membrane of live cells as revealed by single molecule techniques (Review)'. In: *Molecular Membrane Biology* 20.1 (2003), pp. 13–18.

[67]   K. Suzuki et al. 'Rapid Hop Diffusion of a G-Protein-Coupled Receptor in the Plasma Membrane as Revealed by Single-Molecule Techniques'. In: *Biophysical Journal* 88.5 (May 2005), pp. 3659–3680.

[68]   T. K. Fujiwara et al. 'Confined diffusion of transmembrane proteins and lipids induced by the same actin meshwork lining the plasma membrane'. In: *Molecular Biology of the Cell* 27.7 (Apr. 2016). Ed. by P. Bassereau, pp. 1101–1119.

[69] D. Calebiro et al. 'Single-molecule analysis of fluorescently labeled G-protein-coupled receptors reveals complexes with distinct dynamics and organization.' In: *Proceedings of the National Academy of Sciences of the United States of America* 110.2 (Jan. 2013), pp. 743–8.

[70] D. Calebiro et al. 'G protein-coupled receptor-G protein interactions: a single-molecule perspective'. In: *Physiological Reviews* 101.3 (July 2021), pp. 857–906.

[71] C. Eggeling et al. 'Direct observation of the nanoscale dynamics of membrane lipids in a living cell'. In: *Nature* 457.7233 (Feb. 2009), pp. 1159–1162.

[72] A. Honigmann et al. 'Scanning STED-FcS reveals spatiotemporal heterogeneity of lipid interaction in the plasma membrane of living cells'. In: *Nature Communications* 5.1 (Nov. 2014), pp. 1–12.

[73] S. J. Briddon et al. 'Quantitative analysis of the formation and diffusion of A 1-adenosine receptor-antagonist complexes in single living cells'. In: *Proceedings of the National Academy of Sciences of the United States of America* 101.13 (Mar. 2004), pp. 4673–4678.

[74] S. J. Briddon et al. 'Plasma membrane diffusion of g protein-coupled receptor oligomers'. In: *Biochimica et Biophysica Acta - Molecular Cell Research* 1783.12 (Dec. 2008), pp. 2262–2268.

[75] R. Corriden et al. 'Kinetic analysis of antagonist-occupied adenosine-A3 receptors within membrane microdomains of individual cells provides evidence of receptor dimerization and allosterism'. In: *FASEB Journal* 28.10 (Oct. 2014), pp. 4211–4222.

[76] R. H. Rose, S. J. Briddon and S. J. Hill. 'A novel fluorescent histamine H 1 receptor antagonist demonstrates the advantage of using fluorescence correlation spectroscopy to study the binding of lipophilic ligands'. In: *British Journal of Pharmacology* 165.6 (Mar. 2012), pp. 1789–1800.

[77] L. E. Kilpatrick, S. J. Briddon and N. D. Holliday. 'Fluorescence correlation spectroscopy, combined with bimolecular fluorescence complementation, reveals the effects of β-arrestin complexes and endocytic targeting on the membrane mobility of neuropeptide Y receptors'. In: *Biochimica et Biophysica Acta - Molecular Cell Research* 1823.6 (June 2012), pp. 1068–1081.

[78] F. Philip, P. Sengupta and S. Scarlata. 'Signaling through a G protein-coupled receptor and its corresponding G protein follows a stoichiometrically limited model'. In: *Journal of Biological Chemistry* 282.26 (June 2007), pp. 19203–19216.

[79] K. Herrick-Davis et al. 'Fluorescence Correlation Spectroscopy Analysis of Serotonin, Adrenergic, Muscarinic, and Dopamine Receptor Dimerization: The Oligomer Number Puzzle'. In: *Molecular Pharmacology* 84.4 (Oct. 2013), pp. 630–642.

[80] J.-H. Spille et al. 'Rotational Diffusion of the α2a Adrenergic Receptor Revealed by FlAsH Labeling in Living Cells'. In: *Biophysical Journal* 100.4 (Feb. 2011), pp. 1139–1148.

[81] C. D. Valentine and P. M. Haggie. 'Confinement of β 1- and β 2-adrenergic receptors in the plasma membrane of cardiomyocyte-like H9c2 cells is mediated by selective interactions with PDZ domain and A-kinase anchoring proteins but not caveolae'. In: *Molecular Biology of the Cell* 22.16 (Aug. 2011), pp. 2970–2982.

[82] O. Hegener et al. 'Dynamics of β2-adrenergic receptor-ligand complexes on living cells'. In: *Biochemistry* 43.20 (May 2004), pp. 6190–6199.

[83] T. J. Pucadyil and A. Chattopadhyay. 'Cholesterol depletion induces dynamic confinement of the G-protein coupled serotonin1A receptor in the plasma membrane of living cells'. In: *Biochimica et Biophysica Acta - Biomembranes* 1768.3 (Mar. 2007), pp. 655–668.

[84] K. Herrick-Davis et al. 'Oligomer size of the serotonin 5-hydroxytryptamine 2C (5-HT2C) receptor revealed by fluorescence correlation spectroscopy with photon counting histogram analysis: Evidence for homodimers without monomers or tetramers'. In: *Journal of Biological Chemistry* 287.28 (July 2012), pp. 23604–23614.

[85] A. Sergé et al. 'Receptor Activation and Homer Differentially Control the Lateral Mobility of Metabotropic Glutamate Receptor 5 in the Neuronal Membrane'. In: *Journal of Neuroscience* 22.10 (May 2002), pp. 3910–3920.

[86] A. N. Saulière-Nzeh et al. 'Agonist-selective dynamic compartmentalization of human mu opioid receptor as revealed by resolutive FRAP analysis'. In: *Journal of Biological Chemistry* 285.19 (May 2010), pp. 14514–14520.

[87] S. Schrottke et al. 'Expression, Functional Characterization, and Solid-State NMR Investigation of the G Protein-Coupled GHS Receptor in Bilayer Membranes'. In: *Scientific Reports* 7.1 (Apr. 2017), pp. 1–11.

[88] Z. Petrásek and P. Schwille. 'Precise measurement of diffusion coefficients using scanning fluorescence correlation spectroscopy.' In: *Biophysical journal* 94.4 (Feb. 2008), pp. 1437–48.

[89] S. Felekyan et al. 'Filtered FCS: Species Auto- and Cross-Correlation Functions Highlight Binding and Dynamics in Biomolecules'. In: *ChemPhysChem* 13.4 (Mar. 2012), pp. 1036–1053.

[90] M. Oura et al. 'Polarization-dependent fluorescence correlation spectroscopy for studying structural properties of proteins in living cell'. In: *Scientific Reports* 6.1 (2016).

[91] T. Dertinger et al. 'Two-focus fluorescence correlation spectroscopy: A new tool for accurate and absolute diffusion measurements'. In: *ChemPhysChem* 8.3 (Feb. 2007), pp. 433–443.

[92] I. Koyama-Honda et al. 'High-speed single-molecule imaging reveals signal transduction by induced transbilayer raft phases'. In: *Journal of Cell Biology* 219.12 (Oct. 2020).

[93] T. Wohland et al. 'Single Plane Illumination Fluorescence Correlation Spectroscopy (SPIM-FCS) probes inhomogeneous three-dimensional environments'. In: *Optics Express* 18.10 (May 2010), p. 10627.

[94] N. O. Petersen et al. 'Quantitation of membrane receptor distributions by image correlation spectroscopy: concept and application'. In: *Biophysical Journal* 65.3 (Sept. 1993), pp. 1135–1146.

[95] M. A. Digman et al. 'Measuring fast dynamics in solutions and cells with a laser scanning microscope'. In: *Biophysical Journal* 89.2 (Aug. 2005), pp. 1317–1327.

[96] J. Wagner et al. 'Single-Molecule Fluorescence Microscopy for the Analysis of Fast Receptor Dynamics'. In: *G Protein-Coupled Receptors in Drug Discovery. Methods in Molecular Biology*. Ed. by M. Filizola. Vol. 1335. Humana Press, New York, NY, 2015. Chap. 5, pp. 53–66.

[97] J. R. Lakowicz. *Principles of fluorescence spectroscopy*. Ed. by J. R. Lakowicz. Boston, MA: Springer US, 2006, pp. 1–954.

[98] W. Becker. 'Advanced time-correlated single photon counting techniques'. In: *Springer Series in Chemical Physics*. Ed. by A. W. Castleman, J. Toennies and W. Zinth. Springer Series in Chemical Physics. Berlin, Heidelberg: Springer Berlin Heidelberg, 2005. Chap. 3, pp. 27–46.

[99] J. R. Lakowicz. 'Time-Domain Lifetime Measurements'. In: *Principles of Fluorescence Spectroscopy*. Springer US, 2006. Chap. 4, pp. 97–155.

[100] F. Perrin. 'Polarisation de la lumière de fluorescence. Vie moyenne des molécules dans l'etat excité'. In: *Journal de Physique et le Radium* 7.12 (Dec. 1926), pp. 390–401.

[101] J. R. Lakowicz. 'Fluorescence Anisotropy'. In: *Principles of Fluorescence Spectroscopy*. Springer US, 2006. Chap. 10, pp. 353–382.

[102] J. Myšková et al. 'Directionality of light absorption and emission in representative fluorescent proteins'. In: *Proceedings of the National Academy of Sciences of the United States of America* 117.51 (Dec. 2020), pp. 32395–32401.

[103] J. R. Lakowicz. 'Time-Dependent Anisotropy Decays'. In: *Principles of Fluorescence Spectroscopy*. Boston, MA: Springer US, 2006. Chap. 11, pp. 383–412.

[104] S. Sindbert et al. 'Accurate distance determination of nucleic acids via förster resonance energy transfer: Implications of dye Linker length and rigidity'. In: *Journal of the American Chemical Society* 133.8 (Mar. 2011), pp. 2463–2480.

[105] K. Hemmen. 'Structure and conformational fluctuations of Phage T4 Lysozyme under native and denaturing conditions'. PhD thesis. 2016, p. 17.

[106] T. Förster. 'Zwischenmolekulare Energiewanderung und Fluoreszenz'. In: *Annalen der Physik* 437.1-2 (Jan. 1948), pp. 55–75.

[107] T. Eilert et al. 'Complete Kinetic Theory of FRET'. In: *Journal of Physical Chemistry B* 122.49 (Dec. 2018), pp. 11677–11694.

[108] J. R. Lakowicz. 'Energy Transfer'. In: *Principles of Fluorescence Spectroscopy*. Springer US, 2006, pp. 443–475.

[109] T. J. Lambert. 'FPbase: a community-editable fluorescent protein database'. In: *Nature Methods* 16.4 (Apr. 2019), pp. 277–278.

[110] F. S. Wouters and P. I. Bastiaens. 'Fluorescence lifetime imaging of receptor tyrosine kinase activity in cells'. In: *Current Biology* 9.19 (Oct. 1999), pp. 1127–1130.

[111] W. Becker. 'Fluorescence lifetime imaging - techniques and applications'. In: *Journal of Microscopy* 247.2 (Aug. 2012), pp. 119–136.

[112] F. S. Wouters and P. I. Bastiaens. 'Imaging Protein□Protein Interactions by Fluorescence Resonance Energy Transfer (FRET) Microscopy'. In: *Current Protocols in Cell Biology* 7.1 (July 2000), pp. 17.1.1–17.1.15.

[113] E. B. Van Munster et al. 'Fluorescence resonance energy transfer (FRET) measurement by gradual acceptor photobleaching'. In: *Journal of Microscopy* 218.3 (June 2005), pp. 253–262.

[114] T. Zimmermann et al. 'Spectral imaging and linear un-mixing enables improved FRET efficiency with a novel GFP2-YFP FRET pair'. In: *FEBS Letters* 531.2 (Nov. 2002), pp. 245–249.

[115] N. E. Snell et al. 'Homotransfer FRET reporters for live cell imaging'. In: *Biosensors* 8.4 (Oct. 2018).

[116] G. Weber. 'Dependence of the polarization of the fluorescence on the concentration'. In: *Transactions of the Faraday Society* 50.0 (Jan. 1954), pp. 552–555.

[117] E. K. Yeow and A. H. Clayton. 'Enumeration of oligomerization states of membrane proteins in living cells by homo-FRET spectroscopy and microscopy: Theory and application'. In: *Biophysical Journal* 92.9 (May 2007), pp. 3098–3104.

[118] N. Ojha, K. H. Rainey and G. H. Patterson. 'Imaging of fluorescence anisotropy during photoswitching provides a simple readout for protein self-association'. In: *Nature Communications* 11.1 (Dec. 2020), pp. 1–11.

[119] P. Schwille and E. Haustein. 'Fluorescence correlation spectroscopy. An introduction to its concepts and applications'. In: *Spectroscopy* 94(22) (2001), pp. 1–33.

[120] J. R. Lakowicz. 'Fluorescence correlation spectroscopy'. In: *Principles of Fluorescence Spectroscopy*. Boston, MA: Springer US, 2006. Chap. 24, pp. 797–840.

[121] R. Rigler et al. 'Fluorescence correlation spectroscopy with high count rate and low background: analysis of translational diffusion'. In: *European Biophysics Journal* 22.3 (Aug. 1993), pp. 169–175.

[122] P. Schwille, J. Korlach and W. W. Webb. 'Fluorescence correlation spectroscopy with single-molecule sensitivity on cell and model membranes.' In: *Cytometry* 36.3 (1999), pp. 176–182.

[123] K. Bacia et al. 'Fluorescence correlation spectroscopy relates rafts in model and native membranes'. In: *Biophysical Journal* 87.2 (Aug. 2004), pp. 1034–1043.

[124] S. A. Kim, K. G. Heinze and P. Schwille. 'Fluorescence correlation spectroscopy in living cells'. In: *Nature Methods* 4.11 (Nov. 2007), pp. 963–973.

[125] C. Eggeling et al. 'Data registration and selective single-molecule analysis using multi-parameter fluorescence detection'. In: *Journal of Biotechnology* 86.3 (Apr. 2001), pp. 163–180.

[126] M. Böhmer et al. 'Time-resolved confocal scanning device for ultrasensitive fluorescence detection'. In: *Review of Scientific Instruments* 72.11 (Nov. 2001), p. 4145.

[127] M. Wahl et al. 'Fast calculation of fluorescence correlation data with asynchronous time-correlated single-photon counting'. In: *Optics Express* 11.26 (Dec. 2003), p. 3583.

[128] D. C. Lamb et al. 'Sensitivity enhancement in fluorescence correlation spectroscopy of multiple species using time-gated detection'. In: *Biophysical Journal* 79.2 (Aug. 2000), pp. 1129–1138.

[129] J. Ries et al. 'Automated suppression of sample-related artifacts in Fluorescence Correlation Spectroscopy'. In: *Optics Express* 18.11 (May 2010), p. 11073.

[130] S. Felekyan et al. 'Full correlation from picoseconds to seconds by time-resolved and time-correlated Single photon detection'. In: *Review of Scientific Instruments* 76.8 (Aug. 2005), pp. 1–14.

[131]   A. Loman et al. 'Measuring rotational diffusion of macromolecules by fluorescence correlation spectroscopy'. In: *Photochem. Photobiol. Sci.* 9.5 (May 2010), pp. 627–636.

[132]   C. M. Pieper and J. Enderlein. 'Fluorescence correlation spectroscopy as a tool for measuring the rotational diffusion of macromolecules'. In: *Chemical Physics Letters* 516.1-3 (Nov. 2011), pp. 1–11.

[133]   A. Ghosh et al. 'Quantifying Microsecond Transition Times Using Fluorescence Lifetime Correlation Spectroscopy'. In: *Journal of Physical Chemistry Letters* 8.24 (2017), pp. 6022–6028.

[134]   E. P. Petrov and P. Schwille. 'State of the Art and Novel Trends in Fluorescence Correlation Spectroscopy'. In: *Standardization and Quality Assurance in Fluorescence Measurements II*. Vol. 6. Springer Berlin Heidelberg, Mar. 2008, pp. 145–197.

[135]   K. Hassler et al. 'Total internal reflection fluorescence correlation spectroscopy (TIR-FCS) with low background and high count-rate per molecule'. In: *Optics Express* 13.19 (Sept. 2005), p. 7415.

[136]   L. Kastrup et al. 'Fluorescence fluctuation spectroscopy in subdiffraction focal volumes'. In: *Physical Review Letters* 94.17 (May 2005), p. 178104.

[137]   P. Schwille et al. 'Molecular Dynamics in Living Cells Observed by Fluorescence Correlation Spectroscopy with One- and Two-Photon Excitation'. In: *Biophysical Journal* 77.4 (Oct. 1999), pp. 2251–2265.

[138]   K. G. Heinze, A. Koltermann and P. Schwille. 'Simultaneous two-photon excitation of distinct labels for dual-color fluorescence crosscorrelation analysis.' In: *Proceedings of the National Academy of Sciences of the United States of America* 97.19 (Sept. 2000), pp. 10377–82.

[139]   B. D. Hughes, B. A. Pailthorpe and L. R. White. 'The Translational And Rotational Drag On A Cylinder Moving In A Membrane'. In: *Journal of Fluid Mechanics* 110 (1981), pp. 349–372.

[140]   I. Nikić et al. 'Labeling proteins on live mammalian cells using click chemistry'. In: *Nature Protocols* 10.5 (Apr. 2015), pp. 780–791.

[141]   G. Beliu et al. 'Bioorthogonal labeling with tetrazine-dyes for super-resolution microscopy'. In: *Communications Biology* 2.1 (Dec. 2019).

[142]   L. S. Barak et al. 'Internal trafficking and surface mobility of a functionally intact beta2-adrenergic receptor-green fluorescent protein conjugate.' In: *Molecular pharmacology* 51.2 (Feb. 1997), pp. 177–84.

[143]   A. Sieben et al. 'α-Hederin, but Not Hederacoside C and Hederagenin from Hedera helix , Affects the Binding Behavior, Dynamics, and Regulation of β 2 -Adrenergic Receptors'. In: *Biochemistry* 48.15 (Apr. 2009), pp. 3477–3482.

[144]   C. K. Billington, R. B. Penn and I. P. Hall. 'β2 Agonists'. In: *Handbook of Experimental Pharmacology*. Vol. 237. Springer New York LLC, 2016, pp. 23–40.

[145]   M. Tramier et al. 'Restrained torsional dynamics of nuclear DNA in living proliferative mammalian cells'. In: *Biophysical Journal* 78.5 (May 2000), pp. 2614–2627.

[146]   S. T. Hess and W. W. Webb. 'Focal volume optics and experimental artifacts in confocal fluorescence correlation spectroscopy'. In: *Biophysical Journal* 83.4 (Oct. 2002), pp. 2300–2317.

[147] M. Koshioka, K. Sasaki and H. Masuhara. 'Time-Dependent Fluorescence Depolarization Analysis in Three-Dimensional Microspectroscopy'. In: *Applied Spectroscopy* 49.2 (Feb. 1995), pp. 224–228.

[148] G. F. Schröder, U. Alexiev and H. Grubmüller. 'Simulation of Fluorescence Anisotropy Experiments: Probing Protein Dynamics'. In: *Biophysical Journal* 89.6 (2005), pp. 3757–3770.

[149] K. Bahlmann and S. W. Hell. 'Electric field depolarization in high aperture focusing with emphasis on annular apertures'. In: *Journal of Microscopy* 200.1 (Oct. 2000), pp. 59–67.

[150] K. Bahlmann and S. W. Hell. 'Depolarization by high aperture focusing'. In: *Applied Physics Letters* 77.5 (July 2000), pp. 612–614.

[151] A. Z. Politi et al. 'Quantitative mapping of fluorescently tagged cellular proteins using FCS-calibrated four-dimensional imaging'. In: *Nature Protocols* 13.6 (June 2018), pp. 1445–1464.

[152] R. T. Youker and H. Teng. 'Measuring protein dynamics in live cells: protocols and practical considerations for fluorescence fluctuation microscopy'. In: *Journal of Biomedical Optics* 19.9 (Sept. 2014), p. 090801.

[153] E. Kravets et al. 'Guanylate binding proteins directly attack Toxoplasma gondii via supramolecular complexes'. In: *eLife* 5 (Jan. 2016).

[154] F. Hillger et al. 'Probing protein-chaperone interactions with single-molecule fluorescence spectroscopy'. In: *Angewandte Chemie - International Edition* 47.33 (Aug. 2008), pp. 6184–6188.

[155] M. Cristóvão et al. 'Single-molecule multiparameter fluorescence spectroscopy reveals directional MutS binding to mismatched bases in DNA'. In: *Nucleic Acids Research* 40.12 (July 2012), pp. 5448–5464.

[156] T. O. Peulen, O. Opanasyuk and C. A. Seidel. 'Combining Graphical and Analytical Methods with Molecular Simulations to Analyze Time-Resolved FRET Measurements of Labeled Macromolecules Accurately'. In: *Journal of Physical Chemistry B* 121.35 (Sept. 2017), pp. 8211–8241.

[157] A. Ortega, D. Amorós and J. García De La Torre. 'Prediction of hydrodynamic and other solution properties of rigid proteins from atomic- and residue-level models'. In: *Biophysical Journal* 101.4 (Aug. 2011), pp. 892–898.

[158] A. Balakrishnan et al. 'Unraveling the hidden temporal range of fast beta2-adrenergic receptor mobility by time-resolved fluorescence'. In: *Under revision* ().

[159] N. Hino et al. 'Site-specific incorporation of non-natural amino acids into proteins in mammalian cells with an expanded genetic code'. In: *Nature Protocols* 1.6 (Jan. 2007), pp. 2957–2962.

[160] S. J. Hill, C. Williams and L. T. May. 'Insights into GPCR pharmacology from the measurement of changes in intracellular cyclic AMP; advantages and pitfalls of differing methodologies'. In: *British Journal of Pharmacology* 161.6 (Nov. 2010), pp. 1266–1275.

[161] J. Schindelin et al. 'Fiji: An open-source platform for biological-image analysis'. In: *Nature Methods* 9.7 (July 2012), pp. 676–682.

[162] E. M. Manders et al. 'Dynamics of three-dimensional replication patterns during the S-phase, analysed by double labelling of DNA and confocal microscopy'. In: *Journal of Cell Science* 103.3 (Nov. 1992), pp. 857–862.

[163] E. M. MANDERS, F. J. VERBEEK and J. A. ATEN. 'Measurement of co☐localization of objects in dual☐colour confocal images'. In: *Journal of Microscopy* 169.3 (Mar. 1993), pp. 375–382.

[164] V. K. Parmar et al. 'Beta2-adrenergic receptor homodimers: Role of transmembrane domain 1 and helix 8 in dimerization and cell surface expression'. In: *Biochimica et Biophysica Acta - Biomembranes* 1859.9 (Sept. 2017), pp. 1445–1455.

[165] G. Vámosi et al. 'EGFP oligomers as natural fluorescence and hydrodynamic standards'. In: *Scientific Reports* 6 (Sept. 2016).

[166] Z. Zhang, D. Yomo and C. Gradinaru. 'Choosing the right fluorophore for single-molecule fluorescence studies in a lipid environment'. In: *Biochimica et Biophysica Acta - Biomembranes* 1859.7 (July 2017), pp. 1242–1253.

[167] H. Hevekerl et al. 'Förster resonance energy transfer beyond 10 nm: Exploiting the triplet state kinetics of organic fluorophores'. In: *Journal of Physical Chemistry B* 115.45 (Nov. 2011), pp. 13360–13370.

[168] K. Luby-Phelps et al. 'A novel fluorescence ratiometric method confirms the low solvent viscosity of the cytoplasm'. In: *Biophysical Journal* 65.1 (July 1993), pp. 236–242.

[169] K. Fushimi and A. S. Verkman. 'Low viscosity in the aqueous domain of cell cytoplasm measured by picosecond polarization microfluorimetry'. In: *Journal of Cell Biology* 112.4 (Feb. 1991), pp. 719–725.

[170] K. Kwapiszewska et al. 'Nanoscale Viscosity of Cytoplasm Is Conserved in Human Cell Lines'. In: *Journal of Physical Chemistry Letters* 11.16 (Aug. 2020), pp. 6914–6920.

[171] E. Moeendarbary et al. 'The cytoplasm of living cells behaves as a poroelastic material'. In: *Nature Materials* 12.3 (Mar. 2013), pp. 253–261.

[172] Q. Wang et al. 'Structural Basis for Calcium Sensing by GCaMP2'. In: *Structure* 16.12 (Dec. 2008), pp. 1817–1827.

[173] B. Mollwitz et al. 'Directed evolution of the suicide protein O 6-alkylguanine-DNA alkyltransferase for increased reactivity results in an alkylated protein with exceptional stability'. In: *Biochemistry* 51.5 (Feb. 2012), pp. 986–994.

[174] A. Royant and M. Noirclerc-Savoye. 'Stabilizing role of glutamic acid 222 in the structure of Enhanced Green Fluorescent Protein'. In: *Journal of Structural Biology* 174.2 (May 2011), pp. 385–390.

[175] F. Wäldchen et al. 'Whole-cell imaging of plasma membrane receptors by 3D lattice light-sheet dSTORM'. In: *Nature Communications* 11.1 (Dec. 2020), pp. 1–6.

[176] K. Wieland et al. 'Involvement of Asn-293 in stereospecific agonist recognition and in activation of the β2-adrenergic receptor'. In: *Proceedings of the National Academy of Sciences of the United States of America* 93.17 (Aug. 1996), pp. 9276–9281.

[177] M. Kyoung and E. D. Sheets. 'Vesicle diffusion close to a membrane: intermembrane interactions measured with fluorescence correlation spectroscopy.' In: *Biophysical journal* 95.12 (Dec. 2008), pp. 5789–97.

[178] I. Verdeny-Vilanova et al. '3D motion of vesicles along microtubules helps them to circumvent obstacles in cells'. In: *Journal of Cell Science* 130.11 (June 2017), pp. 1904–1916.

[179] H. C. Chan, S. Filipek and S. Yuan. 'The Principles of Ligand Specificity on beta-2-adrenergic receptor'. In: *Scientific Reports* 6.1 (Oct. 2016), pp. 1–11.

[180] G. Beliu and M. Sauer. 'A Trojan Horse for live-cell super-resolution microscopy'. In: *Light: Science and Applications* 9.1 (Dec. 2020).

[181] H. Kim et al. 'Spatiotemporal Characterization of GPCR Activity and Function during Endosomal Trafficking Pathway'. In: *Analytical Chemistry* (Jan. 2021).

[182] E. Shumay et al. 'Trafficking of $\beta2$-adrenergic receptors: Insulin and β-agonists regulate internalization by distinct cytoskeletal pathways'. In: *Journal of Cell Science* 117.4 (Feb. 2004), pp. 593–600.

[183] A. N. Bader et al. 'Homo-FRET imaging as a tool to quantify protein and lipid clustering'. In: *ChemPhysChem* 12.3 (Feb. 2011), pp. 475–483.

[184] E. Serebryany, G. A. Zhu and E. C. Yan. 'Artificial membrane-like environments for in vitro studies of purified G-protein coupled receptors'. In: *Biochimica et Biophysica Acta - Biomembranes* 1818.2 (Feb. 2012), pp. 225–233.

[185] T. Gao et al. 'Characterization of De Novo Synthesized GPCRs Supported in Nanolipoprotein Discs'. In: *PLoS ONE* 7.9 (Sept. 2012), p. 44911.

[186] P. Calmet et al. 'Real time monitoring of membrane GPCR reconstitution by plasmon waveguide resonance: On the role of lipids'. In: *Scientific Reports* 6.1 (Nov. 2016), pp. 1–12.

[187] S. Jazani et al. 'An alternative framework for fluorescence correlation spectroscopy'. In: *Nature Communications* 10.1 (Dec. 2019), p. 3662.

[188] M. Tavakoli et al. 'Pitching Single-Focus Confocal Data Analysis One Photon at a Time with Bayesian Nonparametrics'. In: *Physical Review X* 10.1 (Mar. 2020), p. 011021.

[189] K. Suhling et al. 'Probing the local environment of green fluorescent protein (GFP) with fluorescence lifetime imaging (FLIM) and time-resolved fluorescence anisotropy imaging (tr-FAIM)'. In: *Biomedical Topical Meeting (2002), paper WD1*. The Optical Society, Feb. 2020, WD1.

[190] L. Scipioni et al. 'Phasor S-FLIM: a new paradigm for fast and robust spectral fluorescence lifetime imaging'. In: *Nature Methods* 18.5 (May 2021), pp. 542–550.

[191] E. Sezgin et al. 'Measuring nanoscale diffusion dynamics in cellular membranes with super-resolution STED–FCS'. In: *Nature Protocols* 14.4 (Apr. 2019), pp. 1054–1083.

[192] D. Axelrod, N. L. Thompson and T. P. Burghardt. 'Total internal reflection fluorescent microscopy'. In: *Journal of Microscopy* 129.1 (1983), pp. 19–28.

[193] T. Dertinger et al. 'Fast, background-free, 3D super-resolution optical fluctuation imaging (SOFI)'. In: *Proceedings of the National Academy of Sciences of the United States of America* 106.52 (Dec. 2009), pp. 22287–22292.

[194] N. Gustafsson et al. 'Fast live-cell conventional fluorophore nanoscopy with ImageJ through super-resolution radial fluctuations'. In: *Nature Communications* 7.1 (Aug. 2016), pp. 1–9.

[195]   J. Sankaran et al. 'Simultaneous spatiotemporal super-resolution and multi-parametric fluorescence microscopy'. In: *Nature Communications* 12.1 (Dec. 2021).

[196]   M. A. Digman et al. 'Mapping the number of molecules and brightness in the laser scanning microscope'. In: *Biophysical Journal* 94.6 (Mar. 2008), pp. 2320–2332.

[197]   E. Slenders et al. 'Confocal-based fluorescence fluctuation spectroscopy with a SPAD array detector'. In: *Light: Science and Applications* 10.1 (Dec. 2021), pp. 2047–7538.

[198]   J. Huff. 'The Airyscan detector from ZEISS: confocal imaging with improved signal-to-noise ratio and super-resolution'. In: *Nature Methods* 12.12 (Dec. 2015), pp. i–ii.

[199]   M. Seyedabadi, M. H. Ghahremani and P. R. Albert. 'Biased signaling of G protein coupled receptors (GPCRs): Molecular determinants of GPCR/transducer selectivity and therapeutic potential'. In: *Pharmacology and Therapeutics* 200 (Aug. 2019), pp. 148–178.

[200]   C. M. Suomivuori et al. 'Molecular mechanism of biased signaling in a prototypical G protein-coupled receptor'. In: *Science* 367.6480 (Feb. 2020), pp. 881–887.

[201]   R. Lamichhane et al. 'Biased Signaling of the G-Protein-Coupled Receptor β2AR Is Governed by Conformational Exchange Kinetics'. In: *Structure* 28.3 (Jan. 2020), 371–377.e3.

[202]   J. Widengren et al. 'Two new concepts to measure fluorescence resonance energy transfer via fluorescence correlation spectroscopy: Theory and experimental realizations'. In: *Journal of Physical Chemistry A* 105.28 (July 2001), pp. 6851–6866.

[203]   H. Sahoo and P. Schwille. 'FRET and FCS - Friends or foes?' In: *ChemPhysChem* 12.3 (Feb. 2011), pp. 532–541.

[204]   M. Baibakov and J. Wenger. 'Laser-induced fluorescence quenching of red fluorescent dyes with green excitation: Avoiding artifacts in PIE-FRET and FCCS analysis'. In: *Chemical Physics Letters* 706 (Aug. 2018), pp. 669–674.

[205]   P. Li et al. 'Quantifying intramolecular protein conformational dynamics under lipid interaction using smFRET and FCCS'. In: *Methods in Molecular Biology*. Vol. 1860. Humana Press Inc., 2019, pp. 345–359.

Appendix

Materials

Cell lines

Table 6.1: Cell lines used in this work.

Cell line	Source
CHO-K1	ATCC CCL-61
HEK293T	ATCC CRL-3216

Plasmids

In this thesis, β_2-AR and α_{2A}-AR constructs were used. Dr. Ulrike Zabel from AG Lohse provided me six contructs:

1. β_2-AR conjugated to EGFP in the N-terminal (β_2-AR$^{NT\text{-}EGFP}$)
2. β_2-AR conjugated to EGFP in the intracellular loop-3 (β_2-AR$^{IL3\text{-}EGFP}$)
3. β_2-AR conjugated to SNAP tag in the N-terminal (β_2-AR^{SNAP})
4. α_{2A}-AR conjugated to EGFP in the N-terminal (α_{2A}-AR$^{NT\text{-}EGFP}$)
5. α_{2A}-AR conjugated to SNAP tag in the N-terminal (α_{2A}-AR^{SNAP})

Dr. Gerti Beliu from AG Sauer provided me with two constructs:

1. β_2-AR conjugated to EGFP in the intracellular loop-3 incorporating an unnatural amino acid at A186TCO (β_2-AR$^{A186TCO\text{-}IL3\text{-}EGFP}$)
2. β_2-AR incorporating an unnatural amino acid at A186TCO (β_2-AR^{A186TCO})

Dr. Gerti Beliu also provided me with the plasmid for the expression of tRNA/tRNA-synthetase pair, pCMV tRNA^{Pyl}/NESPylRS^{AF}, which was kindly provided to AG Sauer by Prof. Edward Lemke [140, 141].

All plasmids were constructed based on a pcDNA3 vector backbone with the receptor inserted in between the enzyme cleavage sites of HindIII and XhoI (Figure 6.1) except for α_{2A}-AR^{SNAP}, in which case the cleavage sites are HindIII and BamHI. All constructs were tested for their functionality using cAMP assay kit (Abcam) (refer Methods 3.1.6).
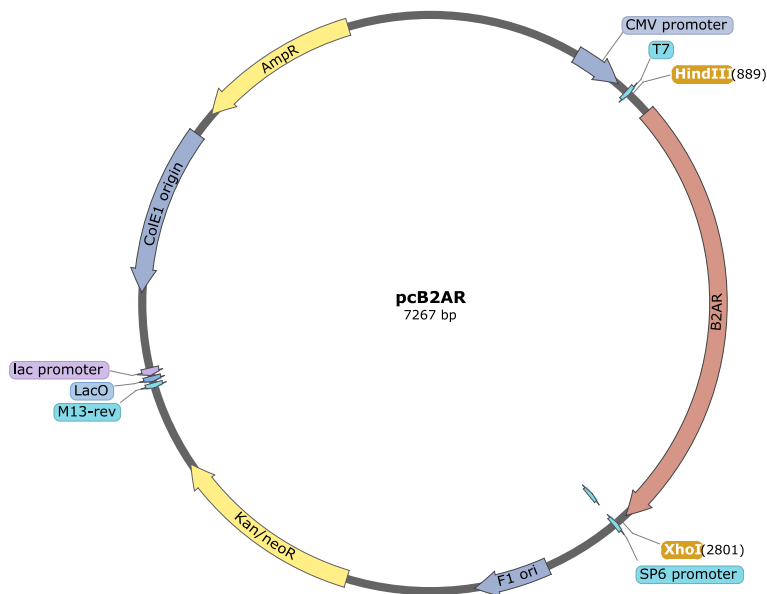
Figure 6.1: Plasmid map of β_2-AR^{WT}. Annotated plasmid map of β_2-AR^{WT} in a pcDNA3 vector backbone.

Table 6.2: Plasmids used in the work.

Vector	Construct name	Insert	Restriction site
pcDNA3	β_2-AR^{WT}	β_2-AR	HindIII and XhoI
pcDNA3	β_2-AR$^{NT-EGFP}$	EGFP-β_2-AR	HindIII and XhoI
pcDNA3	β_2-AR$^{CT-EGFP}$	β_2-AR-EGFP	HindIII and XhoI
pcDNA3	β_2-AR$^{IL3-EGFP}$	FLAG-β_2-AR-EGFP-IL3	HindIII and XhoI
pcDNA3	β_2-AR^{SNAP}	FLAG-SNAP-β_2-AR	HindIII and XhoI
pcDNA3	α_{2A}-AR$^{NT-EGFP}$	FLAG-EGFP-α_{2A}-AR	HindIII and XhoI
pcDNA3	β_2-AR^{SNAP}	FLAG-SNAP-α_{2A}-AR	HindIII and BamHI
pcDNA3	β_2-AR$^{A186TCO-IL3-EGFP}$	FLAG-A186TCO-β_2-AR-EGFP-IL3	HindIII and XhoI
pcDNA3	β_2-AR^{A186TCO}	FLAG-A186TCO-β_2-AR	HindIII and XhoI

Reagents and Materials for cell culture and western blotting

Table 6.3: Reagents and Materials for cell culture.

Reagent/Materials	Manufacturer
DMEM/F12 medium	PAN Biotech, Aidenbach, Germany/ Thermo Fischer Scientific, Dreieich, Germany
DMEM medium	Life Technologies, Darmstadt, Germany/ Thermo Fischer Scientific, Dreieich, Germany
Fetal Calf Serum	Biochrom, Berlin, Germany
Penicillin and Streptomycin	Thermo Fischer Scientific, Dreieich, Germany
L-Glutamine	PAN Biotech, Aidenbach, Germany
100x17 mm Dish, Nunclon Delta	Thermo Fischer Scientific, Dreieich, Germany
dPBS	Life Technologies, Darmstadt, Germany
Trypsin-EDTA	Sigma-Aldrich, Steinheim, Germany
Poly-D-Lysine	Sigma-Aldrich, Steinheim, Germany
HEPES	Life Technologies, Darmstadt, Germany
Lipofectamine 2000	Life Technologies, Darmstadt, Germany
jetPRIME	Polyplus-transfection SA, Illkirch, France
Sonoplus HD200 Ultrasonic bath	Bandelin electronic, Berlin, Germany
Sonorex Super Ultrasonic bath	Bandelin electronic, Berlin, Germany
TCO*lysine	SiChem, Bremen, Germany
TRIS	AppliChem GmbH, Darmstadt, Germany
EDTA	AppliChem GmbH, Darmstadt, Germany
Benzamidine	AppliChem GmbH, Darmstadt, Germany
Beckmann Optima TLX Ultracentrifuge	Beckmann Coulter, Krefeld, Germany
Nitrocellulose membrane	Sartorius AG, Göttingen, Germany
Sodium Chloride	AppliChem GmbH, Darmstadt, Germany
Recombinant Anti-GFP antibody, ab32146	Abcam, Cambridge, UK
Anti-beta 2 Adrenergic Receptor antibody, ab61778	Abcam, Cambridge, UK
Goat Anti-Rabbit IgG H&L (HRP), ab205718	Abcam, Cambridge, UK
Pierce ECL Western Blotting Substrate	Thermo Fischer Scientific, Dreieich, Germany
Vilber Fusion FX	Vilber Lourmat, Collégien, France

Labelling reagents

Table 6.4: Organic fluorophores used in this work.

Label	Source
SNAP-Surface Alexa Fluor 488	New England Biolabs, Massachusetts, USA
6-Methyl-Tetrazine-ATTO-488	Jena Bioscience, Jena, Germany

Chemicals

Table 6.5: Chemicals used for coverslip cleaning.

Chemical	Producer
NaOH	Roth, Karlsruhe, Germany
Chloroform	PanReac AppliChem, Darmstadt, Germany
Absolute ethanol	Merck, Darmstadt, Germany

Materials for Imaging and Spectroscopy

Table 6.6: Materials used for Imaging and Spectroscopy.

Material	Manufacturer
24 x 40 mm^2 coverglass # 1.5 A	Hartenstein, Würzburg, Germany
24 mm circular coveglass # 1.5 A	Hartenstein, Würzburg, Germany
4-well chambered coverglass	Nunc LabTek 1.5 chambered coverglass Cat. No. 155383, Thermo Fischer Scientific, Dreieich, Germany/ CellView 1.5 chambered coverglass C4-1.5-H-N, IBL Labor, Gerasdorf bei Wien, Austria
Attofluor cell chamber	Thermo Fischer Scientific, Dreieich, Germany

Neutral Density Filter positions

Table 6.7: NDF positions and the maximum laser power observed at the back aperture. The laser power was measured using a photodiode at the back aperture.

ND filter position	Max. Laser power, 20 MHz	Max. Laser power, CW mode
0	500 µW	7 mW
1	70 µW	1 mW
2	6 µW	85 µW
3	500 nW	8 µW

Acquisition parameters

Table 6.8: Time-resolved spectroscopy acquisition parameters.

Parameter	Value
Global TCSPC resolution (ps)	4
Laser repetition rate (MHz)	20 for FCS and TRA / CW mode for fullFCS
Sync divider	8
Global sync offset (ps)	12500
Sync CFD level (mV)	300
Sync zero cross (mV)	10
Channel 1 offset (ps)	0
Channel 1 CFD level (mV)	100
Channel 1 zero cross (mV)	10
Channel 2 offset (ps)	-3950
Channel 2 CFD level (mV)	100
Channel 2 zero cross (mV)	10

Materials used in the time-resolved fluorescence spectrometer setup

Table 6.9: Optical components used in the time-resolved fluorescence spectrometer.

Material and Catalogue number	Abbreviation in figure 3.2	Manufacturer
Olympus IX-71 stand		Olympus, Hamburg, Germany
Hydraharp 400	TCSPC module	PicoQuant, Berlin, Germany
485 nm pulsed laser, LDH-D-C-485		PicoQuant, Berlin, Germany
Laser Combining Unit with polarization maintaining single mode fibre	OF	PicoQuant, Berlin, Germany
100x oil immersion, NA 1.49, UAPON100xOTIRF	OBJ	Olympus, Hamburg, Germany
Achromatic half-wave plate, AHWP05M-600	HWP	Thorlabs, Bergkirchen, Germany
Polarizing beamsplitter, PBS101 420-680	PBS_1	Thorlabs, Bergkirchen, Germany
Dichroic, Quad band zt405/473-488/561/640 rpc phase r uf1	D_1	AHF, Tübingen, Germany
100 µm pinhole, PNH-100	PH	Newport, Darmstadt, Germany
50 µm pinhole, PNH-50	PH	Newport, Darmstadt, Germany
PMA Hybrid-40	$HPMT_1$ and $HPMT_2$	PicoQuant, Berlin, Germany

Keplerian telescope, lens focal length 60 mm, G063126000	L_1, L_2, L_3	Qioptiq, Rhyl, UK
Polarizing beamsplitter cube, 10FC16PB.3	PBS_2	Newport, Darmstadt, Germany
Band pass filter Brightline HC 525/50	EF_1, EF_2	AHF, Tübingen, Germany

Software used in data analysis

Table 6.10: Software used for data acquisition and data analysis.

Software	Source
SymPhoTime 64	PicoQuant, Berlin, Germany
Origin Pro	OriginLab, Massachusetts, USA
MATLAB	Mathworks, Massachusetts, USA
LAS X	Leica Microsystems, Mannheim , Germany
Kristine	AG Seidel Software package, https://www.mpc.hhu.de/en/software/3-software-package-for-mfd-fcs-and-mfis
Chisurf	Peulen, Opanasyuk and Seidel [156], https://github.com/Fluorescence-Tools/chisurf
Fiji	Schindelin et al. [161]

Acknowledgements

Curriculum Vitae

Name:	**Ashwin Balakrishnan**
Address:	Sanderring 4
	97070 Würzburg
	Germany
Date and place of birth:	5th December 1991 in Gudiyattam, India
Contact:	+49 15257360062, ashwin.balakrishnan@uni-wuerzburg.de

Academic Education

since May 2017
Ph.D, AG Heinze, Molecular Microscopy, Rudolf Virchow Zentrum, Universität Würzburg, Würzburg, Germany
Supervisor: Prof. Dr. K. G. Heinze
Project: Fast molecular mobility of β_2-adrenergic receptor revealed by time-resolved fluorescence spectroscopy

October 2014 - September 2016
Master of Science, Molecular Bioengineering, Biotechnologisches Zentrum, TU Dresden, Dresden, Germany (Grade: 2.4)
Thesis with Prof. Dr. K. Fahmy: Spectroscopic investigation of cysteines in LpCopA

August 2009 - April 2013
Bachelor of Technology, Industrial Biotechnology, Centre for Biotechnology, Anna University, Chennai, India (Grade: 9.01)
Thesis with Prof. G. Pennathur: Interaction of substituted quinolines and porphyrins with proteins

Education

2007 - 2009
High school leaving certificate, Major: Maths, physics, chemistry and biology, Holy infant jesus higher secondary school, Chennai, India (Grade: 94%)

Conferences

Oral presentation:

RVZ Symposium, Bad Brückenau, Germany (June 2018)
Focus On Microscopy conference, London, UK (April 2019)
Focus On Microscopy online conference (March 2021)

Poster:

RVZ Symposium, Bad Brückenau, Germany (June 2017)
12th Eureka Symposium, Würzburg, Germany (October 2017)
Novo Nordesk Fonden Symposium, Copenhagen, Denmark (November 2017)
Quantitative Bio Imaging Conference, Göttingen, Germany (January 2018)
RVZ Symposium, Bad Brückenau, Germany (June 2019)
Picoquant Single Molecule Spectroscopy symposium, Berlin, Germany (September 2019)

Workshop

Picoquant time-resolved fluoresence spectroscopy workshop, Berlin, Germany (September 2018)
Picoquant Single Molecule Spectroscopy symposium, Berlin, Germany (September 2019)

Publication

A. Balakrishnan*, K. Hemmen*, J-H. Krohn, S. Choudhury, K. Jansen, M. Friedrich, G. Beliu, M. Sauer, M. J. Lohse, K. G. Heinze, "Unraveling the hidden temporal range of fast β_2-adrenergic receptor mobility by time-resolved fluorescence" submitted

* - first author

Würzburg, 8th December 2021   Ashwin Balakrishnan

Affidavit

I hereby confirm that my thesis entitled **Fast molecular mobility of β_2-adrenergic receptor revealed by time-resolved fluorescence spectroscopy** is the result of my own work. I did not receive any help or support from commercial consultants. All sources and / or materials applied are listed and specified in the thesis.

Furthermore, I confirm that this thesis has not yet been submitted as part of another examination process neither in identical nor in similar form.

Place, Date   Signature

Eidesstattliche Erklärung

Hiermit erkläre ich an Eides statt, die Dissertation **Schnelle molekulare Beweglichkeit des β_2-adrenergen Rezeptors durch zeitaufgelöste Fluoreszenzspektroskopie** eigenständig, d.h. insbesondere selbständig und ohne Hilfe eines kommerziellen Promotionsberaters, angefertigt und keine anderen als die von mir angegebenen Quellen und Hilfsmittel verwendet zu haben.

Ich erkläre außerdem, dass die Dissertation weder in gleicher noch in ähnlicher Form bereits in einem anderen Prüfungsverfahren vorgelegen hat.

Ort, Datum   Unterschrift